

Spring 5-31-2011

Uniform heating of thin ceramic slabs in a multimode microwave cavity

Shuchi Agrawal
New Jersey Institute of Technology

Follow this and additional works at: <https://digitalcommons.njit.edu/dissertations>



Part of the [Mathematics Commons](#)

Recommended Citation

Agrawal, Shuchi, "Uniform heating of thin ceramic slabs in a multimode microwave cavity" (2011).
Dissertations. 273.
<https://digitalcommons.njit.edu/dissertations/273>

This Dissertation is brought to you for free and open access by the Electronic Theses and Dissertations at Digital Commons @ NJIT. It has been accepted for inclusion in Dissertations by an authorized administrator of Digital Commons @ NJIT. For more information, please contact digitalcommons@njit.edu.

Copyright Warning & Restrictions

The copyright law of the United States (Title 17, United States Code) governs the making of photocopies or other reproductions of copyrighted material.

Under certain conditions specified in the law, libraries and archives are authorized to furnish a photocopy or other reproduction. One of these specified conditions is that the photocopy or reproduction is not to be “used for any purpose other than private study, scholarship, or research.” If a user makes a request for, or later uses, a photocopy or reproduction for purposes in excess of “fair use” that user may be liable for copyright infringement,

This institution reserves the right to refuse to accept a copying order if, in its judgment, fulfillment of the order would involve violation of copyright law.

Please Note: The author retains the copyright while the New Jersey Institute of Technology reserves the right to distribute this thesis or dissertation

Printing note: If you do not wish to print this page, then select “Pages from: first page # to: last page #” on the print dialog screen

The Van Houten library has removed some of the personal information and all signatures from the approval page and biographical sketches of theses and dissertations in order to protect the identity of NJIT graduates and faculty.

ABSTRACT

UNIFORM HEATING OF THIN CERAMIC SLABS IN A MULTIMODE MICROWAVE CAVITY

by
Shuchi Agrawal

Two-dimensional reaction diffusion equations, which contain a functional and an inhomogeneous source term, are good models for describing microwave heating of thin ceramic slabs and cylinders in a multi mode, highly resonant cavity. A thin ceramic slab situated in a TE_{N03} rectangular cavity modeled in the small Biot number limit and a thin silicon wafer situated in a TM_{101} cylindrical cavity modeled in the small fineness ratio limit are studied to gain insight into the dynamics of the heating process. The evolution of temperature is governed by a two-dimensional reaction diffusion equation and a spatially non-homogeneous reaction term. Numerical methods are applied to accurately approximate the steady state leading order temperature of this equation and to determine the stability of solutions for Neumann boundary conditions. The choices of parameters in the equation that lead to uniform heating of the ceramic slab have been characterized.

UNIFORM HEATING OF THIN CERAMIC SLABS IN A
MULTIMODE MICROWAVE CAVITY

by
Shuchi Agrawal

A Dissertation
Submitted to the Faculty of
New Jersey Institute of Technology
in Partial Fulfillment of the Requirements for the Degree of
Doctor of Philosophy in Mathematical Sciences

Department of Mathematical Sciences

May 2011

Copyright © 2011 by Shuchi Agrawal
ALL RIGHTS RESERVED

APPROVAL PAGE

UNIFORM HEATING OF THIN CERAMIC SLABS IN A
MULTIMODE MICROWAVE CAVITY

Shuchi Agrawal

Dr. Gregory A. Kriegsmann, Dissertation Advisor
Distinguished Professor, Department of Mathematical Sciences, NJIT

Date

Dr. Gerald Whitman, Committee Member
Professor, Department of Electrical and Computer Engineering, NJIT

Date

Dr. Michael Booty, Committee Member
Professor, Department of Mathematical Sciences, NJIT

Date

Dr. Peter Petropoulos, Committee Member
Associate Professor, Department of Mathematical Sciences, NJIT

Date

Dr. Richard Moore, Committee Member
Associate Professor, Department of Mathematical Sciences, NJIT

Date

BIOGRAPHICAL SKETCH

Author: Shuchi Agrawal
Degree: Doctor of Philosophy
Date: May 2011

Undergraduate and Graduate Education:

- Doctor of Philosophy in Mathematical Sciences,
New Jersey Institute of Technology, Newark, NJ, 2011
- Master of Philosophy in Mathematics,
University of Delhi, 2001
- Master of Science in Mathematics,
St. Stephen's College, University of Delhi, Delhi, India, 1998
- Bachelor of Science in Mathematics,
St. Stephen's College, University of Delhi, Delhi, India, 1996

Major: Mathematical Sciences

Presentations and Publications:

- S. Agrawal, and G. A. Kriegsmann, "Multimode Cavity Heating of a Thin Ceramic Slab," in preparation.
- S. Agrawal, "Stability and Bifurcation Analyses of Microwave Heated Ceramic Cylinders and Slabs," *Frontiers in Applied and Computational Mathematics*, NJIT, May 19-21, 2008.
- S. Agrawal, "Stability of Microwave Heated Ceramic Cylinders and Slabs," *Graduate Student-Faculty Seminars*, Department of Mathematical Sciences, NJIT, July 28, 2008.
- S. Agrawal, "Spatial Patterns due to Diffusion-Driven Instability," *Graduate Student-Faculty Seminars*, Department of Mathematical Sciences, NJIT, November 30, 2005.

To my grandfather Jugal Kishore Bansal (Late) who wanted me to become a medical doctor, to my grandfather Panna Lal who always told me "You must do a Ph.D.", to my parents Shashi Kiran, Rajendra Kumar Bansal, Anjoo Gupta, Ashok Gupta for always standing by me like pillars, to my husband Rajeev Agrawal for being my strength, and to my beautiful kids Sahaj and Rishi.

ACKNOWLEDGMENT

I take this opportunity to express my deep sense of gratitude to my thesis advisor, Prof. Gregory A. Kriegsmann for his invaluable guidance and constant encouragement. He generously provided me financial support whenever I needed it. Working under his close guidance has been a privilege, pleasure and a challenge too. From him I have picked up finer values in life also. He patiently put up with all my shortcomings. He has been a guru to me as one in the Indian tradition. I am indebted to him for everything. His guidance will remain a treasure with me.

I extend my sincere gratitude to Prof. Daljit Ahluwalia, the Chair of the Department of Mathematics, for giving me the opportunity to study at NJIT and for encouraging at every step of PhD.

I acknowledge my indebtedness to Prof. Michael Booty for his kind guidance both as a committee member and as a graduate advisor. I am grateful to my committee members, Prof. Peter Petropoulos, Prof. Richard Moore and Prof. Gerald Whitman for many useful discussions and suggestions. I would also like to thank Ms. Padma Gulati and Ms. Susan J. Sutton for helping me with the administrative work.

I reiterate my gratitude to my teacher, Prof. Ajit Iqbal Singh of University of Delhi, India. She groomed me in mathematics and in life. The training I received from her has been a constant asset to me especially during my stay in USA.

Special thanks go to many friends, in particular Kuan Xu, Manmeet Kaur, Yogesh Joshi, Daniel Cargill, Neha Mittal, Charu Chinhalli, Krishna Boddakayala, Rama Abbireddy and Anuradha Boddakayala for helping me at various stages of PhD and for providing the much needed moral support in difficult times.

I owe my sincere thanks to Mrs. Anjoo Gupta, my mother-in-law; Mr. Ashok Gupta, my father-in-law; Dr. Shashi Kiran, my mother and Mr. Rajender Bansal, my father, for being excellent parents and helping me take care of my family to provide

me with the time to study. They are a personification of love and affection which has gone a long way in the completion of this dissertation. With pleasure I thank Mr. Rajeev Agrawal, my husband for his constant support and understanding without which the completion of the manuscript would not have been possible. He has been my strength and a true friend throughout these years. My children, Sahaj 8 years old, and Rishi 2 years old are my inspiration. They have grown up while I was involved in my research work. I am indebted to them for my time that they deserved.

TABLE OF CONTENTS

Chapter	Page
1 INTRODUCTION	1
2 ONE FUNCTIONAL PROBLEM	4
2.1 Introduction	4
2.2 Stationary Solutions	8
2.2.1 A Symmetric Stationary Solution	9
2.2.2 An Asymmetric Stationary Solution	19
2.3 Linear Stability	29
2.3.1 Linear Stability of Symmetric Stationary Solution	31
2.3.2 Linear Stability of Asymmetric Stationary Solution	36
2.4 Dynamical Simulations	42
2.5 Conclusions	50
2.6 Future Work	52
3 TWO FUNCTIONAL PROBLEM	54
3.1 Introduction	54
3.2 Stationary Solutions	57
3.2.1 A Symmetric Stationary Solution	58
3.2.2 An Asymmetric Stationary Solution	65
3.3 Linear Stability	72
3.3.1 Linear Stability of Symmetric Stationary Solution	75
3.3.2 Linear Stability of Asymmetric Stationary Solution	78
3.4 Dynamical Simulations	83
3.5 Conclusions	88
3.6 Future Work	88
4 CIRCULAR GEOMETRY	90
4.1 Introduction	90

TABLE OF CONTENTS
(Continued)

Chapter	Page
4.2 Radial Stationary Solutions	90
4.3 Linear Stability	103
4.4 Dynamical Simulations	108
4.5 Conclusions	109
4.6 Future Work	109
APPENDIX A DELTA FUNCTION AS A SOURCE	110
A.1 A Model Problem: $N = 1$	110
A.2 The Model: $N = 2$	116
REFERENCES	121

LIST OF TABLES

Table	Page
2.1 Special Values of Γ and P	13
2.2 Critical Points (P_{crit}, q_{crit}) at which modes become unstable, $D = 1.75$. . .	35
2.3 Parameter Values For Uniform Heating For Arbitrary Initial Data.	51
3.1 Critical Points (P_{crit}, q_{scrit}) for $D = 1.75$, Time Varying Source.	79

LIST OF FIGURES

Figure	Page
2.1 Geometry of 2-D model.	6
2.2 $\ u_{0s}\ _2$ as a function of q_s for $D = 1.75$	11
2.3 Γ as a function of q_s for $D = 1.75$	11
2.4 q_s as a function of P for $D = 1.75$	13
2.5 Steady state temperature u_{0s} as a function of x for $P \sim 1, D = 1.75$ in three branches.	14
2.6 q_s as a function of P for several values of $D, N = 1, 2$	15
2.7 q_s as a function of P for several values of $D, N = 3, 4$	15
2.8 $u_{0s}(x)$ for $P \sim 2, N = 1, 2$	16
2.9 $u_{0s}(x)$ for $P \sim 2, N = 3, 4$	17
2.10 $U_{0s}(x)$ for $D = 1.75, N = 1, 2, P \sim 1$, upper branch.	17
2.11 $U_{0s}(x)$ for $D = 1.75, N = 3, 4, P \sim 1$, upper branch.	18
2.12 Top view of the stationary solutions when rotated at 90 degrees. The solutions admit a stripe like structure.	18
2.13 q_a as a function of P for $D = 1.75$	20
2.14 Steady state temperature u_{0a} as a function of x for $P \sim 1, D = 1.75$ in three branches.	21
2.15 q_a as a function of P for several values of $D, N = 1, 2$	22
2.16 q_a as a function of P for several values of $D, N = 3, 4$	22
2.17 Symmetric and asymmetric branches.	23
2.18 $u_{0s}(x)$ and $u_{0a}(x)$ for $D = 0.25, 1.75, P \sim 2$	23
2.19 $u_{0a}(x)$ for $P \sim 2, N = 1, 2$	24
2.20 $u_{0a}(x)$ for $P \sim 2, N = 3, 4$	25
2.21 $U_{0a}(x)$ for $D = 1.75, P \sim 0.65, N = 1, 2$, upper branch.	26
2.22 $U_{0a}(x)$ for $D = 1.75, P \sim 0.65, N = 3, 4$, upper branch.	26
2.23 $U_{0a}(x)$ for $D = 1.75, P \sim 0.8, N = 1, 2$, upper branch.	27

LIST OF FIGURES
(Continued)

Figure	Page
2.24 $U_{0a}(x)$ for $D = 1.75, P \sim 0.8, N = 3, 4$, upper branch.	27
2.25 $U_{0a}(x)$ for $D = 1.75, P \sim 1, N = 1, 2$, upper branch.	28
2.26 $U_{0a}(x)$ for $D = 1.75, P \sim 1, N = 1, 2$, upper branch.	29
2.27 Lowest eigenvalue $\Lambda_{00}^s = \lambda_0^s$ and first odd non-local eigen-value $\Lambda_{01}^s = \lambda_1^s$ for $D = 0.25$	32
2.28 Lowest eigenvalue $\Lambda_{00}^s = \lambda_0^s$ and first odd non-local eigen-value $\Lambda_{01}^s = \lambda_1^s$ for $D = 1$	32
2.29 Lowest eigenvalue $\Lambda_{00}^s = \lambda_0^s$ and first odd non-local eigen-value $\Lambda_{01}^s = \lambda_1^s$ for $D = 1.75$	33
2.30 First local eigen-value Λ_{10}^s for $N = 1, 2$	35
2.31 First local eigen-value Λ_{10}^s for $N = 3, 4$	36
2.32 λ_0^a and λ_1^a for $D = 0.25$	37
2.33 Lowest eigen-value λ_0^a and first odd non-local eigen-value λ_1^a for $D = 1$	38
2.34 λ_0^a and λ_1^a for $D = 1.75$	38
2.35 λ_0^s and λ_0^a for $D = 1$	39
2.36 λ_1^s and λ_1^a for $D = 1$	39
2.37 First local eigen-value Λ_{10}^a for $N = 1, 2$	41
2.38 First local eigen-value Λ_{10}^a for $N = 3, 4$	41
2.39 $U(x, y, t)$ for $P = 1, D = 1.75$. Initial condition: $U_{0s}(x)$	44
2.40 $U(x, y, t)$ for $N = 2, P = 1$. Initial condition: $U_{0s}(x)$	45
2.41 $U(x, y, t)$ for $N = 2, P = 1$ at later times.	45
2.42 $U(x, y, t)$ for $P = 3$. Initial condition: $U_{0s}(x)$	46
2.43 $U(x, y, t)$ for $P = 3, N = 1, 2$. Initial condition: $U_{0s}(x) + \epsilon \cos(\frac{\pi y}{h})$	47
2.44 $U(x, y, t)$ for $P = 3, N = 3, 4$. Initial condition: $U_{0s}(x) + \epsilon \cos(\frac{\pi y}{h})$	47
2.45 $U(x, y, t)$ for $P = 3, N = 1, 2$. Initial condition: $\epsilon \cos(\frac{\pi y}{h})$	48
2.46 $U(x, y, t)$ at $t = 1$ for $N = 3, P \sim 3$. Initial condition: $\epsilon \cos(\frac{\pi y}{h})$	49
2.47 $U(x, y, t)$ for $N = 3, P \sim 3$ as it evolves. Initial condition: $\epsilon \cos(\frac{\pi y}{h})$	49

LIST OF FIGURES
(Continued)

Figure	Page
2.48 $U(x, y, t)$ at later times for $N = 3, P \sim 3$. Initial condition: $\epsilon \cos(\frac{\pi y}{h})$	50
2.49 S-curves for $D = 2.25, N = 1, 2$	52
2.50 Stationary states for $D = 2.25, N = 1, 2$	53
3.1 N as a periodic function of time in one period of t	56
3.2 Γ_1 as a function of Γ_2 and $q_s, D = 1.75$	60
3.3 Maximum temperature as a function of power for $D = 0.75, 1.25$	61
3.4 Maximum temperature as a function of power for $D = 1.75, 2, 25$	61
3.5 Stationary solution as a function of $x, P \sim 1, D = 1.75$	62
3.6 Comparison of symmetric states obtained from using one source with those that use a time-varying source when $P \sim 2$	62
3.7 Comparison of symmetric states obtained from using one source with those that use a time-varying source when $P \sim 2$	63
3.8 $U_{0s}^*(x), a_1 = 0.2, P \sim 2, D = 1.75$	64
3.9 $U_{0s}^*(x), a_1 = 0.5, 0.8, P \sim 2, D = 1.75$	64
3.10 Γ_1 as a function of Γ_2 and $q_a, D = 1.75$	66
3.11 P vs q_a for $D = 0.75, 1.25$ and $a_1 = 0.2, 0.5, 0.8$	66
3.12 P vs q_a for $D = 1.75, 2.25$ and $a_1 = 0.2, 0.5, 0.8$	67
3.13 $u_{0a}(x)$ for $P \sim 1, D = 1.75$ and $a_1 = 0.2, 0.5, 0.8$	68
3.14 Asymmetric states obtained from using one source vs those that use two sources for $P \sim 2, D = 0.75, 1.25$	68
3.15 Asymmetric states obtained from using one source vs those that use two sources for $P \sim 2, D = 1.75, 2.25$	69
3.16 $U_{0a}^*(x), a_1 = 0.2, P \sim 1, D = 1.75$	69
3.17 $U_{0a}^*(x), P \sim 2, D = 1.75$	70
3.18 $u_{0a}(x)$ and $U_{0a}^*(x)$ for $P \sim 7.71, D = 1.75$	71
3.19 $U_{0a}^*(x)$ for $P \sim 7.71, D = 1.75, a_1 = 0.5, 0.8$	72
3.20 Lowest non local eigen-value $\Lambda_{00}^s = \lambda_0^s$ for $D = 0.75, 1.25$	76

LIST OF FIGURES
(Continued)

Figure	Page
3.21 Lowest non local eigen-value $\Lambda_{00}^s = \lambda_0^s$ for $D = 1.75, 2.25$	76
3.22 Non local eigen-value $\Lambda_{01}^s = \lambda_1^s$ for $D = 0.75, 1.25$	77
3.23 Non local eigen-value $\Lambda_{01}^s = \lambda_1^s$ for $D = 1.75, 2.25$	77
3.24 First local eigen-value Λ_{10}^s for $D = 0.75, 1.25$	78
3.25 First local eigen-value Λ_{10}^s for $D = 1.75, 2.25$	78
3.26 Lowest non local eigen-value $\Lambda_{00}^a = \lambda_0^a$ for $D = 0.75, 1.25$	79
3.27 Lowest non local eigen-value $\Lambda_{00}^a = \lambda_0^a$ for $D = 1.75, 2.25$	80
3.28 Non local eigen-value $\Lambda_{01}^a = \lambda_1^a$	80
3.29 Non local eigen-value $\Lambda_{01}^a = \lambda_1^a$	81
3.30 Local eigen-value Λ_{10}^a for $D = 0.75, 1.25$	82
3.31 Local eigen-value Λ_{10}^a for $D = 1.75, 2.25$	82
3.32 $U(x, y, t)$ for $P = 1, D = 1.75$. Initial condition: $U_{0s}^*(x)$	84
3.33 $U(x, y, t) = U_{0a}^*(x)$ for $P = 2, a_1 = 0.2$. Initial condition: $U_{0s}^*(x)$	85
3.34 $U(x, y, t) = U_{0a}^*(x)$ for $P = 2, a_1 = 0.5, 0.8$. Initial condition: $U_{0s}^*(x)$	85
3.35 $U(x, y, t)$ for $P = 2$. Initial condition: $U_{0s}^*(x) + \epsilon \cos(\frac{\pi y}{h})$	86
3.36 $U(x, y, t)$ for $P = 2$. Initial condition: $U_{0s}^*(x) + \epsilon \cos(\frac{\pi y}{h})$	87
3.37 $U(x, y, t)$ for $P = 2$. Initial condition: $U_{0s}^*(x) + \epsilon \cos(\frac{\pi y}{h})$	87
4.1 Cylindrical Geometry.	91
4.2 Electric field sources J_0^2, J_1^2 as a function of r	93
4.3 q as a function of P ; $\mathbf{S} = J_0^2$	96
4.4 q as a function of P ; $\mathbf{S} = J_1^2$	96
4.5 $u_0(r)$ for $\mathbf{S} = J_0^2, D = 2, P \sim 1.75$, three branches.	97
4.6 $u_0(r)$ for $\mathbf{S} = J_1^2, D = 2, P \sim 1.75$, three branches.	97
4.7 $U_0(x, y)$ for $\mathbf{S} = J_0^2, D = 2, P \sim 1.75$, three branches.	98
4.8 $U_0(x, y)$ for $\mathbf{S} = J_1^2, D = 2, P \sim 1.75$, three branches.	98
4.9 $\ u_0\ _2$ as a function of q ; $\mathbf{S} = J_0^2, J_1^2$	99

LIST OF FIGURES
(Continued)

Figure	Page
4.10 $u_0(r)$ for $P \sim 1.75$, $\mathbf{S} = J_0^2$, upper branch.	100
4.11 $u_0(r)$ for $P \sim 1.75$, $\mathbf{S} = J_1^2$, upper branch.	100
4.12 $U_0(x, y)$ for $P \sim 1.75$, upper branch, $\mathbf{S} = J_0^2$	101
4.13 $U_0(x, y)$ for $P \sim 1.75$, upper branch, $\mathbf{S} = J_0^2$	101
4.14 $U_0(x, y)$ for $P \sim 1.75$, upper branch, $\mathbf{S} = J_1^2$	102
4.15 $U_0(x, y)$ for $P \sim 1.75$, upper branch, $\mathbf{S} = J_1^2$	102
4.16 Lowest eigen-value λ_0 as a function of q , $\mathbf{S} = J_0^2$	104
4.17 Lowest eigen-value λ_0 as a function of q , $\mathbf{S} = J_1^2$	105
4.18 λ_1 as a function of q , $\mathbf{S} = J_0^2$	105
4.19 λ_1 as a function of q , $\mathbf{S} = J_1^2$	106
4.20 Λ_{11} as a function of q , $D = 1$	107
A.1 u_0^* as a function of p	112
A.2 Bifurcation branch for $D = 1$	119
A.3 Symmetric and asymmetric solutions for $D = 1$	120

CHAPTER 1

INTRODUCTION

The word ceramics derives from the Greek word 'keramos' meaning burnt stuff. In general a ceramic has been defined as any inorganic or non-metallic material rendered hard and heat resistant by heating at temperatures of 1000 degrees Fahrenheit or above. Most of the important ceramics consist of complex oxides and silicates, although a number of useful carbide, nitride and boride ceramics are also produced. For the purposes of this thesis, it will be enough to define ceramics as a material suitable for heat processing and characterized by a low thermal conductivity [25].

The ceramic industry is a fast growing industry with current world sales in multi billion dollars. An important characteristic of the ceramic industry is that it is basic to the successful operation of many other industries such as automobile, architectural, electronic and electrical industries. Useful chemical, electrical, mechanical, thermal and structural properties of ceramics have led to diverse and specialized uses in industry [9]. The increasing demand of ceramics in the industry has accelerated research into more efficient methods such as microwave and millimeter wave heating for producing them. According to Bykov et al., [4], the possibility of ceramics processing was discussed about 50 years ago by Von Hippel [24], and experimental studies started in the middle of the 1960s by Tinga and co-authors [22, 23]. Since then many investigators have reported results on microwave sintering and joining of ceramics [1, 26].

Microwaves are electromagnetic waves with frequencies between 0.3 and 300 gigahertz. A standardized frequency of 2.45 gigahertz is used in industrial microwave applications of ceramics. There is a fundamental difference between microwave heating and conventional heating processes. In microwave processes, microwaves penetrate

a material and get transformed into heat so that heat is generated internally within the material whereas in conventional heating processes, heat diffuses inward from the sample surface. As a result of internal and volumetric heating, microwave processing makes it possible to heat both small and large shapes very rapidly and more uniformly as compared to conventional heating.

Microwave heating is known to exhibit temperature instabilities and formation of hot spots. Although hot spot formation and thermal runaway has been reported to be catastrophic by most researchers, Jerby et al., [7, 6] utilized the phenomenon of hot-spot formation to invent the microwave drill, a new method to drill into hard non-conductive materials. The microwave drill is based on the principle of concentrating microwave energy into a small spot where the hole needs to be drilled, much smaller than the microwave wavelength itself.

The structure of the remainder of the thesis is as follows. Chapter 2 deals with the formulation and the results for the heating of a ceramic slab in a multi mode microwave cavity which gives rise to a two dimensional reaction diffusion equation with one-functional. It will be demonstrated using accurate numerical techniques that when the dimensionless diffusion constant $D > 1$ and electric field modal number $N > 1$, then uniform heating of the slab can be achieved by choosing an appropriate value of dimensionless power P . It will also be shown that as D decreases, the solutions become more localized and the maximum temperature increases. In Chapter 3, the solutions are studied when the back wall of the rectangular cavity is moved as a function of time. Moving the back wall varies the N in the electric field source term as a function of time. The case when the mode number N switches between two values at regular intervals of time gives rise to a two dimensional reaction diffusion equation with two-functionals and will be discussed in detail. Finally, microwave heating of a thin silicon fibre in a cylindrical geometry is discussed in Chapter 4.

The goal of this dissertation is to study mathematically the experiments done by researchers to obtain uniform heating of a thin aluminium slab in a rectangular microwave cavity and to obtain rapid heating of silicon wafers in a cylindrical cavity. The evolution of temperature is governed by a two-dimensional reaction diffusion equation and a spatially non-homogeneous reaction term. Numerical techniques have been applied to accurately approximate steady states of the resulting equations. These solutions have then been studied for stability as they evolve in time. The stability of steady state solutions depends on different parameters in the equation. A careful examination of these parameters has been done to distinguish stable steady states from unstable ones. Finally, the parameters that will provide the most uniform temperature distribution along the ceramic slab have been characterized.

CHAPTER 2

ONE FUNCTIONAL PROBLEM

2.1 Introduction

Microwave heating is known to exhibit temperature instabilities and formation of hot spots. Brodwin and Johnson used a TE_{103} rectangular cavity with an adjustable aperture and a moving short circuit to design an experiment for sintering of certain ceramics [3]. They found experimentally that it was impossible to obtain uniform heating and that increasing the power eventually resulted in local melting. Non-uniform heating causes the temperature to be higher at certain parts of the sample. If the incident power is above a critical value, it leads to thermal runaway which is interpreted as a hot spot. In [13], Kriegsmann modeled this experiment for heating of a thin ceramic slab and was able to explain these observations mathematically. He found that the evolution of temperature is governed by a two dimensional reaction diffusion equation with a functional that admits stripe like temperature distribution. This solution became unstable and evolved into a hot spot. The striped solution was studied in [13] when a single electric mode with modal number $N = 1$ propagates in the microwave cavity. This chapter deals with studying the location and stability of stripes when a single mode with modal number $N \geq 2$ propagates in a multi mode microwave cavity.

In [12], Kriegsmann studied the effects of varying aperture size of the microwave cavity on the heating of a ceramic slab of finite thickness situated in a TE_{103} applicator with adjustable iris. The cavity was adjusted so that only one mode was allowed to propagate at a time. It was shown that for large aperture openings, the shape of the S-curve describing maximum temperature as a function of power was due to skin effect shielding, while for smaller openings, the upper branches were due to cavity

detuning as opposed to the skin effect. Walker further extended this work and studied the problem when a thick slab was heated in a TE_{M01} cavity which could support multiple modes. The shape of S-curve was again either due to skin effect shielding or cavity detuning. It was also found that an increase in the number of electric field modes propagating within the object lead to more uniform temperature.

The problem of heating of a thin ceramic slab in a highly resonant TE_{N03} multi mode applicator gives rise to a two-dimensional functional, reaction-diffusion equation. The modeling is identical to that in [13] where the solutions have been studied for $N = 1$ in a one-dimensional cavity. The solutions will now be analyzed for $N \geq 2$ in a two-dimensional cavity where a TE_{N0} mode would be excited at the aperture. This cavity can support modes with modal number $N > 1$ and has been considered in [25] to study the heating of a thick slab where multiple modes propagate in the cavity. For convenience, the geometry of the applicator has been described below.

The rectangular applicator comprises of a waveguide, an iris and a moveable back wall called short at $Z = L$, Figure 2.1. The term cavity is used to describe the region occupied by the iris, the ceramic sample and the waveguide walls. The waveguide and the iris are of uniform height H and there is no gap present between these structures. The slab completely fills the cross sectional area of the waveguide. This arrangement prevents the aperture and slab from exciting modes with field variations in Y direction.

The slab is placed in the center of the cavity where the electric field intensity inside the applicator is maximum. This is particularly important because the slab is thin. The waveguide width W is fixed and the cavity length L is allowed to vary by moving the back wall. The choice of L determines the N in the TE_{N03} cavity.

The variables (X, Y, Z) are non-dimensionalized with respect to the waveguide width W and the new variables are $(x, y, z) = (1/W)(X, Y, Z)$. The dimensionless

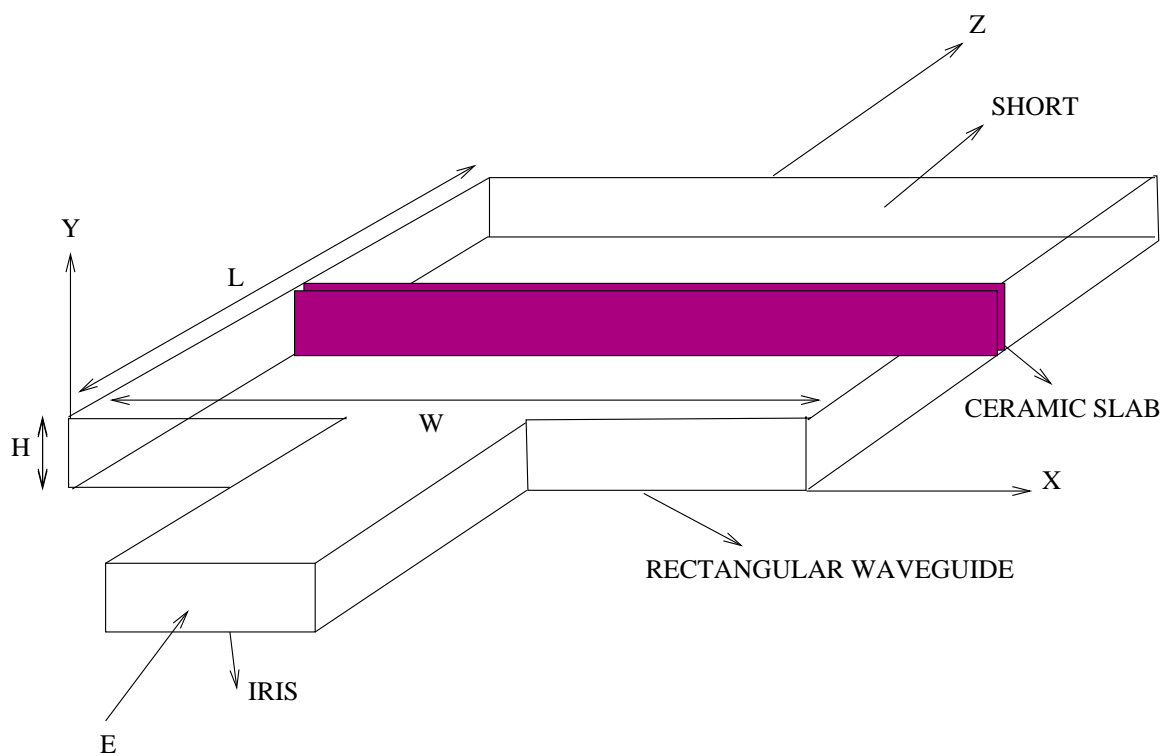


Figure 2.1 Geometry of 2-D model.

temperature U is defined by $U = (T - T_A)/T_A$, where T is the dimensional temperature and $T_A = 300^\circ\text{C}$ is the ambient temperature. Since the slab is thin, the leading order term in the small Biot number expansion of the dimensionless temperature is independent of z and takes the form of a non-dimensional equation in $U(x, y, t)$:

$$\frac{\partial}{\partial t}U = D\nabla_{\perp}^2U - 2L(U) + P \sin^2(N\pi x)g(U), \quad (x, y) \in \Omega, \quad (2.1a)$$

$$f(U) = e^{CU}, \quad g(U) = \frac{f(U)}{\left[1 + \frac{\chi}{h} \int_0^h \int_0^1 \sin^2(N\pi x) f(U) dx dy\right]^2}, \quad (2.1b)$$

$$L(U) = U + \beta[(1 + U)^4 - 1], \quad (2.1c)$$

where ∇_{\perp}^2 is the Laplacian in x and y , $\Omega = \{(x, y) | 0 < x < 1, 0 < y < h = 0.8\}$, $L(U)$ is the boundary loss term, P is the dimensionless power that is applied by the electric field source, C is a positive constant, e^{CU} is the effective electrical conductivity and N is a positive integer. The dimensionless diffusion coefficient $D = (dK/h_e W^2)$ is a function of h_e , the effective heat transfer coefficient of ceramic's surface. Here d is the slab thickness, K is the thermal conductivity of the material and D is assumed to be $O(1)$. The parameter $\beta = \frac{seT_A^3}{he}$, where s is the Stefan-Boltzman constant, e is the emissivity of the ceramic. Temporal evolution of U is described and is studied as a function of microwave power P . The boundary conditions are

$$\frac{\partial U}{\partial n} = 0, \quad (x, y) \in \partial\Omega, \quad (2.1d)$$

where $\partial\Omega$ is the lateral boundary of the slab and initial conditions are

$$U(x, y, 0) = 0, \quad (2.1e)$$

i.e., the slab is initially at ambient temperature. The stationary solutions are found in Section 2.2. Section 2.3 deals with linear stability of these solutions. The evolution of solutions with time will be discussed in Section 2.4.

2.2 Stationary Solutions

Determining all the steady state solutions to equation (2.1a) and the given boundary and initial conditions is hard but as observed in [13], the steady state solution $u_0(x)$ of the one-dimensional version of the problem when there is no y dependence satisfies (2.1a-d) and is therefore, a solution of equation (2.1a). Physically, the stationary solution $U_0 = u_0(x)$ represents a stripe pattern and this striped solution will be determined in this section.

Consider the y -independent version of equation (2.1a) and let the solution be denoted by u .

$$u_t = Du_{xx} - 2L(u) + Pg(u) \sin^2(N\pi x), \quad 0 < x < 1, \quad (2.2a)$$

$$f(u) = e^{Cu}, \quad g(u) = \frac{f(u)}{[1 + \chi \int_0^1 e^{Cu} \sin^2(N\pi \tilde{x}) d\tilde{x}]^2}, \quad (2.2b)$$

$$u_x = 0, \quad x = 0, 1, \quad (2.2c)$$

$$u(x, 0) = 0, \quad 0 < x < 1, \quad (2.2d)$$

where the boundary loss term $L(u)$ now is $L(u) = u + \beta((1 + u)^4 - 1)$. The steady state version of equations (2.2a-c) is

$$Du_{0xx} - 2L(u_0) + Pg(u_0) \sin^2(N\pi x) = 0, \quad 0 < x < 1, \quad (2.3a)$$

$$f(u_0) = e^{Cu_0}, \quad g(u_0) = \frac{f(u_0)}{[1 + \chi \int_0^1 e^{Cu_0} \sin^2(N\pi \tilde{x}) d\tilde{x}]^2}, \quad (2.3b)$$

$$u_{0x} = 0, \quad x = 0, 1, \quad (2.3c)$$

where u_0 denotes the steady state solution. Equations (2.3a-c) are a boundary value problem for a functional differential equation and admit both symmetric (u_{0s}) and asymmetric (u_{0a}) steady state solutions, when $N > 1$. There is a special point (P_b, q_b) on the S-shaped curve at which the stationary solutions bifurcate from the symmetric branch and lock themselves into an asymmetric branch. In fact, it was possible to produce the asymmetric branch of the response curve when the method

in [13] was used to find the stationary solutions. This is not a numerical artifact but a mathematical phenomenon which has been seen in the model problem discussed in Appendix. The simpler equation considered in the model problem was solved exactly using analytical techniques to yield symmetric and asymmetric stationary solutions. These solutions have properties similar to those of equation (2.3a). This will be demonstrated numerically in the following sections.

2.2.1 A Symmetric Stationary Solution

Since the source term is symmetric about $x = \frac{1}{2}$, solutions with the same symmetry are desired. The shooting method used to approximate symmetric steady states is a slight variation of the method described in [13]. Consider the related initial value problem:

$$D\psi_{xx} - 2L(\psi) + \Gamma \sin^2(N\pi x)f(\psi) = 0, \quad 0 < x < 1, \quad (2.4a)$$

$$\psi(0) = \alpha, \quad (2.4b)$$

$$\psi_x(0) = 0, \quad (2.4c)$$

where Γ is a positive constant. The above initial value problem is solved numerically using a fourth order Runge-Kutta scheme for a fixed α and Γ . The solution of equations (2.4a-c) satisfies equations (2.3a-c) if

$$\psi_x(1) = 0, \quad (2.5a)$$

$$\|\psi\|_2^2 - \zeta = 0, \quad (2.5b)$$

where $\|\psi\|_2$ denotes the $L^2[0, 1]$ norm of ψ defined by:

$$\|\psi\|_2 = \left(\int_0^1 \psi(x)^2 dx \right)^{1/2}. \quad (2.6)$$

Define the functions $G(\Gamma; \alpha; \zeta) = \psi_x(1)$ and $H(\Gamma; \alpha; \zeta) = \|\psi\|_2^2 - \zeta$. If ζ , Γ and α can be found such that $G = H = 0$, then equations (2.5a,b) will be satisfied. This is done by fixing ζ and using a 2-dimensional Newton's method to find Γ and α . A continuation procedure [13] on ζ is used to obtain the starting values Γ_0 and α_0 . Choose $\zeta_0 \ll 1$ so that equations (2.4a-c) can be linearized and solved exactly to give:

$$\Gamma^0 = 4\sqrt{\frac{\zeta_0}{\rho^2 + 2\varrho^2}}, \quad (2.7a)$$

$$\alpha^0 = \frac{\Gamma^0(\rho - \varrho)}{4\rho\varrho}, \quad (2.7b)$$

where $\rho = L'(0)$ and $\varrho = L'(0) + 2DN^2\pi^2$. These values of Γ and α are used as the initial guesses in Newton's method. Once $\Gamma(\zeta_0)$ and $\alpha(\zeta_0)$ are obtained, a slightly larger value of ζ , say $\zeta_1 > \zeta_0$, is chosen and $\Gamma(\zeta_0)$, $\alpha(\zeta_0)$ are used respectively as initial guesses for $\Gamma(\zeta_1)$ and $\alpha(\zeta_1)$. This process is continued and yields the functions $\Gamma(\zeta)$ and $\alpha(\zeta)$. Each ζ yields a symmetric steady state solution on $[0, 1]$. Let q_s denote the maximum temperature of the symmetric solution so that

$$q_s = \max_{x \in [0,1]} \psi(x). \quad (2.8)$$

Figure 2.2 shows that there is a 1-1 correspondence between ζ and q_s for several values of N . Since it is desired to study different parameters as a function of maximum temperature, therefore, Γ is treated as a function of q_s and q_s is used for plotting results. The solution of equations (2.4a-c) and (2.5a,b) will completely satisfy equations (2.3a-c) when

$$P = \Gamma(q_s) \left[1 + \chi \int_0^1 \sin^2(N\pi x) f(\psi) dx \right]^2. \quad (2.9)$$

Equation (2.9) implicitly gives the maximum temperature along the surface of the slab as a function of power P . Set $\beta = \chi = 0.01$, $C = 1.5$, values representative of

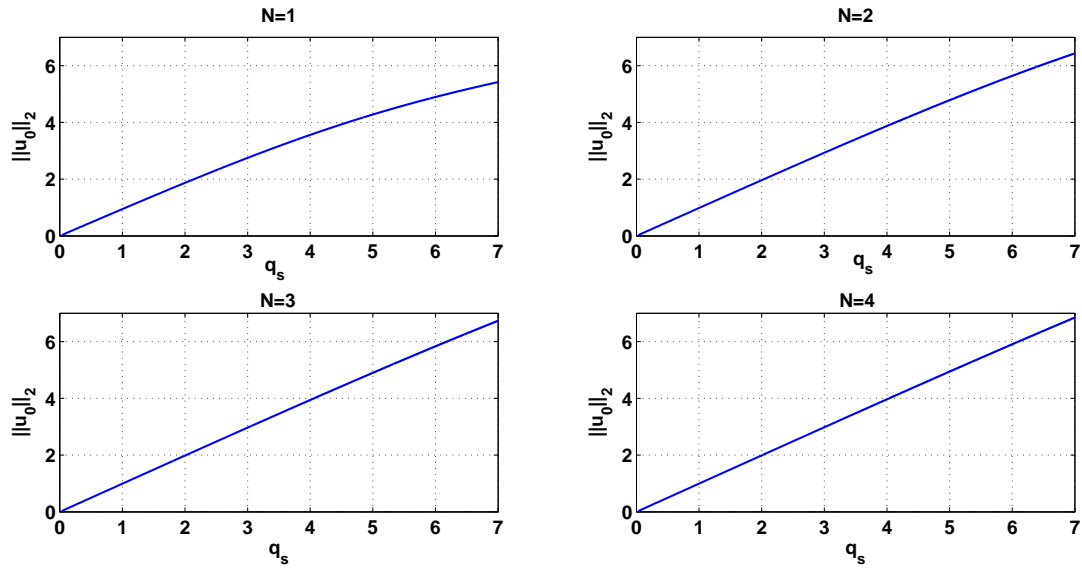


Figure 2.2 $\|u_{0s}\|_2$ as a function of q_s for $D = 1.75$.

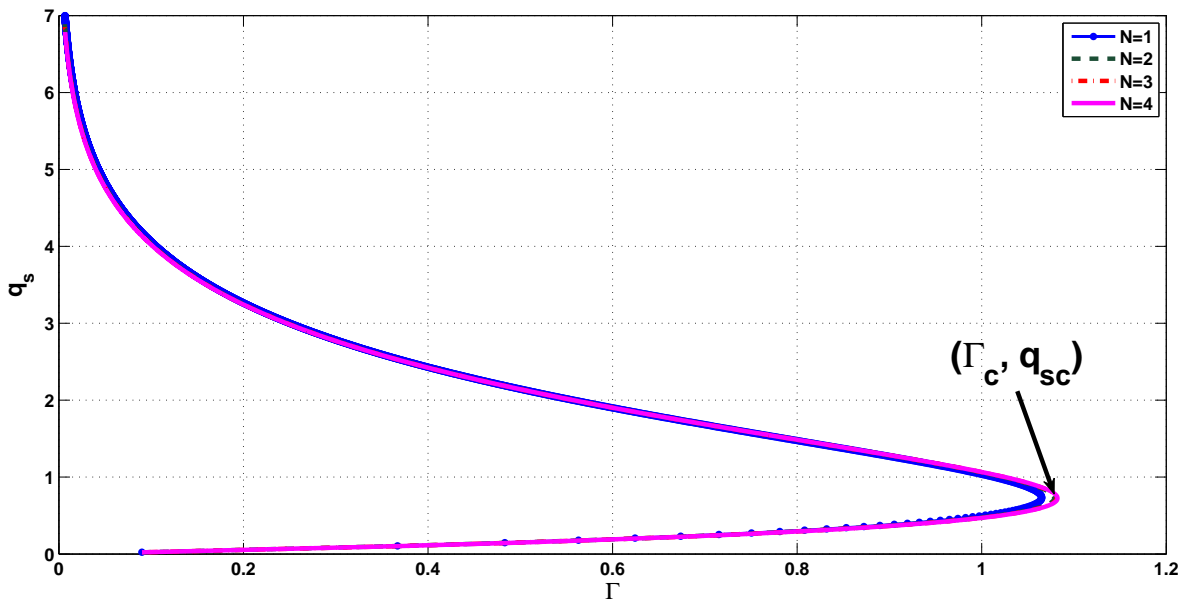


Figure 2.3 Γ as a function of q_s for $D = 1.75$.

the low-loss ceramic alumina. Also set, $d = 4.5 \text{ mm}$, $W = 9 \text{ cm}$. Finally, a nominal value of $h_e \sim 10 \text{ Watts/m}^2 \text{ }^\circ\text{K}$ corresponds to $D = 1$. For the discussion that follows D is taken to be 1.75 and $N = 1, 2, 3, 4$. The behaviour of solutions will be studied for these parameter values unless otherwise specified. Although the case $N = 1$ has been studied in [13], the results for this case also are studied as a means for comparison.

Figure 2.3 plots Γ as a function of q_s for four values of N . Γ is a multi-valued function of maximum stationary temperature as was found in [13]. There are two solutions for $\Gamma < \Gamma_C$ and no solution for $\Gamma > \Gamma_C$. For very thin slabs, $\chi \sim 0$ and there is a critical power $P_C \sim \Gamma_C$ beyond which there is no stationary solution. For $P < P_C$, the lower branch solution occurs due to the balance between microwave power being absorbed by the material and the thermal power being lost at the surface of the slab. When $P > P_C$, the slab does not have enough surface area to release the thermal power and the temperature runs away exceeding the melting point of the ceramic.

When $\chi = 0.01$, then $P \sim \Gamma$ when ψ and the integral are $O(1)$. Since ψ and the exponential increase with q_s , therefore, $P \neq \Gamma$ for larger values of q_s . Response curves in Figure 2.4 show that q_s is a multi-valued function of P with one solution for $P < P_L$ ($P > P_C$) and three solutions for $P_L < P < P_C$. The upper branch solution occurs due to cavity detuning. When $P > P_C$, electrical conductivity becomes large because of increase in temperature which detunes the cavity and reduces the exciting electric field. Table 2.1 gives values of Γ_C , P_C and P_L for $\chi = 0.01$, $N = 1, 2, 3, 4$.

For small values of power, maximum temperature is nearly the same for $N = 1, 2, 3, 4$ as predicted by curves in Figure 2.4. For higher values of power, this temperature decreases monotonically as N increases which suggests that stability increases with N .

Figure 2.5 is a plot of stationary temperature $u_{0s}(x)$ as a function of x for $P \sim 1$ corresponding to lower, middle and upper branches of curves in Figure 2.4. On the lower branch the temperature is nearly constant along x for all values of N . Non-linear

Table 2.1 Special Values of Γ and P for $D = 1.75, C = 1.5$

N	Γ_c	P_c	P_L
1	1.065	1.097	0.492
2	1.079	1.112	0.511
3	1.081	1.114	0.514
4	1.082	1.115	0.515

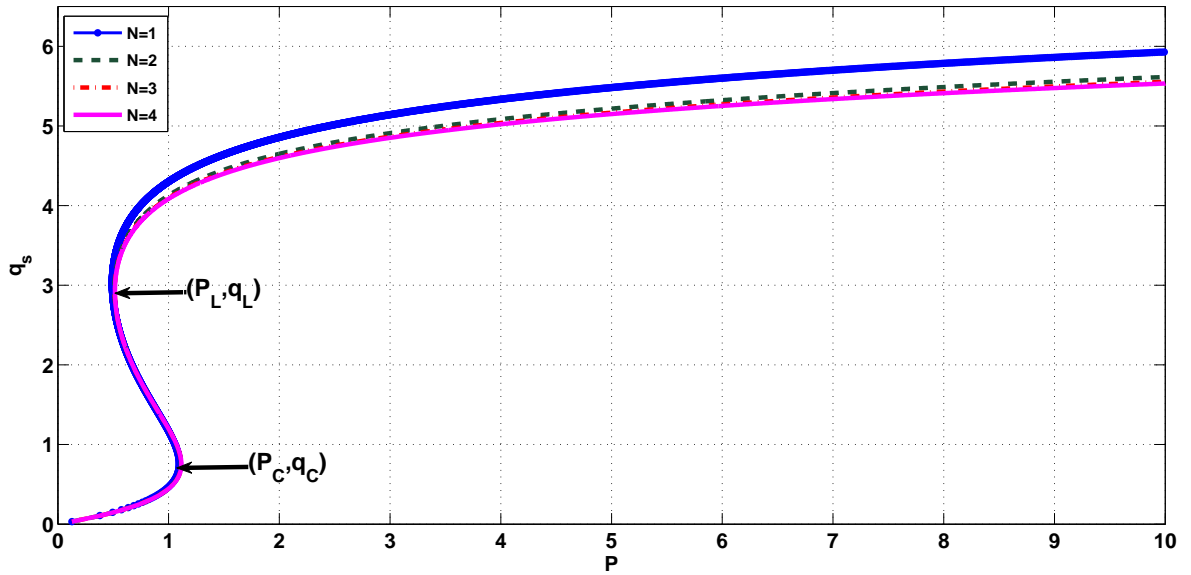


Figure 2.4 q_s as a function of P for $D = 1.75$.

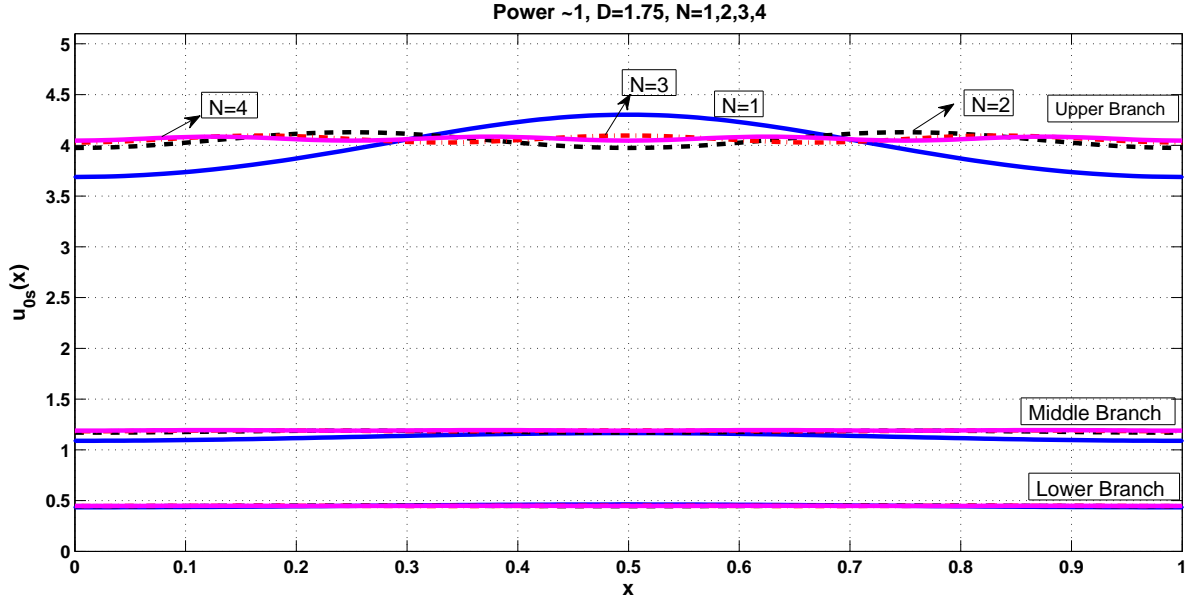


Figure 2.5 Steady state temperature u_{0s} as a function of x for $P \sim 1, D = 1.75$ in three branches.

behaviour becomes prominent in middle and upper branches where there are more temperature variations along x . The maximum temperature $q_s \sim 4.3$ when $N = 1$ and this rescales to $\sim 1590^\circ\text{C}$ which is much below the melting point of alumina which is 2200°C . As N increases, the difference in the maximum and the minimum temperature of the solutions decreases. As a result of Riemann-Lebesgue Lemma, the increase in number of oscillations with N causes cancellations. This reduces temperature variations along the ceramic slab. This suggests that in the limit as $N \rightarrow \infty$, an averaged temperature can be obtained which is almost constant along the slab. These observations support the experimental evidence that the temperature is more uniform when the electric field propagating within the ceramic material has a larger modal number.

The curves in Figures 2.6 and 2.7 are S-curves for $N = 1, 2$ and $N = 3, 4$ respectively relating maximum temperature with power for seven different values of D . For a fixed slab thickness d , different values of D are obtained by varying h_e , the

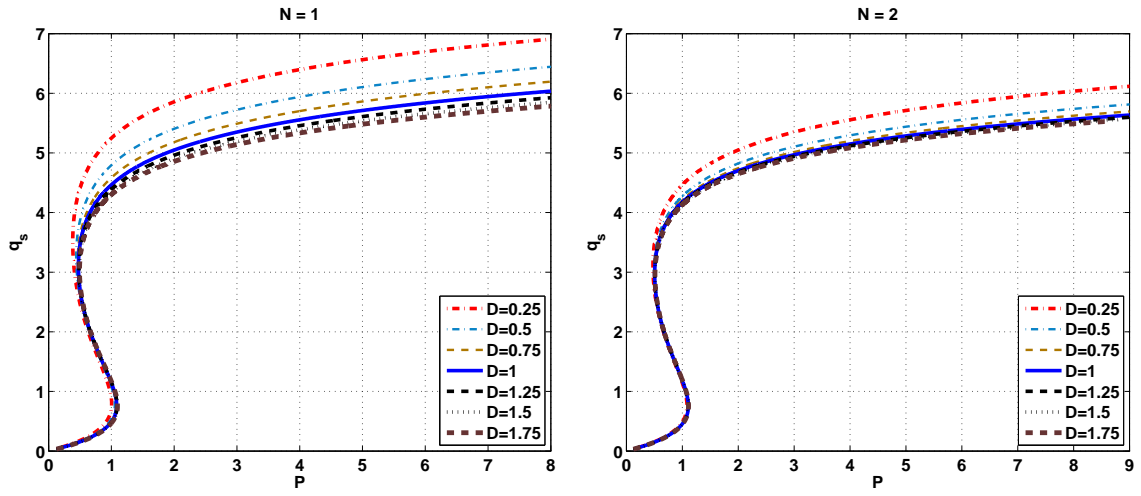


Figure 2.6 q_s as a function of P for several values of D , $N = 1, 2$.

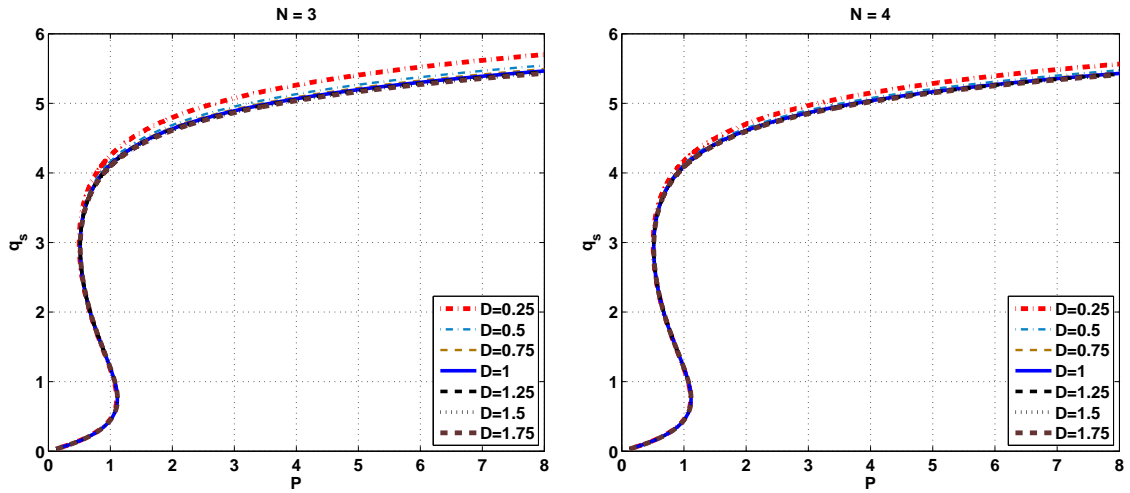


Figure 2.7 q_s as a function of P for several values of D , $N = 3, 4$.

effective heat transfer coefficient of the ceramic's surface. The maximum temperature increases as D decreases, i.e., as h_e decreases. This is due to the fact that less heat is removed from the slab for a smaller D .

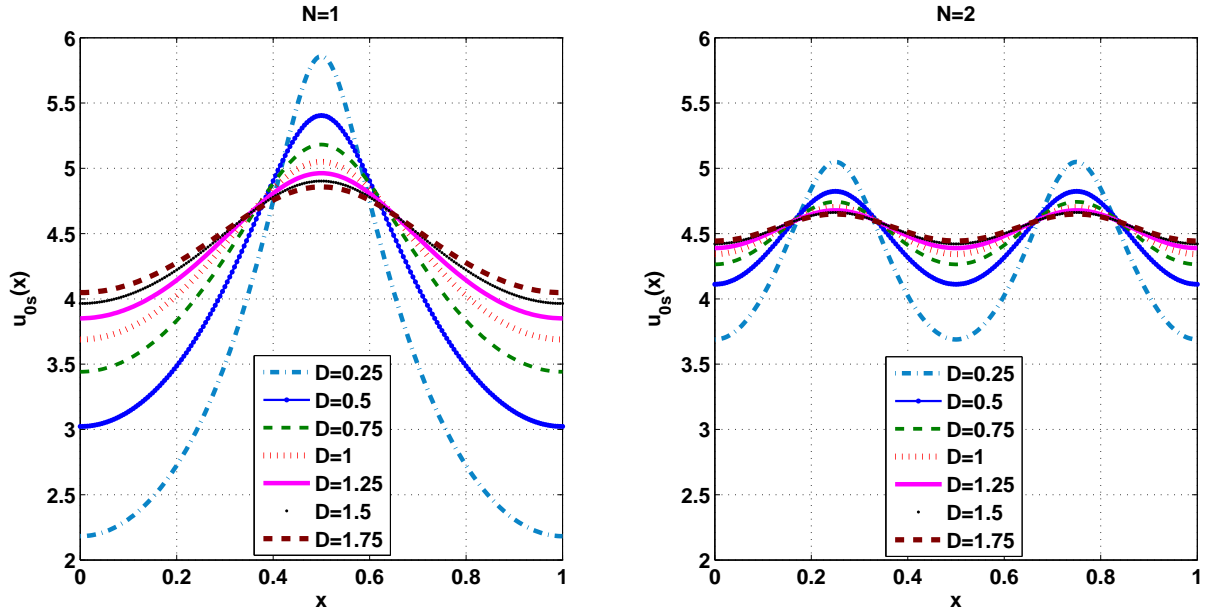


Figure 2.8 $u_{0s}(x)$ for $P \sim 2$, $N = 1, 2$.

Next, the stationary states for same seven values of D are plotted in Figures 2.8 and 2.9 when $P \sim 2$. The solutions become more localized as D decreases and this localization is interpreted as a hot-spot. For a fixed value of N , the number of hot spots is equal to N , the temperature is same at these hot spots and they are located at the local maxima of the source term. Although temperature localization increases as D decreases, not much variation is seen in temperature when N is big. This is again a consequence of Riemann-Lebesgue Lemma. Since the solutions for different values of D exhibit similar behaviour, therefore, for convenience $U_{0s}(x)$ is plotted only for $D = 1.75$. Solutions corresponding to this value of D will be analysed for stability for different powers in Section 2.3.

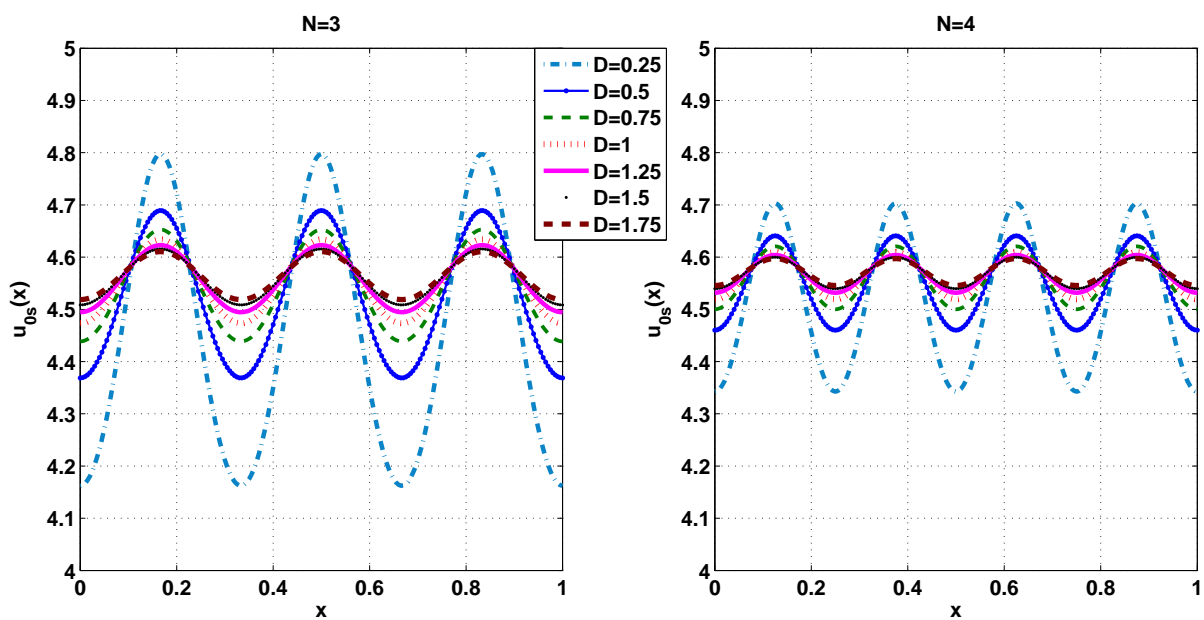


Figure 2.9 $u_{0s}(x)$ for $P \sim 2$, $N = 3, 4$.

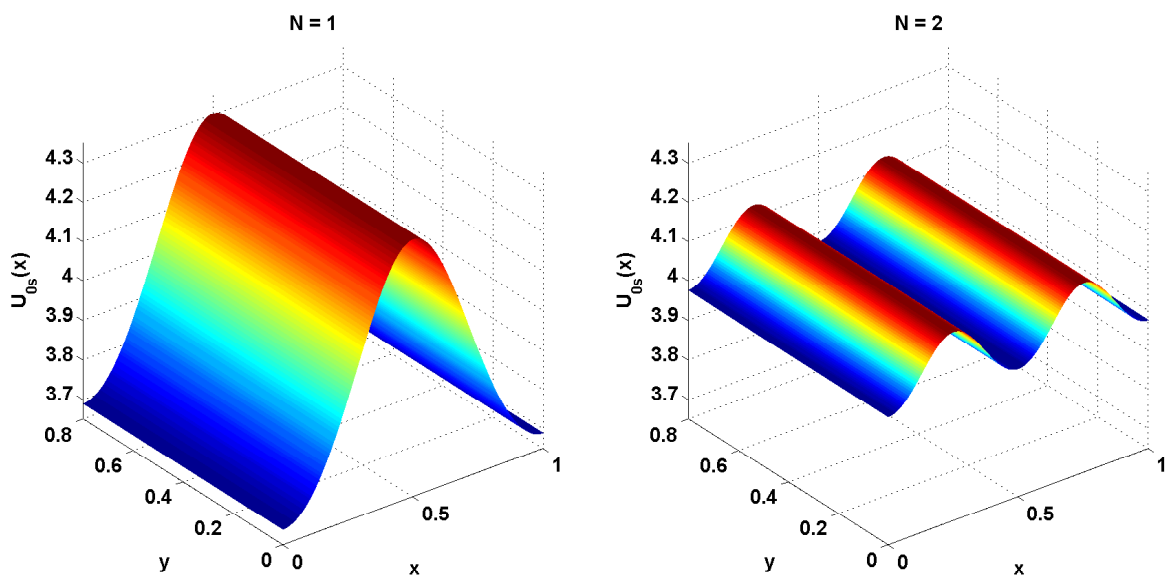


Figure 2.10 $U_{0s}(x)$ for $D = 1.75$, $N = 1, 2$, $P \sim 1$, upper branch.

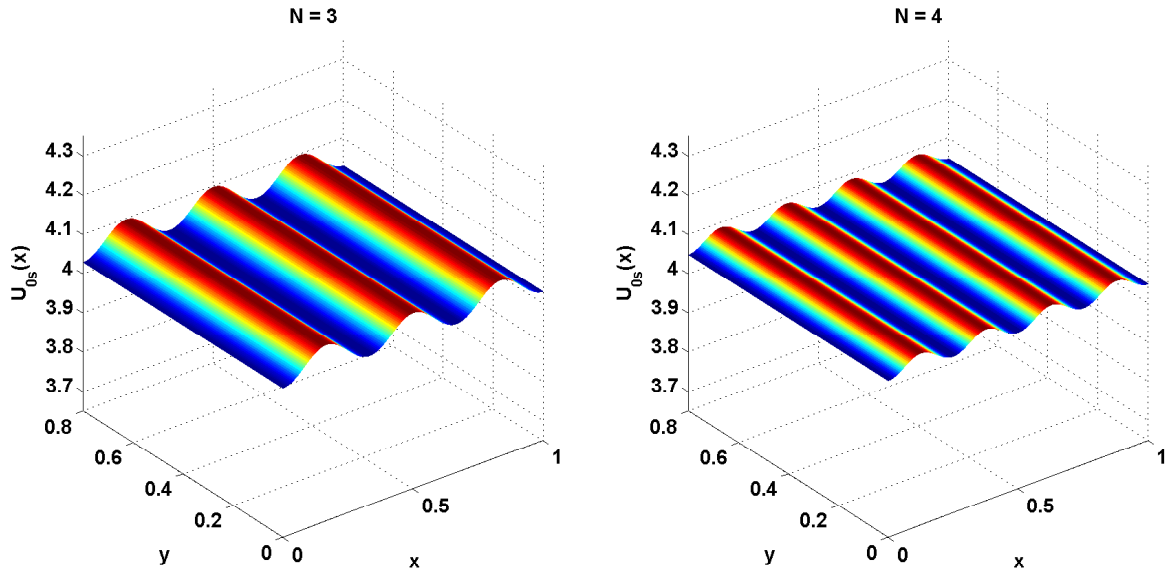


Figure 2.11 $U_{0s}(x)$ for $D = 1.75, N = 3, 4, P \sim 1$, upper branch.

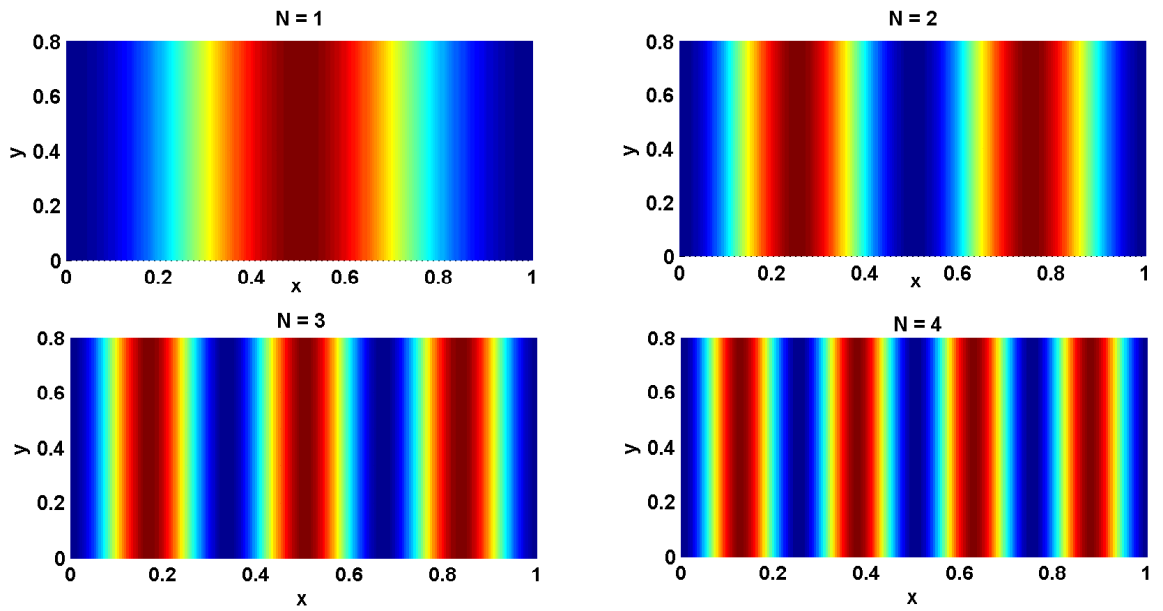


Figure 2.12 Top view of the stationary solutions when rotated at 90 degrees. The solutions admit a stripe like structure.

Figure 2.10 and 2.11 represent $U_{0s}(x)$ for $P \sim 1, D = 1.75$ for $N = 1, 2$ and $N = 3, 4$ when solutions have reached upper branches of curves in Figure 2.4. The steady states have a striped structure and the number of stripes is the same as value of N . Figure 2.12 is a top view of solutions when solutions in Figures 2.10 and 2.11 are rotated at 90 degrees. This shows how the temperature varies on the surface of the slab. Red represents the hottest part of the slab and blue represents the part where temperature is minimum. In each case there are N stripes in a position symmetric about $x = \frac{1}{2}$. The maximum temperature increases on moving up along the branches. Stationary solutions for $N = 2, 3, 4$ at powers 0.65, 1 and 3 exhibit different stability properties and it will be enough to study the stability of solutions at these powers to understand the stability of solutions for other powers also. Before moving on to stability, the very interesting asymmetric stationary solutions to equation (2.3a,b) are found in the next section.

2.2.2 An Asymmetric Stationary Solution

The method in Kriegsmann[13] was used to find the asymmetric branch of the steady states. Symmetry was not assumed as in [13] and therefore, the solutions were approximated on the full interval instead of half interval. The initial guesses were taken at $x = 0$.

The curves in Figure 2.13 depict maximum temperature q_a of the asymmetric stationary solution as a function of microwave power for $D = 1.75$. The S-shaped curve for $N = 1$ is different from those for $N > 1$. This is because there are no asymmetric solutions for $N = 1$ case and both methods (one for finding symmetric solutions and the other for finding asymmetric solutions) produce the same symmetric solution. But for $N > 1$, there are asymmetric solutions and the S-curves for these solutions are as in Figure 2.13. Contrary to the symmetric case, it is observed that

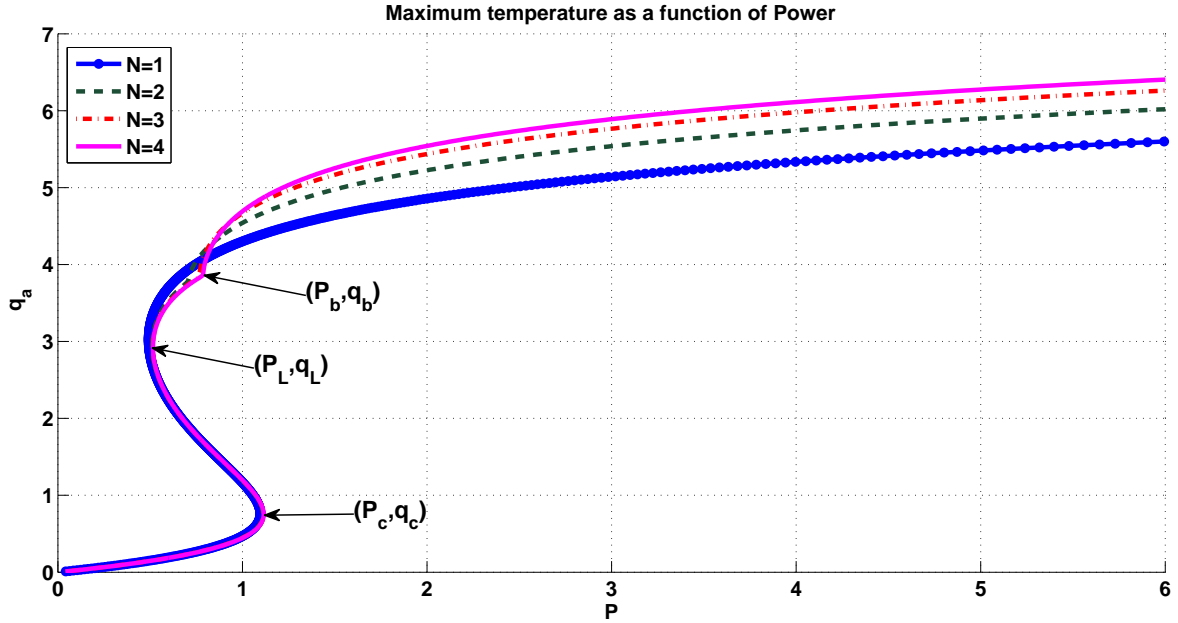


Figure 2.13 q_a as a function of P for $D = 1.75$.

on the upper branch, maximum temperature increases as N increases. This suggests that stability decreases with increasing N .

In Figure 2.14 steady state temperature $u_{0a}(x)$ has been plotted as a function of x for $P \sim 1$ corresponding to lower, middle and upper branches of curves in Figure 2.13. On the upper branch, the maximum temperature increases as N increases and the temperature distribution is no more symmetric about $x = \frac{1}{2}$. This also shows that increasing the electric field modal number makes the temperature more uniform as long as solutions stay on the symmetric branch. On the asymmetric branch, the non-uniformity in temperature increases with N . The maximum of the asymmetric solution is to the left of the center of the slab. This is purely due to numerical noise. If there is a stationary solution with a local maximum at $x_0 \in [0, \frac{1}{2}]$, then there is another stationary solution with a local maximum at $1 - x_0$. This solution can be found numerically if the initial guesses are taken at $x = 1$ instead at $x = 0$. Thus, the stationary solution at x_0 is unique up to a mirror image at $1 - x_0$. Also, for a given solution, there is only one local maximum, whatever the value of N maybe.

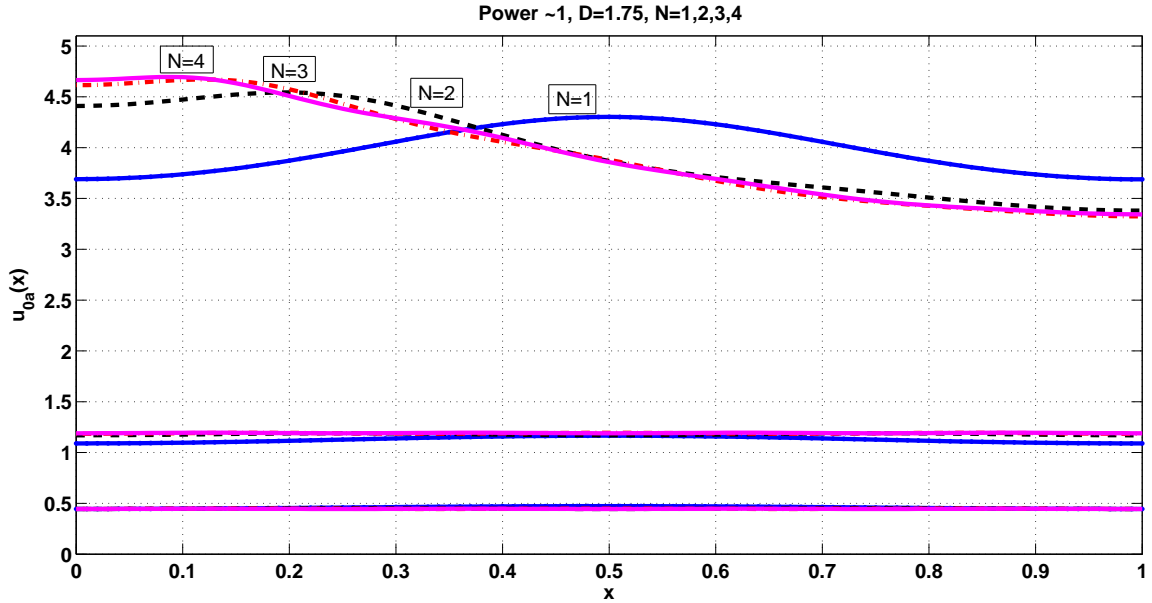


Figure 2.14 Steady state temperature u_{0a} as a function of x for $P \sim 1, D = 1.75$ in three branches.

This maximum is always on one side and cannot be in the center since the solutions are on the asymmetric branch.

Next, in Figures 2.15 and 2.16, q_a as a function of P has been plotted for seven different values of D . As in the symmetric case, temperature localization and q_a increase as D decreases. This shows that the asymmetric solutions also become more unstable as D decreases. The curves for $N = 1$ are the same as in the symmetric case while in other cases the curves deviate at the bifurcation point where the solutions split into symmetric and asymmetric solutions.

Figure 2.17 indicates bifurcation points (P_b, q_b) when $N = 2, 3$ for smallest and the largest values of D among the values considered in this chapter. The solutions are symmetric on both branches until (P_b, q_b) and deviate into symmetric and asymmetric branches beyond this point. The solutions on asymmetric branch have a higher maximum temperature for the same value of power as compared with solutions on the symmetric branch. For the same value of N , bifurcation occurs earlier on the S-curve for a smaller value of D . This suggests that stability decreases with D .

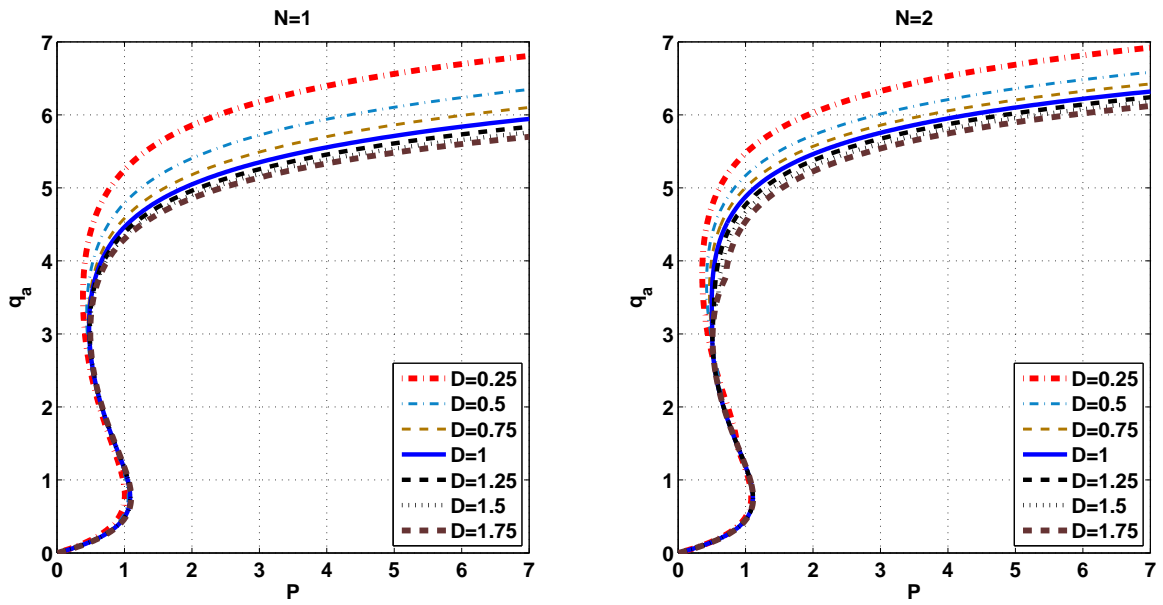


Figure 2.15 q_a as a function of P for several values of D , $N = 1, 2$.

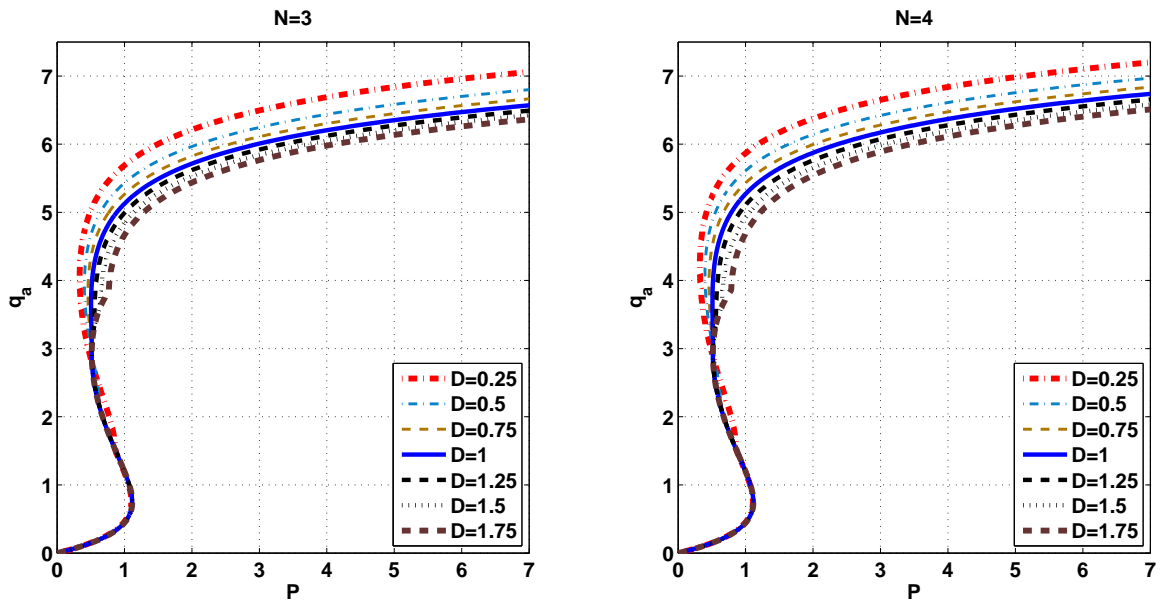


Figure 2.16 q_a as a function of P for several values of D , $N = 3, 4$.

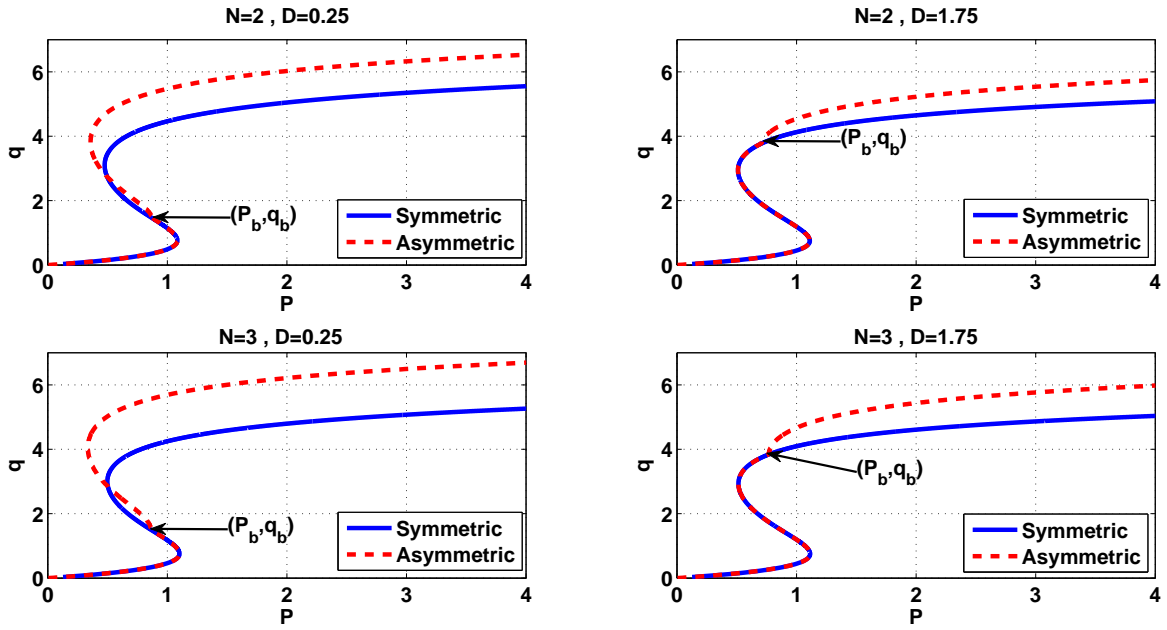


Figure 2.17 Symmetric and asymmetric branches.

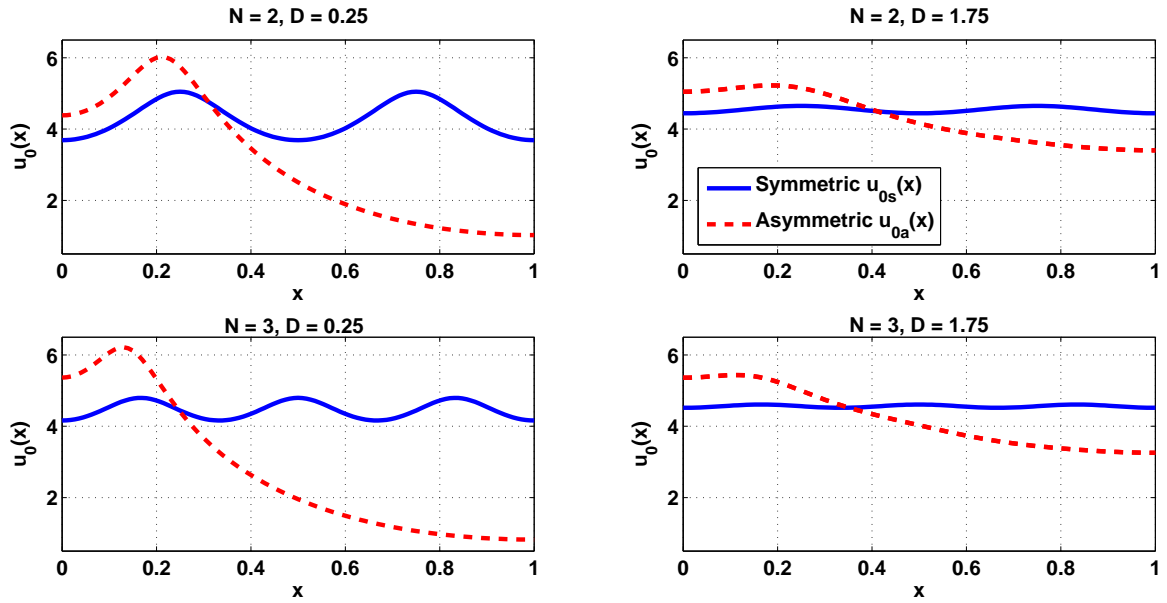


Figure 2.18 $u_{0s}(x)$ and $u_{0a}(x)$ for $D = 0.25, 1.75, P \sim 2$.

These observations show that to obtain a stable symmetric solution, D should be chosen large enough so as to stay on the symmetric branch.

Symmetric and asymmetric stationary solutions for $P \sim 2$ have been plotted in Figure 2.18 for $N = 2, 3$ and $D = 0.25, 1.75$. Clearly, the asymmetric solutions have a higher maximum temperature for the same value of power. Both symmetric and asymmetric solutions are more localized for a small value of D since less heat is allowed to escape from the slab while they are flatter for a bigger value of D . For a higher value of N , symmetric solutions are more uniform while the asymmetric solutions are more non-uniform. That is, as N is increased, the difference in maximum and minimum temperatures of solutions decreases in the symmetric case while this difference increases in the asymmetric case.

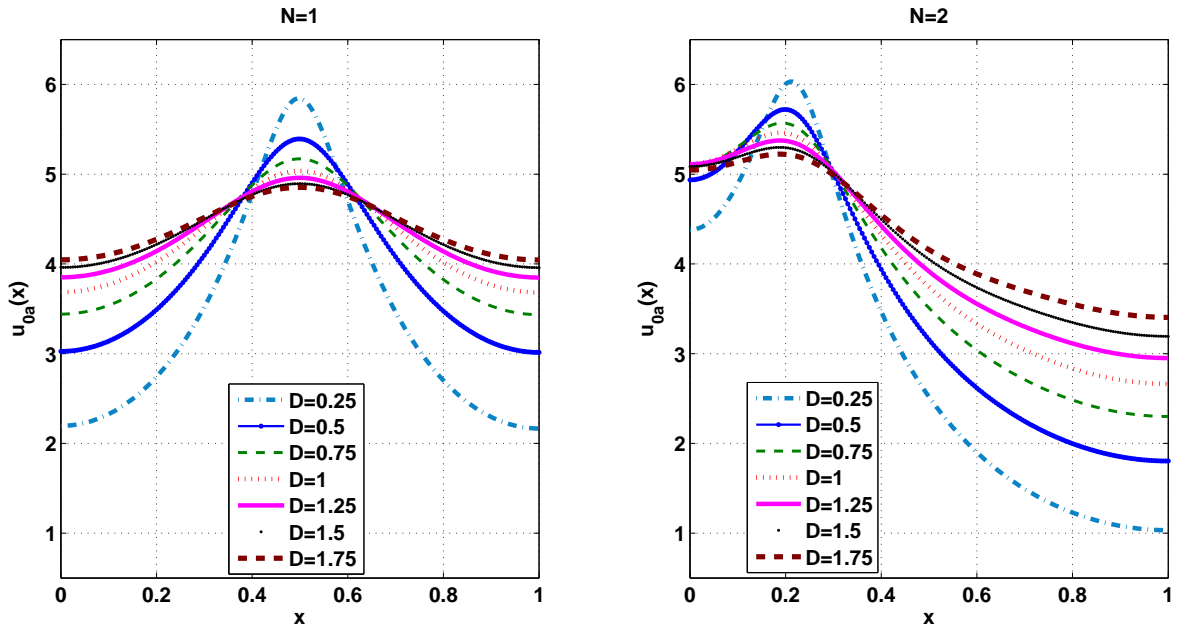


Figure 2.19 $u_{0a}(x)$ for $P \sim 2, N = 1, 2$.

Figures 2.19 and 2.20 are plots of asymmetric stationary solutions for $P \sim 2$ for seven different values of D . As in the symmetric case, not only does the maximum of solutions increase, but the solutions become more localized as D decreases. In

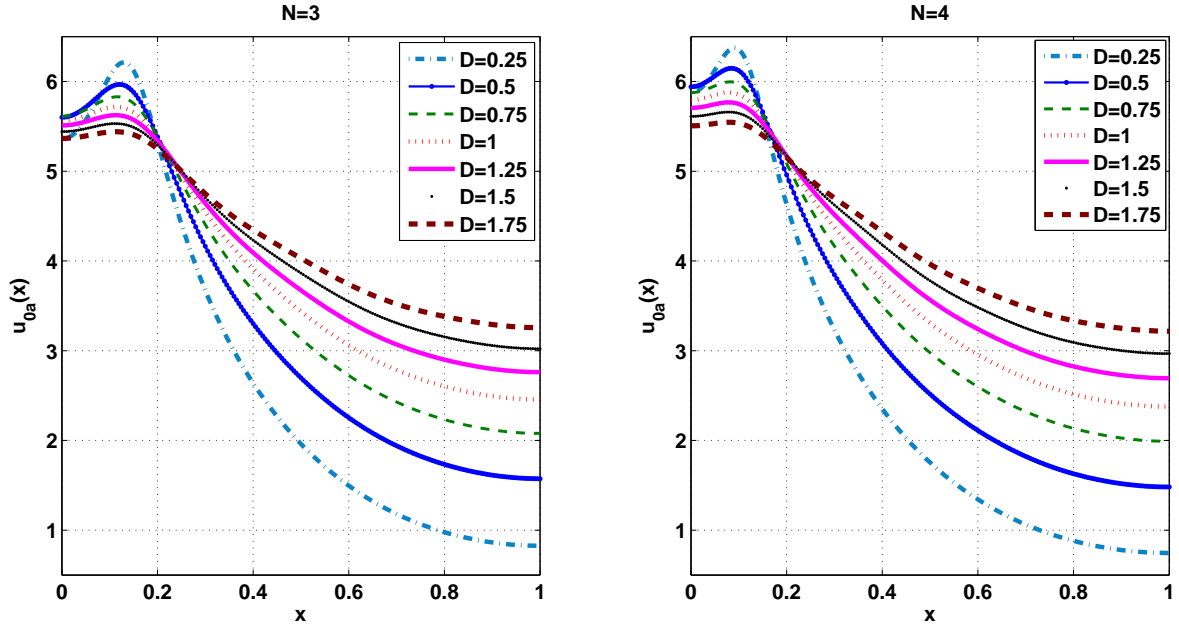


Figure 2.20 $u_{0a}(x)$ for $P \sim 2, N = 3, 4$.

contrast to the symmetric case, maximum temperature and asymmetry and therefore, non-uniformity of solutions increase with N on the asymmetric branch.

Figures 2.21 and 2.22 are the asymmetric stripes $U_{0a}(x)$ for $N = 1, 2$ and $N = 3, 4$ respectively when $P \sim 0.65$. This value of power is just a little before the bifurcation point and the solutions are purely on the symmetric branch.

When the power is increased slightly to $P \sim 0.8$, a bifurcation occurs for $N > 1$ and the solutions move to the asymmetric branch as shown in Figures 2.23 and 2.24. The bifurcation occurs when $P \sim 0.71$ for $N = 2$, $P \sim 0.77$ for $N = 3$ and $P \sim 0.79$ for $N = 4$. Although the solutions lose symmetry when $P \sim 0.8$, more than one local maxima can be seen at this power since the point is close to the bifurcation point. Another interesting point to observe is that although on the asymmetric branch maximum temperature increases with N , for this value of power the maximum temperature is decreasing with N because this point is very close to the symmetric branch.

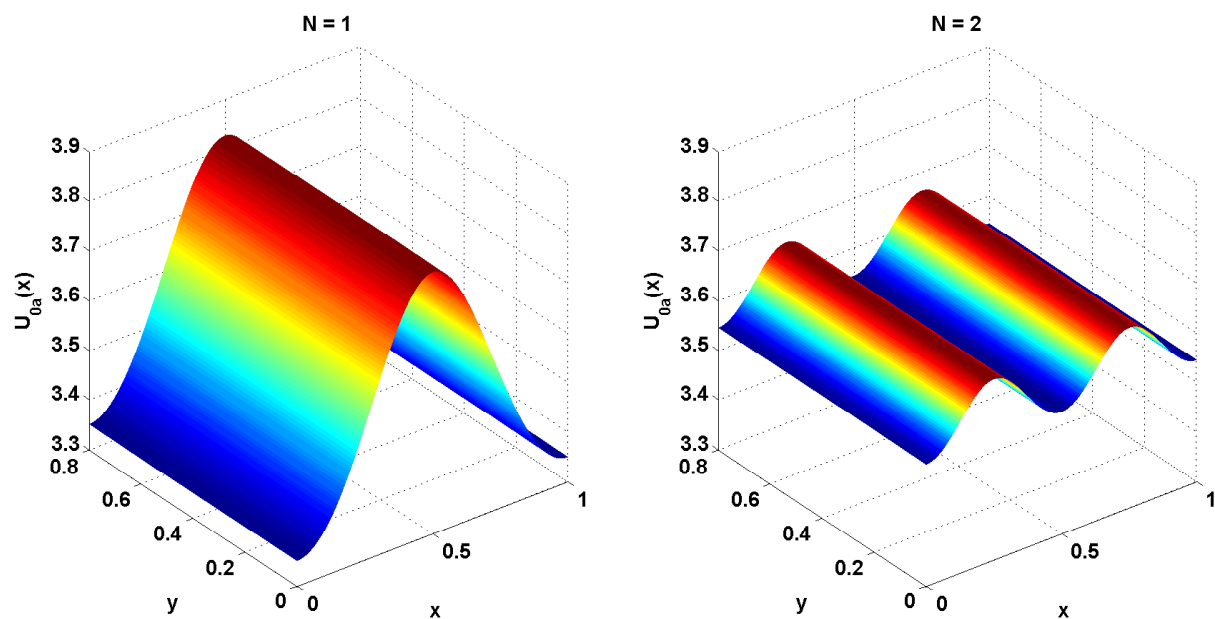


Figure 2.21 $U_{0a}(x)$ for $D = 1.75, P \sim 0.65, N = 1, 2$, upper branch.

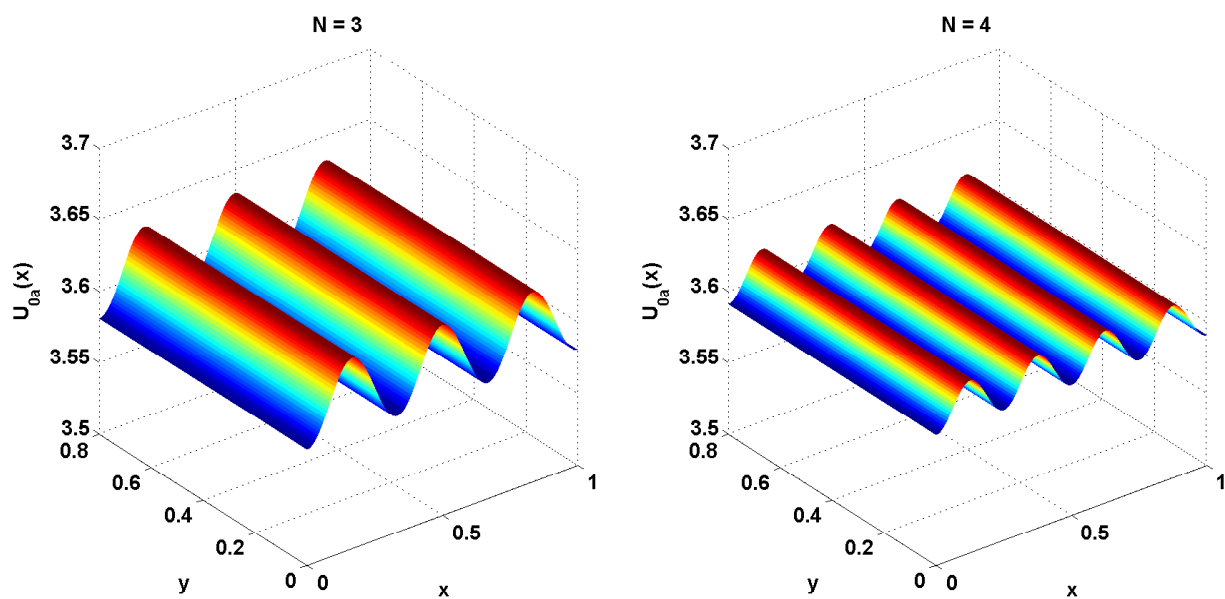


Figure 2.22 $U_{0a}(x)$ for $D = 1.75, P \sim 0.65, N = 3, 4$, upper branch.

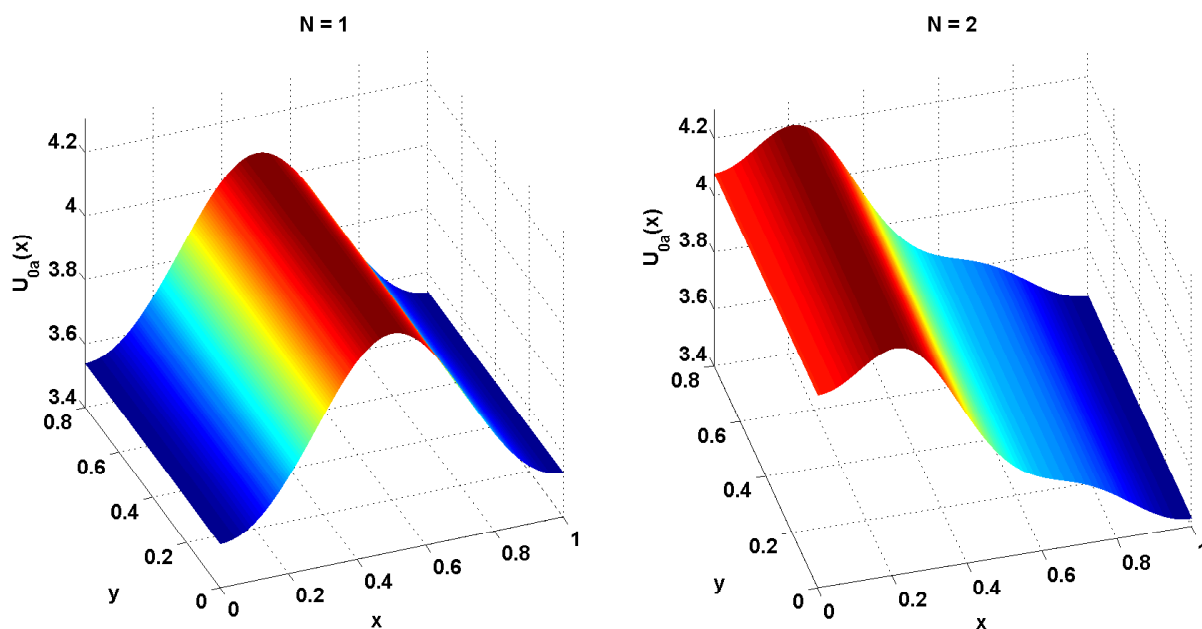


Figure 2.23 $U_{0a}(x)$ for $D = 1.75, P \sim 0.8, N = 1, 2$, upper branch.

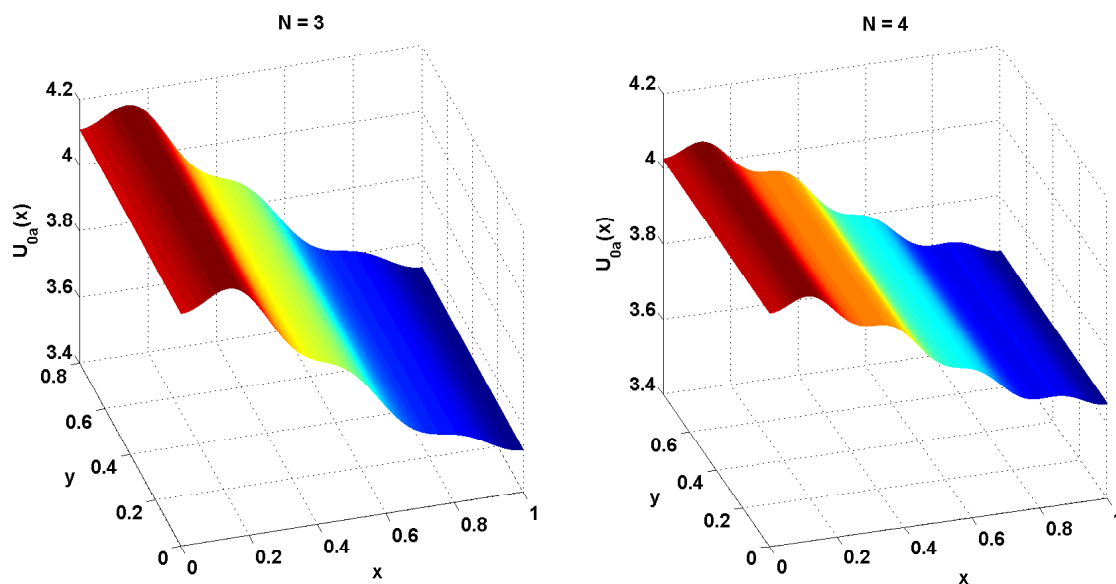


Figure 2.24 $U_{0a}(x)$ for $D = 1.75, P \sim 0.8, N = 3, 4$, upper branch.

When power is increased further to 1 as depicted in Figures 2.25 and 2.26, the oscillations are negligible and only one local maxima is observed whatever the value of N may be. The asymmetry increases with power and no oscillations are seen further away from the bifurcation point. The solutions have acquired all the characteristics of the asymmetric solution and now the maximum temperature is increasing with N . On the asymmetric branch, the solutions cannot handle more than one maxima and all the heat moves to one side of the slab. This is because electromagnetic heating is preferential.

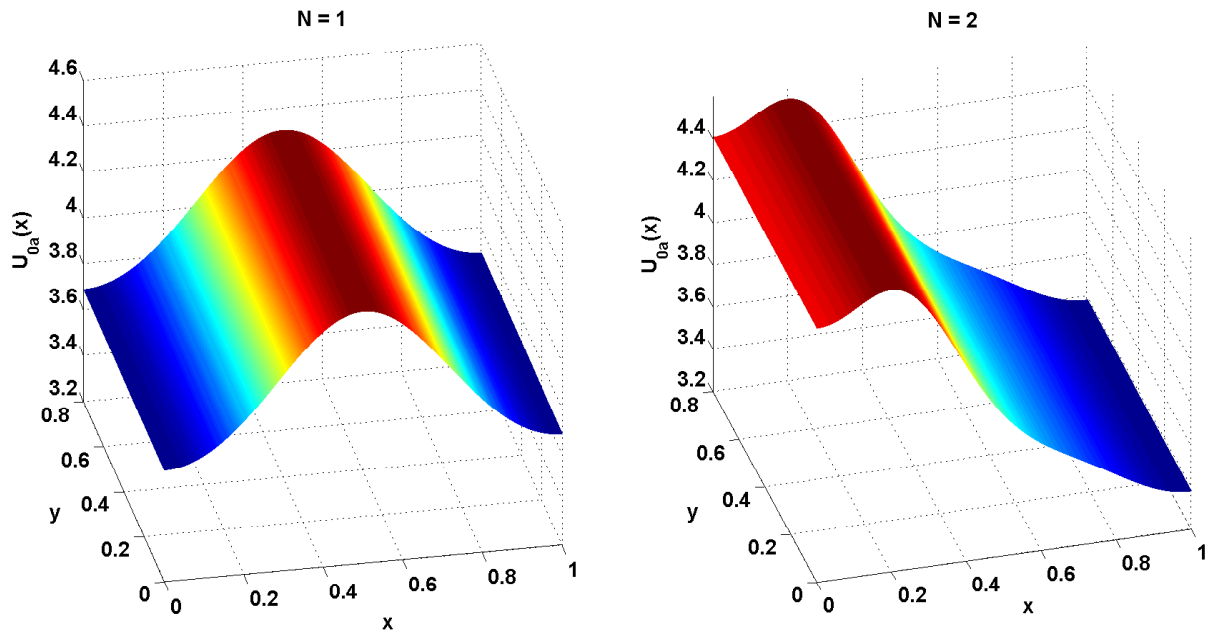


Figure 2.25 $U_{0a}(x)$ for $D = 1.75, P \sim 1, N = 1, 2$, upper branch.

The next question of interest is what happens to the solutions after a long period of time. Next section deals with the stability of these solutions as they evolve in time. The solutions at powers 0.65, 1, 3 for $D = 1.75, N = 2, 3, 4$ have different stability properties and it will be enough to study the stability of solutions at these powers to understand the behaviour of solutions at other powers also.

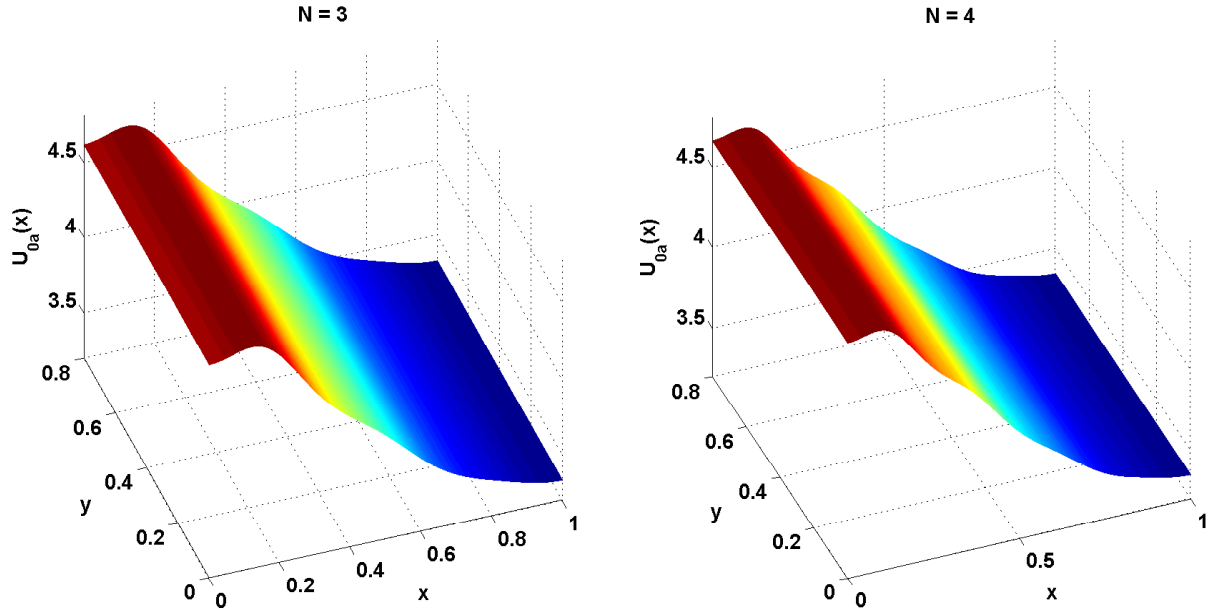


Figure 2.26 $U_{0a}(x)$ for $D = 1.75, P \sim 1, N = 1, 2$, upper branch.

2.3 Linear Stability

It will be interesting to determine whether the striped solutions found in the previous section are stable to perturbations in time. To analyze the stability of this stripe, let $U(x, y, t) = u_0(x) + V(x, y)e^{-\Lambda t}$, where Λ are the eigen-values. The eigen-values are a function of the dimensionless diffusion coefficient D and the modal number N . The behaviour of the most sensitive eigen-values is tracked as these parameters vary. The sign of Λ will determine whether the solution is stable or unstable as it evolves in time. Inserting the above expression for U in equation (2.1a) yields:

$$D\nabla_{\perp}^2 V + [\Lambda - 2\dot{L}(u_0) + C\Gamma g(x)]V = \frac{2C\chi P}{Q^3}\mathcal{L}(V), \quad (2.10a)$$

$$\frac{dV}{dx} = 0, \quad x = 0, 1, \quad (2.10b)$$

where \dot{L} is the derivative of L with respect to its argument,

$$\mathcal{L}(V) = \frac{1}{h} \int_0^h \int_0^1 g(x)g(x')V(x', y')dx'dy', \quad (2.11a)$$

$$g(x) = \sin^2(N\pi x)e^{Cu_0(x)}, \quad (2.11b)$$

$$I_0 = \int_0^1 g(x)dx, \quad Q = 1 + \chi I_0, \quad \Gamma = \frac{P}{Q^2}, \quad (2.11c)$$

V can be expanded in the cosine series:

$$V(x, y) = \sum_{n=0}^{\infty} A_n(x) \cos\left(\frac{n\pi y}{h}\right). \quad (2.12)$$

Inserting the above expression for V in (2.10a) gives an eigen-value problem for A_n :

$$\frac{d^2 A_n}{dx^2} + [\Lambda - l_n^2 - 2\dot{L}(u_0) + C\Gamma g(x)]A_n = \delta_{n0} \frac{2C\chi P}{Q^3} \mathcal{L}(A_n), \quad (2.13a)$$

$$\mathcal{L}(A_n) = \frac{1}{h} \int_0^h \int_0^1 g(x)g(x')A_n(x')dx', \quad (2.13b)$$

$$\frac{dA_n}{dx}(0) = \frac{dA_n}{dx}(1) = 0, \quad (2.13c)$$

where δ_{n0} is the Kronecker delta and

$$l_n^2 = \frac{Dn^2\pi^2}{h^2}, \quad n = 0, 1, 2, \dots$$

The above eigen-value problem is non-local when $n = 0$, due to the presence of the inhomogeneous term on the right side of the equation. The non-local eigen-values determine the stability of solutions in x direction. The right hand side of equation (2.13a) vanishes when $n \geq 1$. These eigen-values determine how stable the solutions are when there is noise in y -direction also. In the case when $n = 0$, the following information about the eigen-values $\Lambda_{0j} = \lambda_j$ and eigen-functions $v_j, j = 0, 1, 2, \dots$ of equations (2.13a-c) is obtained from [13]:

1. Spectrum is real.
2. The eigen-values and eigen-functions can be divided into odd and even eigen-pairs

about $x = \frac{1}{2}$. Odd pairs: $(\lambda_{2n+1}, v_{2n+1})$ and even pairs: (λ_{2n}, v_{2n}) .

3. The spectrum is discrete and well ordered, i.e., $\lambda_0 < \lambda_1 < \lambda_2, \dots, \lambda_n < \lambda_{n+1} < \dots$

The above observations hold for eigen-values and eigen-functions of both symmetric and asymmetric stationary solutions. The two stationary solutions of the same equation possess very different stability properties. This will be demonstrated by looking at the eigen-values for each solution. The stability of symmetric state is dealt with first.

2.3.1 Linear Stability of Symmetric Stationary Solution

The eigen-pairs for the symmetric case are found using the symmetric stationary state $u_{0s}(x)$ in equation (2.10a). Positive eigen-value corresponds to a stable stationary solution whereas negative eigen-value represents an unstable one. An unstable solution here means that the solution evolves to a different state after sometime and does not come back to its original stationary state.

2.3.1.1 Case $n = 0$: Non-Local Eigen-values $\Lambda_{0j}^s = \lambda_j^s$. The non-local eigen-pairs are denoted by $(\lambda_j^s, v_j^s), j = 0, 1, 2, \dots$. When $P \ll 1$, a simple perturbation expansion of equation (2.13a) as $P \rightarrow 0$ yields

$$v_0^s = 1 + O(P), \quad \lambda_0^s = 2(1 + 4\beta) + O(P), \quad (2.14)$$

$$v_j^s = \sqrt{2} \cos(j\pi x), \quad \lambda_j^s = 2(1 + 4\beta) + Dj^2\pi^2 + O(P). \quad (2.15)$$

Newton's method described in Kriegsmann[13] has been used to determine λ_j^s as a function of q_s . The eigen-values and eigen-functions are computed using the values of P and $u_{0s}(x)$ found in Section 2.2.1. The linear stability of $u_{0s}(x)$ can be deduced for any (P, q_s) on the response curves in Figures 2.6 and 2.7.

In Figures 2.27, 2.28 and 2.29, the lowest non-local eigen-value λ_0^s and the first odd non-local eigen-value λ_1^s have been plotted as a function of q_s for $D = 0.25, 1$ and

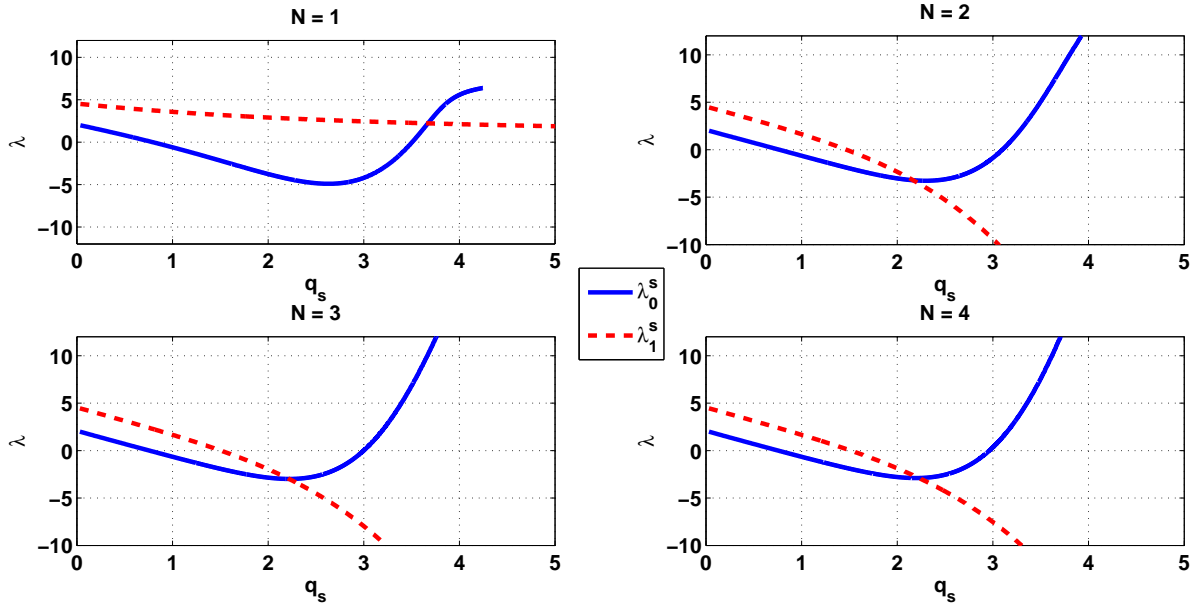


Figure 2.27 Lowest eigenvalue $\Lambda_{00}^s = \lambda_0^s$ and first odd non-local eigen-value $\Lambda_{01}^s = \lambda_1^s$ for $D = 0.25$.

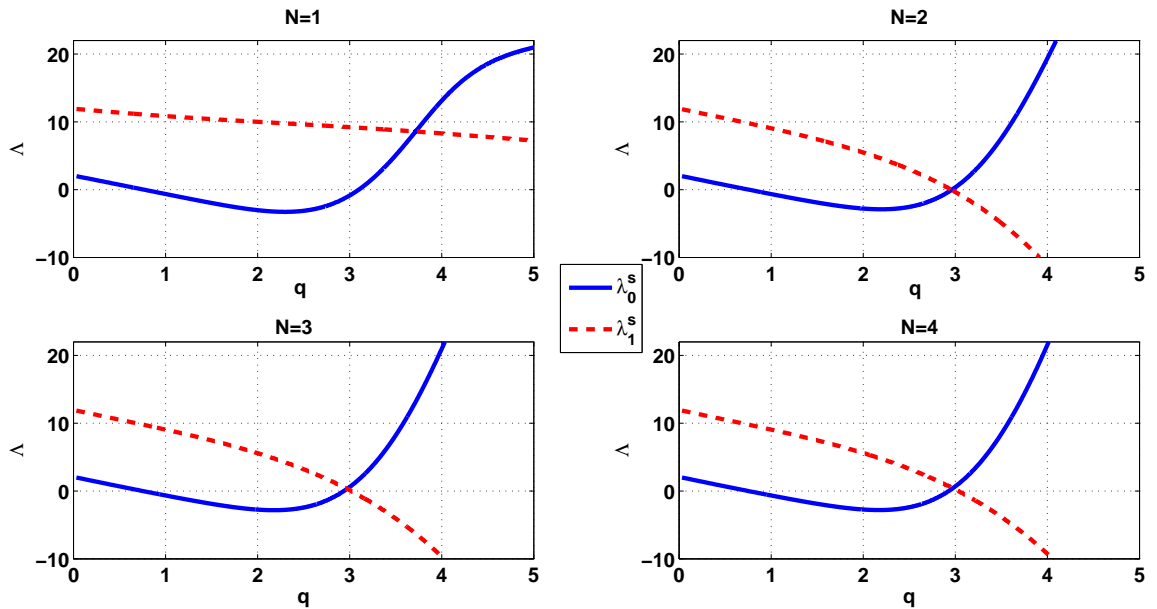


Figure 2.28 Lowest eigenvalue $\Lambda_{00}^s = \lambda_0^s$ and first odd non-local eigen-value $\Lambda_{01}^s = \lambda_1^s$ for $D = 1$.

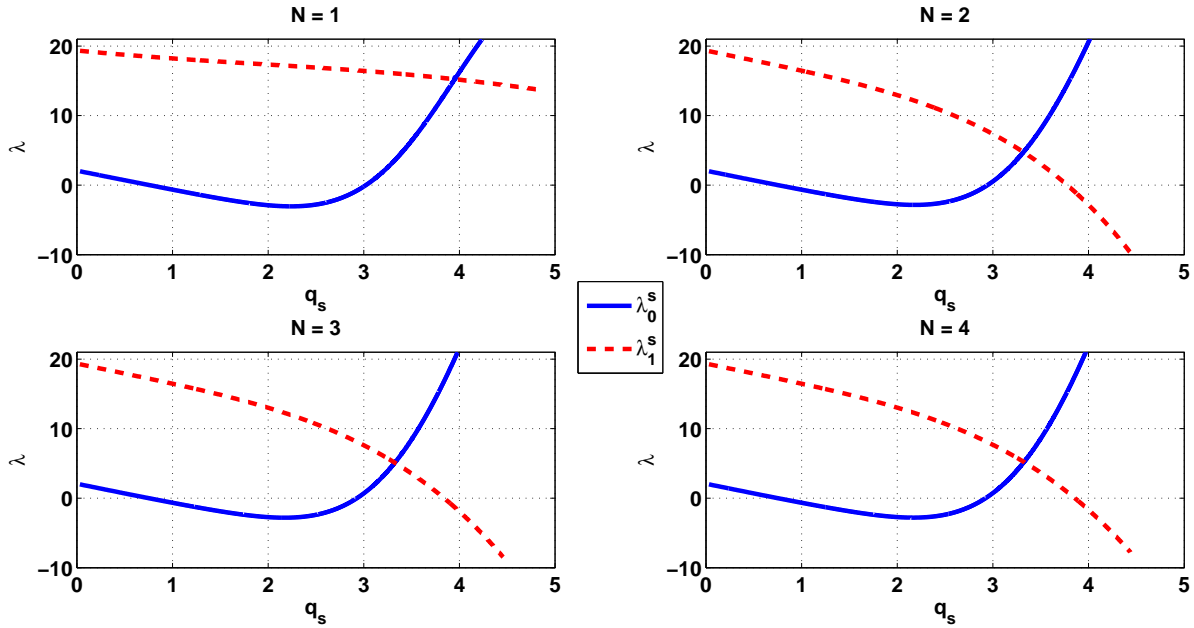


Figure 2.29 Lowest eigenvalue $\Lambda_{00}^s = \lambda_0^s$ and first odd non-local eigen-value $\Lambda_{01}^s = \lambda_1^s$ for $D = 1.75$.

$D = 1.75$ respectively. For each N , λ_0^s is negative on the middle branch ($P_L < P < P_c$). When $N \geq 2$, there is a special point (P_b, q_b) on the response curve at which λ_1^s becomes negative and stays negative. This is because a secondary bifurcation emerges at this point, which will be shown to be the asymmetric bifurcation. This phenomenon was not observed for $N = 1$. It should also be noted that when $D < 1$, λ_1^s becomes negative on the middle branch and stays negative. Therefore, for small values of D the symmetric stationary state is stable only on the lower branch. Whereas, when $D > 1$, the portion of the S-curve between (P_L, q_L) and (P_b, q_b) where both λ_0^s and λ_1^s are positive is stable.

The eigen-value λ_1^s being negative for $N > 1$ shows that the symmetric stationary solution $u_{0s}(x)$ is unstable for every $q > q_b$. This eigen-value has a simple zero $q_{01}^{*s}(D, N)$ for $N = 2, 3, 4$ and this zero is an increasing function of D and N . Note that when $N = 1$, this eigen-value is positive for all values of D . When $N > 1$, the

asymmetric bifurcation branch emerges at the point where λ_1^s is zero. This eigen-value distinguishes the case $N = 1$ from $N > 1$.

Several other λ_j^s were computed for different values of $N > 1$ and it was found that the odd eigen-values λ_j^s are negative for $j = 2k + 1 < N, k = 0, 1, 2, \dots$ and positive for $j = 2k + 1 \geq N$. For example, λ_3^s becomes negative at $q_s \sim 6.4$ for $N = 4$ which suggests that another asymmetric bifurcation branch emerges at this point in addition to the one at (P_b, q_b) . This supports the conjecture that the number of asymmetric bifurcations to the symmetric stationary solution increases with N . The determination of these branches is under further investigation.

2.3.1.2 Case $n \geq 1$: Local Eigen-values Λ_{nj}^s . The local eigen-values for the slab are obtained when the right hand side of equation (2.13a) vanishes when $n \geq 1$. This gives rise to an infinite number of uncoupled Sturm-Liouville problems for A_n . These problems are equivalent to the local eigen-value problems for the $n = 0$ case, that is equation (2.13a) with the right hand side set to zero. Thus, the eigen-functions for equations (2.13a-2.13b) are found by solving the local eigen-value problem and the eigen-values are:

$$\Lambda_{nj}^s = \mu_j^s(q_s, D, N) + \frac{Dn^2\pi^2}{h^2}, \quad j + 1, n = 1, 2, \dots, \quad (2.16)$$

where $\mu_j^s, j = 0, 1, 2, \dots$ depend on q_s , the point on the S-shaped curve in Figures 2.6, 2.7, the dimensionless diffusion constant D and N . Also, $\mu_1^s = \lambda_1^s$, which splits into a stable and an unstable portion as a function of q_s . Applying a similar shooting technique it was found that μ_0^s as a function of q is positive for $0 < q < q_c$ and negative for $q > q_c$, regardless of the value of D .

From equation (2.16) it is clear that the sign of Λ_{nj}^s will depend on $\mu_j^s(q_s, D, N)$ and D . Figures 2.30 and 2.31 depict curves for the first local eigen-value Λ_{10}^s as a decreasing function of q_s . This eigen-value has simple zeros $q_{10}^{*s}(D, N)$ for $N = 1, 2, 3, 4$

and these zeros are increasing functions of D and N . This eigen-value being negative shows that solutions become unstable to perturbations in y . Several other eigen-values were computed and it was found that when $N > 1$, Λ_{nj}^s has simple zeros for all n when $j < N, j = 0, 1, 2, \dots$ where N is the modal number of the incident electric field. On the other hand, when $j \geq N, N > 1$, then $\Lambda_{nj}^s, n \geq 1$ is positive. When $N = 1$, then the only unstable modes were $\Lambda_{n0}^s, n \geq 1$.

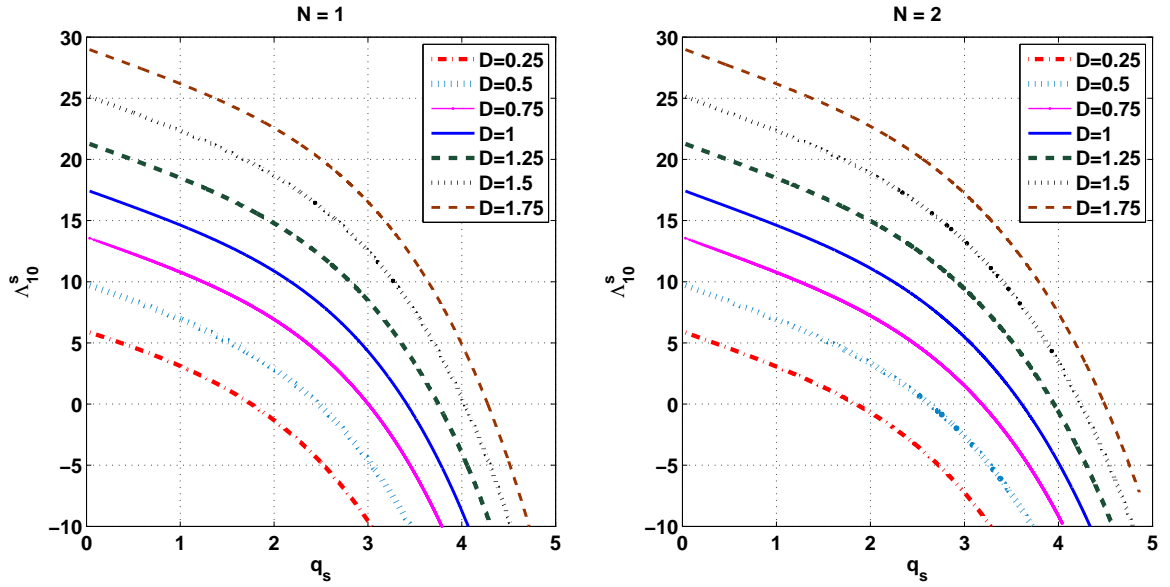


Figure 2.30 First local eigen-value Λ_{10}^s for $N = 1, 2$.

Table 2.2 Critical Points (P_{crit}, q_{crit}) at which modes become unstable, $D = 1.75$

N	λ_1^s	Λ_{10}^s
1	stable	(0.97, 4.28)
2	(0.71, 3.78)	(1.59, 4.49)
3	(0.77, 3.84)	(1.81, 4.54)
4	(0.79, 3.86)	(1.9, 4.56)

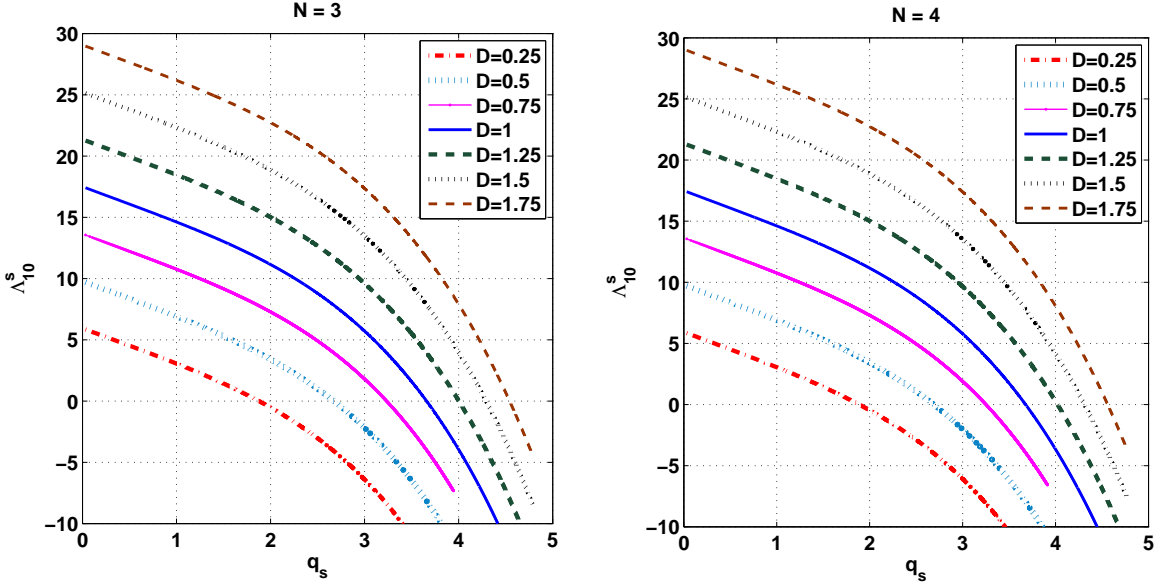


Figure 2.31 First local eigen-value Λ_{10}^s for $N = 3, 4$.

Table 2.2 gives the critical points at which the non-local mode λ_1^s and the local mode Λ_{10}^s become unstable for $D = 1.75$ and $N = 1, 2, 3, 4$. The above analyses show that $\Lambda_{0j}^s = \lambda_j^s$ becomes unstable when $q_s > q_b$ for $N \geq 2$. Many more modes become unstable when $N > 1$ as compared to the $N = 1$ case. This suggests that the symmetric solution is more unstable when $N > 1$ and the possibility of symmetric stripe becoming unstable is greater.

2.3.2 Linear Stability of Asymmetric Stationary Solution

Stability of asymmetric steady state is examined by looking at the eigen-values when $u_{0a}(x)$ is used in equation (2.10a) to find the eigen-values and eigen-functions.

2.3.2.1 Case $n = 0$: Non-Local Eigen-values $\Lambda_{0j}^a = \lambda_j^a$. The superscript a corresponds to asymmetric case. When $P \ll 1$, a simple perturbation expansion as

$P \rightarrow 0$ yields

$$v_0^a = 1 + O(P), \quad \lambda_0^a = 2(1 + 4\beta) + O(P), \quad (2.17)$$

$$v_j^a = \sqrt{2} \cos(j\pi x), \quad \lambda_j^a = 2(1 + 4\beta) + Dj^2\pi^2 + O(P). \quad (2.18)$$

Newton's method described in Kriegsmann[13] is now used to determine λ_j^a as a function of q_a . The eigen-values and eigen-functions are computed using the values of P and $u_{0a}(x)$ found in Section 2.2.2. The linear stability of $u_{0a}(x)$ can be deduced for any (P, q_a) on the response curves in Figures 2.15 and 2.16.

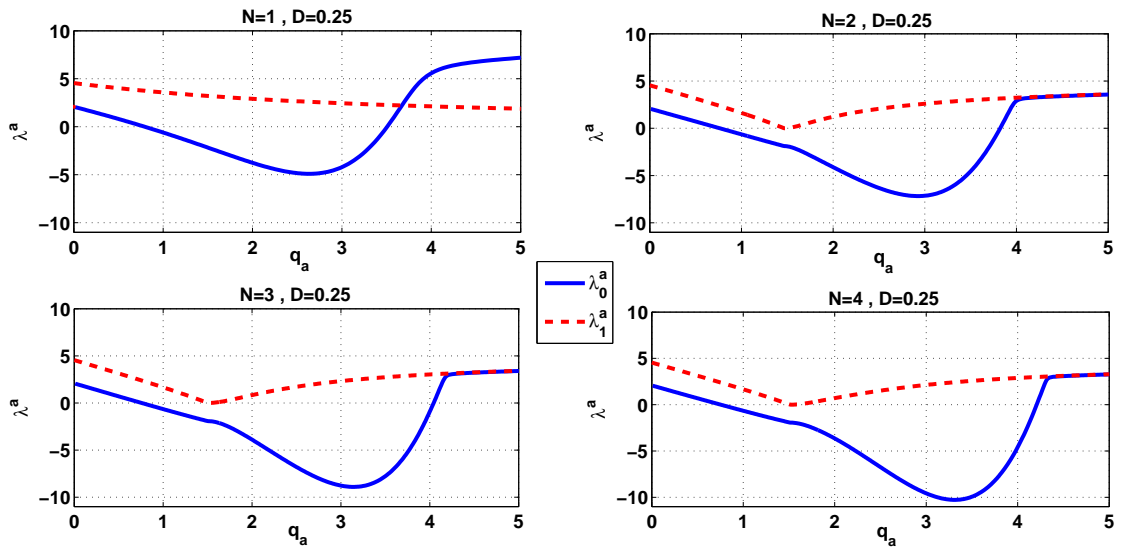


Figure 2.32 λ_0^a and λ_1^a for $D = 0.25$.

Lowest non-local eigen-value λ_0^a and the first odd non-local eigen-value λ_1^a have been plotted in Figures 2.32, 2.33 and 2.34 as a function of q_a for $D = 0.25, 1$ and 1.75 respectively. It was found that λ_0^a is negative on the middle branch ($P_L < P < P_c$) for each N . When $N \geq 2$, λ_1^a becomes zero at the point (P_b, q_b) on the response curve but then it is positive again. This is contrary to the symmetric case where λ_1^s becomes negative at the bifurcation point and stays negative. Several other λ_n^a were computed for different values of N and they were all positive for all values of N . Increasing or decreasing D did not change the qualitative behaviour of the eigen-values.

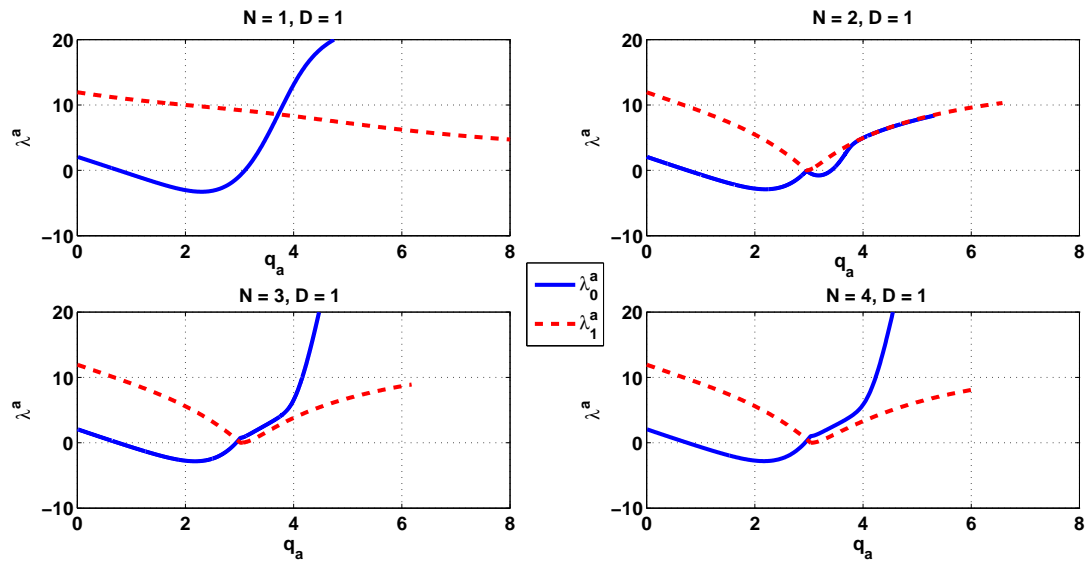


Figure 2.33 Lowest eigen-value λ_0^a and first odd non-local eigen-value λ_1^a for $D = 1$.

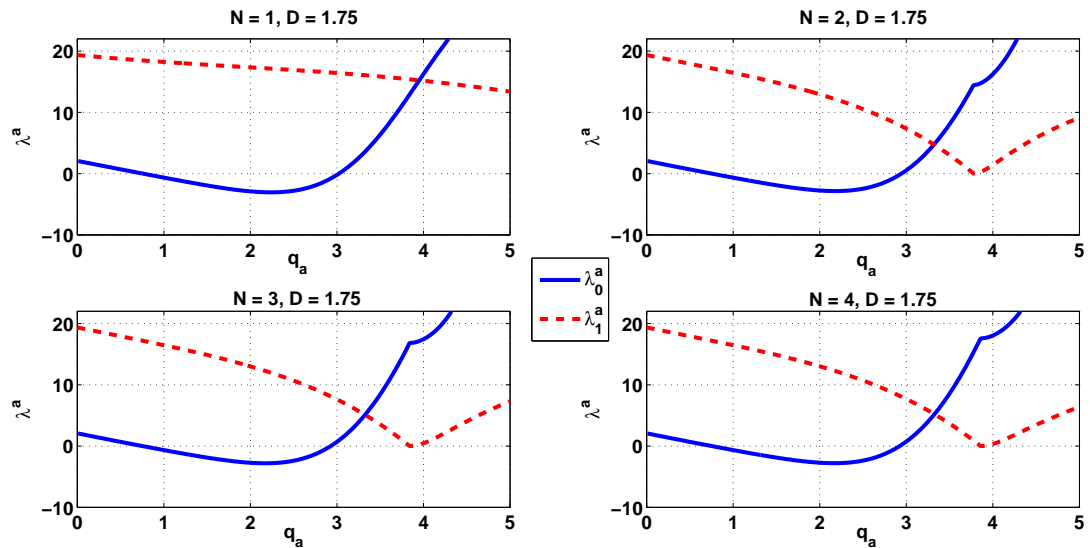


Figure 2.34 λ_0^a and λ_1^a for $D = 1.75$.

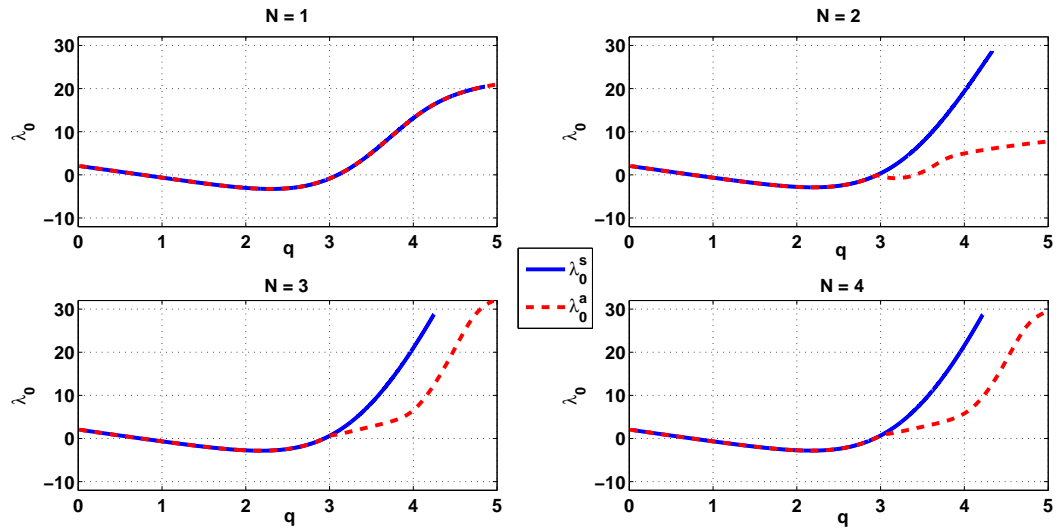


Figure 2.35 λ_0^s and λ_0^a for $D = 1$.

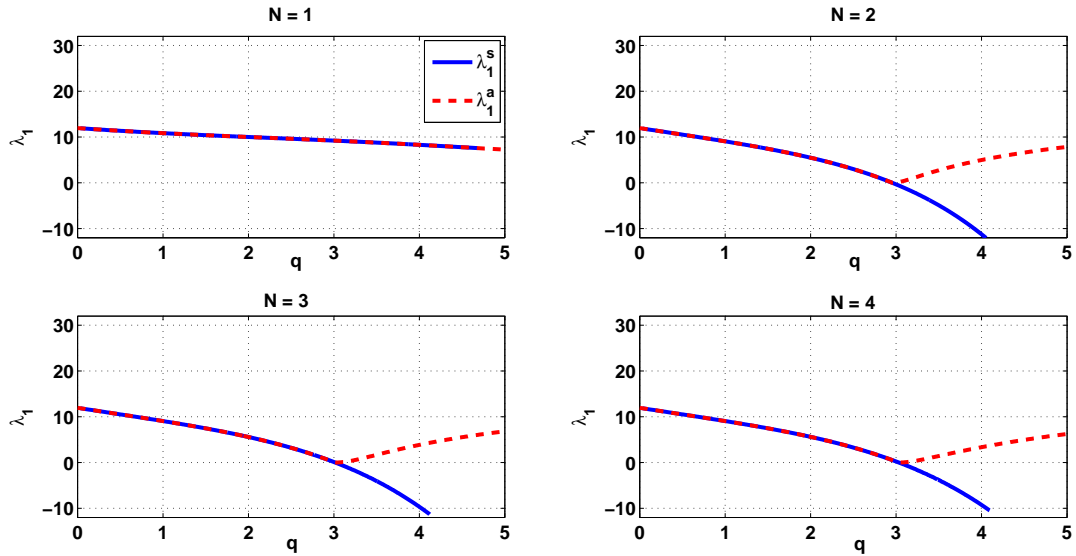


Figure 2.36 λ_1^s and λ_1^a for $D = 1$.

To summarize the behaviour of non local eigen-values for the symmetric and the asymmetric cases, both λ_0^s and λ_0^a are unstable in the middle branch for all values of N . The second non-local eigen-value λ_1^a is stable whereas λ_1^s is unstable beyond the bifurcation point. The comparison of eigen-values from symmetric with asymmetric cases has been shown in Figures 2.35 and 2.36.

2.3.2.2 Case $n \geq 1$: Local Eigen-values Λ_{nj}^a . The local eigen-values in the asymmetric case are given by

$$\Lambda_{nj}^a = \mu_j^a(q_a, D, N) + \frac{Dn^2\pi^2}{h^2}, \quad j + 1, n = 1, 2, \dots, \quad (2.19)$$

where μ_j^a $j = 0, 1, 2, \dots$ depend on q_a , the point on the S-shaped curve, the dimensionless diffusion constant D and the modal number N . From equation (2.19) it is evident that the sign of Λ_{nj}^a will depend on μ_j^a , the size of D and N . Also, $\mu_1^a = \lambda_1^a$. Figures 2.37 and 2.38 contain curves for the local eigen-value Λ_{10}^a as decreasing functions of q_a . The local eigen-values have simple zeros $q_{a10}^*(D, N)$ for $N = 1, 2, 3, 4$. As in the symmetric case, these zeros are increasing functions of D and N . The stability of many other modes was checked and it was found to be similar to stability of the modes for $N = 1$ case, i.e., the modes $\Lambda_{n0}^a, n \geq 1$ had simple zeros $q_{an0}^*(D, N)$ for $N = 1, 2, 3, 4$. The modes for $j \geq 1$ were stable.

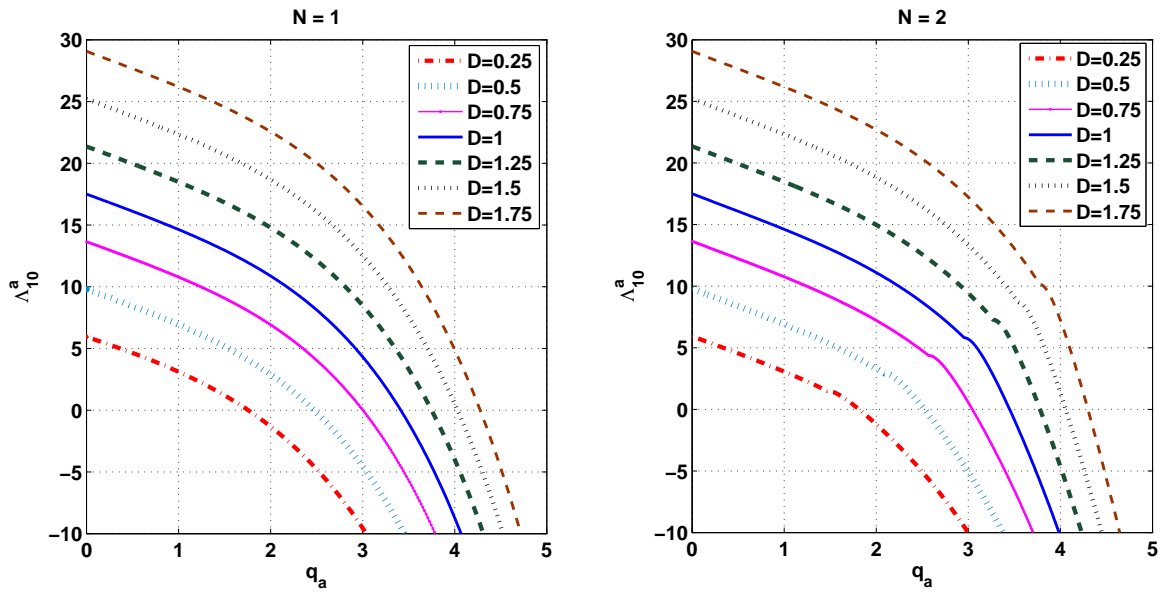


Figure 2.37 First local eigen-value Λ_{10}^a for $N = 1, 2$.

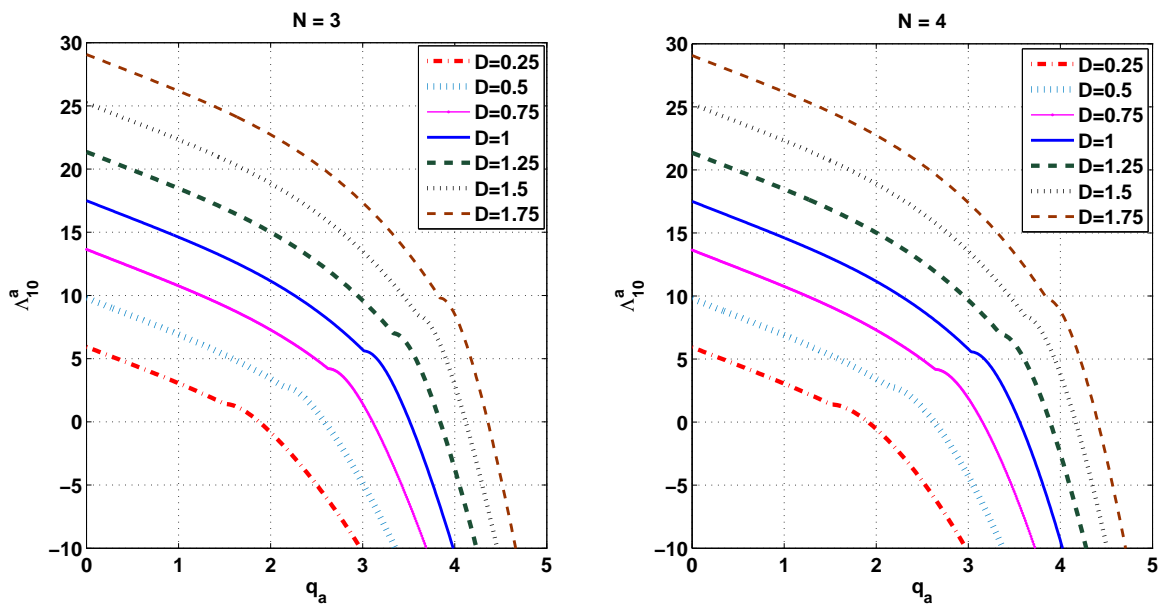


Figure 2.38 First local eigen-value Λ_{10}^a for $N = 3, 4$.

2.4 Dynamical Simulations

Eigen-values $\lambda_0^s, \lambda_1^s, \Lambda_{10}^s, \lambda_0^a, \lambda_1^a$ and Λ_{10}^a becoming negative suggests that the symmetric stripe solution $U_{0s}(x)$ and the asymmetric stripe solution $U_{0a}(x)$ are unstable to certain choices of P and D . An explicit two-dimensional finite difference scheme was developed to approximate the solutions of equation (2.1a-e). Time evolution of solutions for $N = 1, 2, 3, 4$ were analyzed for different values of power. Since the qualitative behaviour of solutions is the same for all $N \geq 2$, therefore, solutions corresponding to $N = 2$ are studied in greater detail. The critical points for different eigen-values are spread out on the S-curve for a large D . This facilitates in the analysis of solutions and since $D = 1.75$ serves this purpose, the solutions will be studied in detail for this value of D . The other parameters are fixed as before :- $\chi = \beta = 0.01, C = 1.5$.

An oval hot spot symmetric about x was observed in the center of a thin aluminium slab in the experiments done by Brodwin and Johnson for $N = 1$ case. The observations were proved mathematically for this case by Kriegsmann[13] where the formation of hot spots was related to one or more modes becoming unstable due to preferential electromagnetic heating. It was expected that two such hot spots would be observed in the simulations for $N = 2$, three for $N = 3$ and so on. But only one hot spot formed in a position asymmetric about x whatever the value of N maybe. This difference in the evolution of symmetric steady states for $N \geq 2$ was because the symmetric state was not as stable as the asymmetric state. When $N \geq 2$, all the heat moves to one side of the slab, again because electric field distribution causes preferential heating.

The difference between symmetric steady states for $N = 1$ and $N \geq 2$ is explained mathematically by looking at the first odd non-local eigen-value λ_1 . This eigen-value is positive for $N = 1$ but negative for $N \geq 2$ beyond the special point (P_b, q_b) since the symmetric steady state for $N \geq 2$ is unstable beyond this point.

Another asymmetric bifurcation branch emerges at (P_b, q_b) which is more stable than the symmetric stationary states. The bifurcation point moves up on increasing D which means that stability increases with D .

Several different sets of initial data were chosen to study the time evolution of solutions to equations (2.1a-d) and to understand the dynamics of the heating process. First, homogeneous initial data were chosen for different values of power. When $P < P_c$, initial data evolved to the symmetric stationary state corresponding to the lower branch. On the other hand, when $P > P_c$, initial data evolved to symmetric steady state on the upper branch if $P_c < P < P_b$ for $N \geq 2$. When $P > P_b$, the solutions first reached the symmetric steady state on the upper branch but finally evolved to the asymmetric steady state. Even when the power was big enough, there was not enough numerical noise to trigger an instability in the y direction. Numerical noise could only excite the asymmetric mode Λ_{01}^s in x and the initial data evolved to the asymmetric steady state.

When the homogeneous initial data were replaced by a function that varied in y , then the initial data evolved to stationary states as the previous case if $P < P_c$ or $P < P_{10}$, where P_{10} is the power at which Λ_{10}^s becomes unstable. On the other hand, when $P > P_{10} > P_c$, then a spike was observed at one of the y boundaries. If the maximum of the initial data was to the left of $h/2$, then the spike was formed on the lower y boundary, otherwise the spike was formed on the upper y boundary.

Next, the homogeneous initial data were replaced by the symmetric stationary solution $U_{0s}(x)$ and the corresponding power on the S-shaped curves in Figures 2.6, 2.7. It took a shorter time to reach the same final state. For $N = 2$, Λ_{01}^s becomes unstable when $P \sim 0.71 (= P_b)$. In simulations with $P < 0.71$, any initial data whether symmetric or not about $x = \frac{1}{2}$ that averaged to stationary solutions corresponding to the upper branch evolved to the symmetric states on the upper branch. On the other hand, when $P > 0.71$, initial data that smoothed out to

symmetric states corresponding to the upper branch evolved to asymmetric stationary states corresponding to the same value of power. If the average was closer to the stationary states on the lower branch, then the initial data evolved to the lower branch solutions for $0.71 < P < P_c$. When $P > P_c$, any initial data evolved to asymmetric steady state.

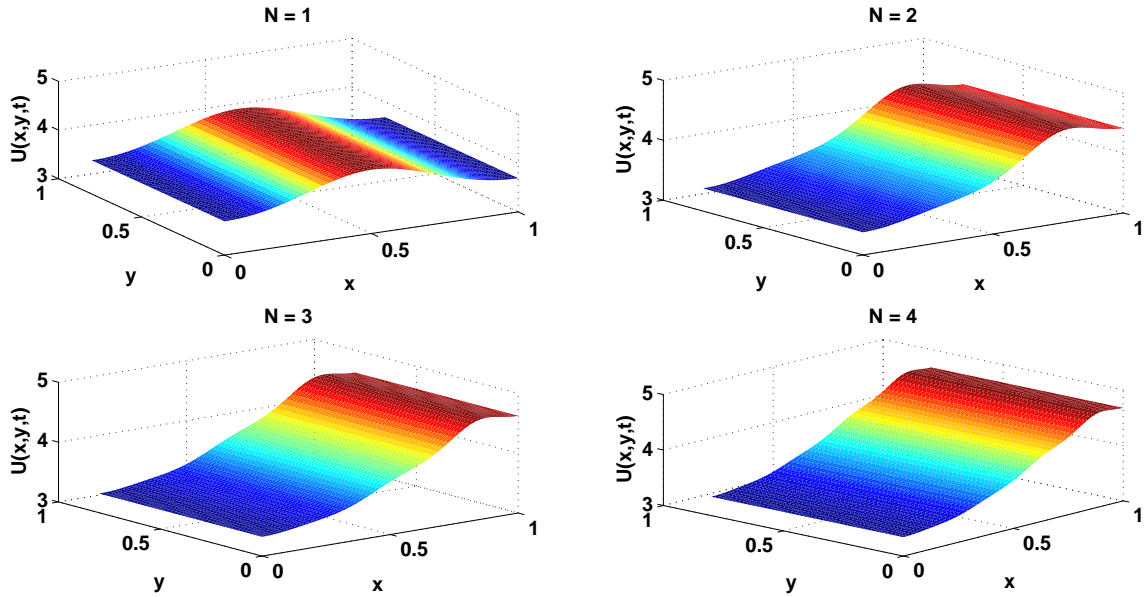


Figure 2.39 $U(x, y, t)$ for $P = 1, D = 1.75$. Initial condition: $U_{0s}(x)$.

Figure 2.39 represents solutions for $P \sim 1$ when symmetric steady states in Figures 2.10 and 2.11 were used as the initial condition. At this value of power, only Λ_{01}^s is unstable on the upper branch for $D = 1.75, N = 2, 3, 4$. The symmetric state evolves to a mirror image of the asymmetric steady states in Figures 2.25 and 2.26. Although the maximum value of the solutions in Figure 2.39 is the same as that in Figures 2.25 and 2.26, the maximum is on the right of $x = \frac{1}{2}$ as opposed to on the left in Figures 2.25 and 2.26. This is purely due to numerical noise. If a small perturbation is added on the left of $x = \frac{1}{2}$ to the initial condition, the initial data would evolve to a stationary state with maximum on the left.

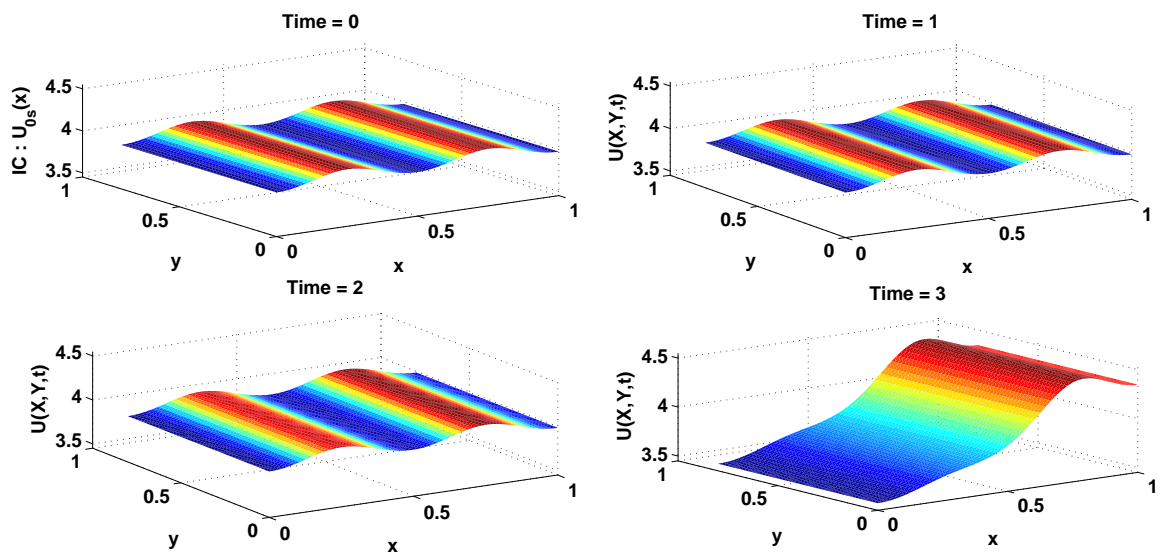


Figure 2.40 $U(x, y, t)$ for $N = 2, P = 1$. Initial condition: $U_{0s}(x)$.

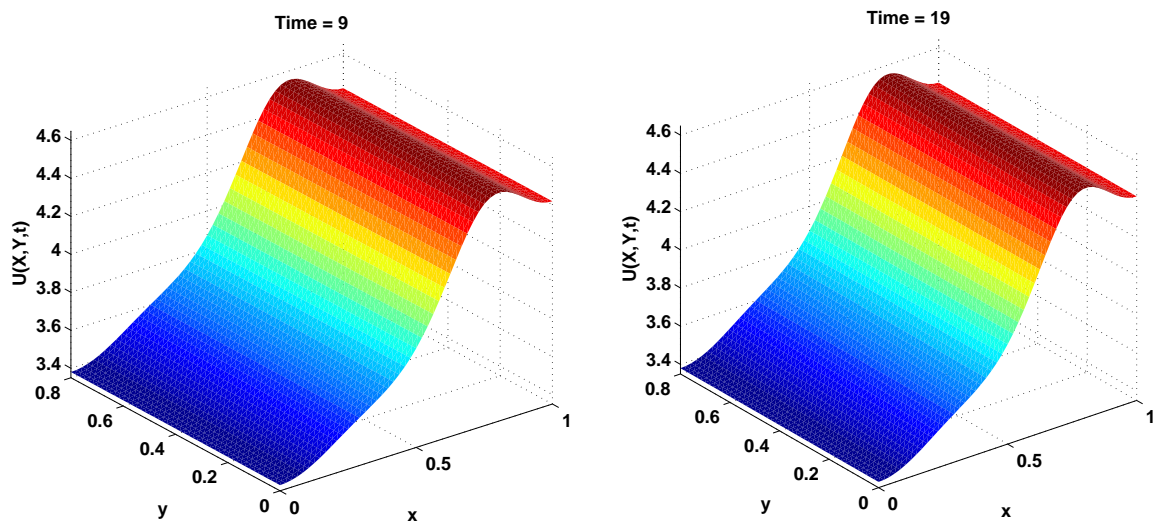


Figure 2.41 $U(x, y, t)$ for $N = 2, P = 1$ at later times.

In Figures 2.40 and 2.41, solutions for $N = 2$ have been plotted at different times as the symmetric steady state (chosen as the initial data) evolves to the asymmetric steady state. When Time=3, initial data have almost reached the asymmetric steady state. Once the solutions reach the asymmetric state, they do not change. This suggests that for the same value of power, the asymmetric steady state is more stable than the symmetric steady state. The same results were observed when $P > 1$, i.e., the symmetric steady state evolved to the asymmetric state.

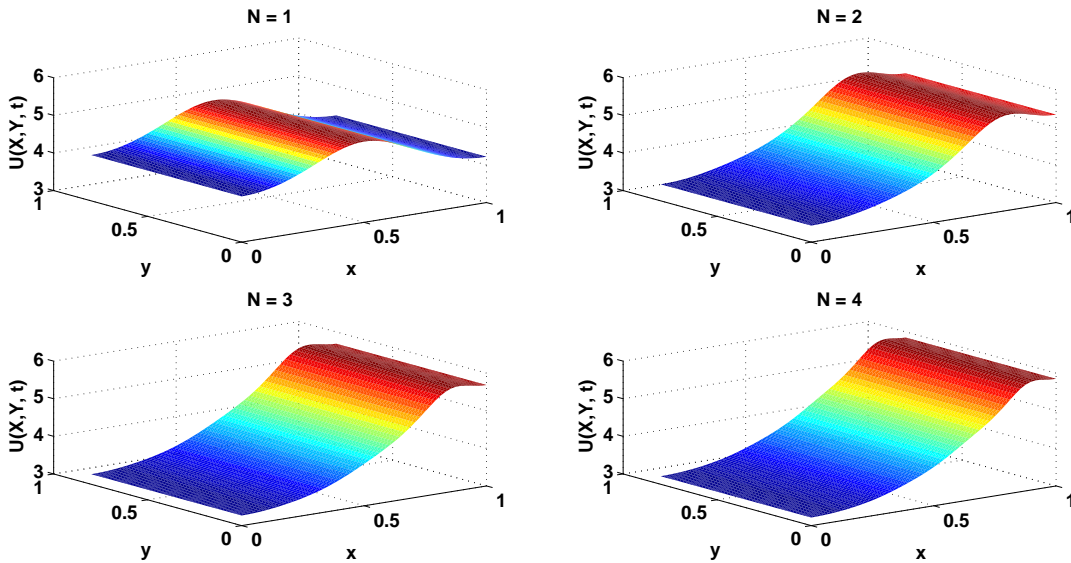


Figure 2.42 $U(x, y, t)$ for $P = 3$. Initial condition: $U_{0s}(x)$.

Even when the power is big enough, there is not enough numerical noise to trigger an instability in the y direction. This has been demonstrated in Figure 2.42 when $P \sim 3$. Although Λ_{10}^s is also unstable for $N = 1, 2, 3, 4$ at the chosen value of power, this mode did not get excited by numerical noise. Instability in solutions was only seen in x -direction due to asymmetric mode λ_1^s getting excited by numerical noise.

Third, an antisymmetric noise $N(y) = \cos(\frac{\pi y}{h})$ in y was introduced into the process when the initial data had evolved to the symmetric steady state. That is, the

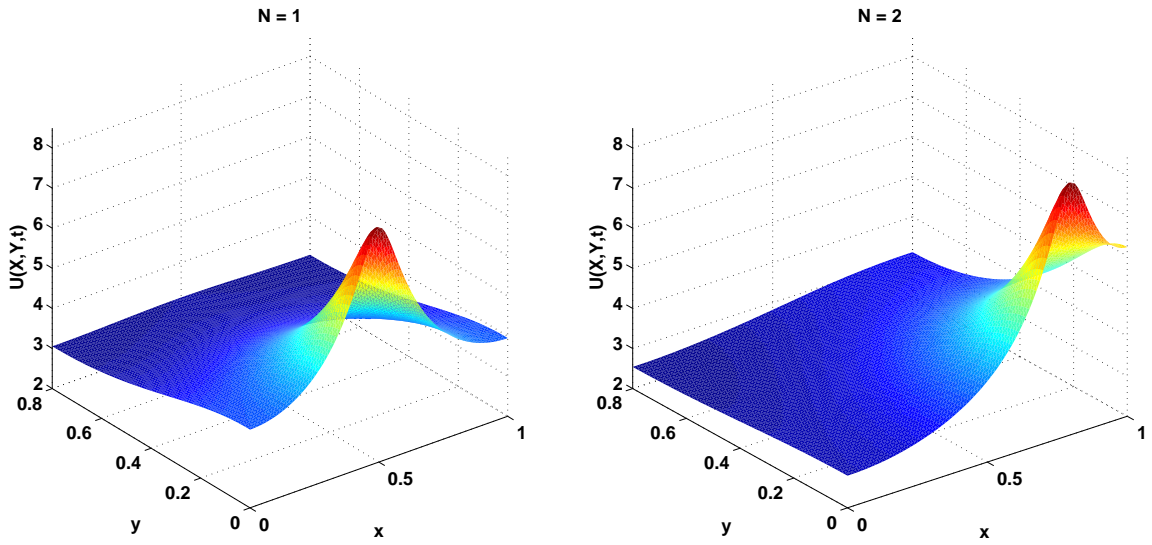


Figure 2.43 $U(x, y, t)$ for $P = 3, N = 1, 2$. Initial condition: $U_{0s}(x) + \epsilon \cos(\frac{\pi y}{h})$.

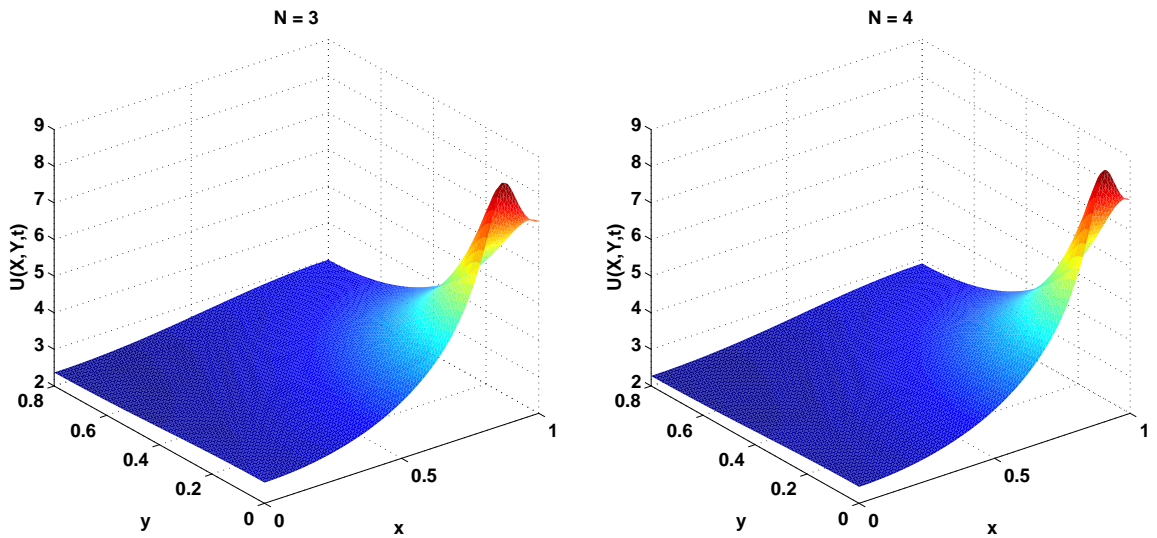


Figure 2.44 $U(x, y, t)$ for $P = 3, N = 3, 4$. Initial condition: $U_{0s}(x) + \epsilon \cos(\frac{\pi y}{h})$.

initial data are now

$$U(x, 0) = U_{0s}(x) + \epsilon N(y), \quad (2.20)$$

where $\epsilon = 0.01$ is the strength of the noise. The mode Λ_{10}^s becomes unstable when $P \sim 1.59$ for $N = 2$. In simulations with $P < 1.59$, solutions evolve either to the symmetric or the asymmetric stationary state. But when $P > 1.59$, a spike was observed at the lower y boundary. The solutions evolved to a spike near $(0.8, 0)$ for $N = 2, 3, 4$ since both Λ_{10}^s and Λ_{10}^a are unstable for these N when $P \sim 3$. These spikes are shown in Figures 2.43 and 2.44 and are formed near the position of maximum temperature of $u_{0a}(x)$. If a small perturbation to the left of $x = \frac{1}{2}$ is added to the initial data, then the spike is formed on the left of $x = \frac{1}{2}$.

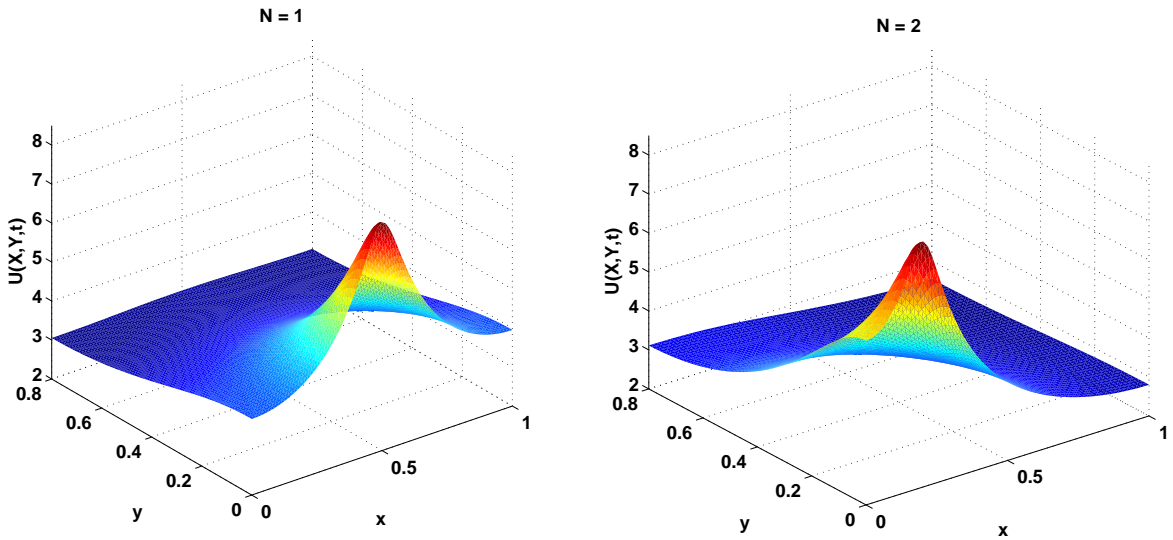


Figure 2.45 $U(x, y, t)$ for $P = 3, N = 1, 2$. Initial condition: $\epsilon \cos(\frac{\pi y}{h})$.

Next, the same noise was added to homogeneous initial data and the solutions for $P \sim 3, N = 1, 2$ were plotted in Figure 2.45. The spike is formed on the lower x boundary for $N = 2$ and the solution is just a mirror image of the solution in Figure 2.43. When $N = 3$ or $N = 4$, the patterns in Figure 2.44 were repeated. This shows that no particular side in x is preferred but numerical noise just causes the initial data

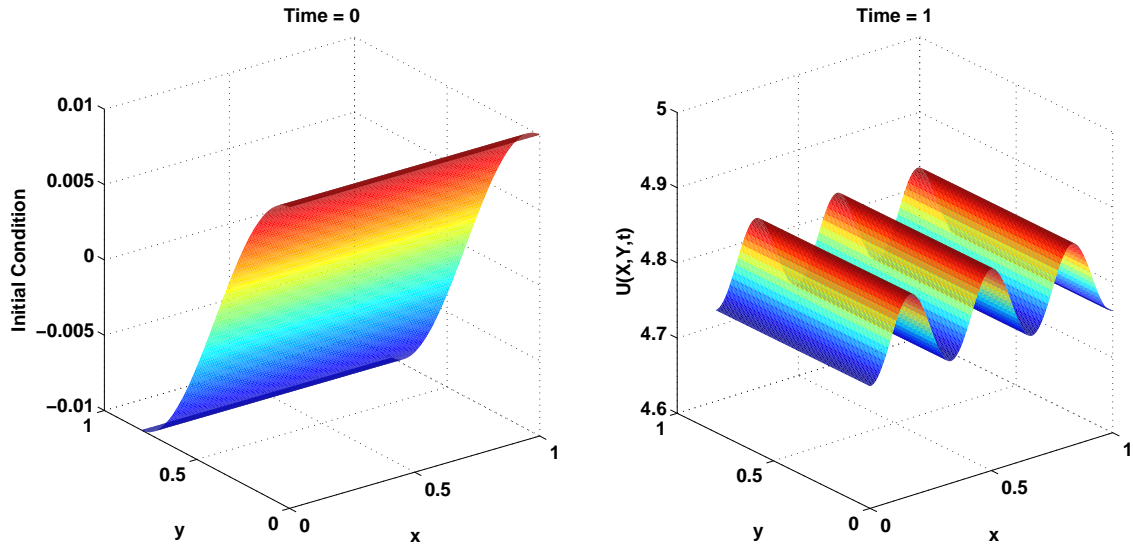


Figure 2.46 $U(x, y, t)$ at $t = 1$ for $N = 3, P \sim 3$. Initial condition: $\epsilon \cos(\frac{\pi y}{h})$.

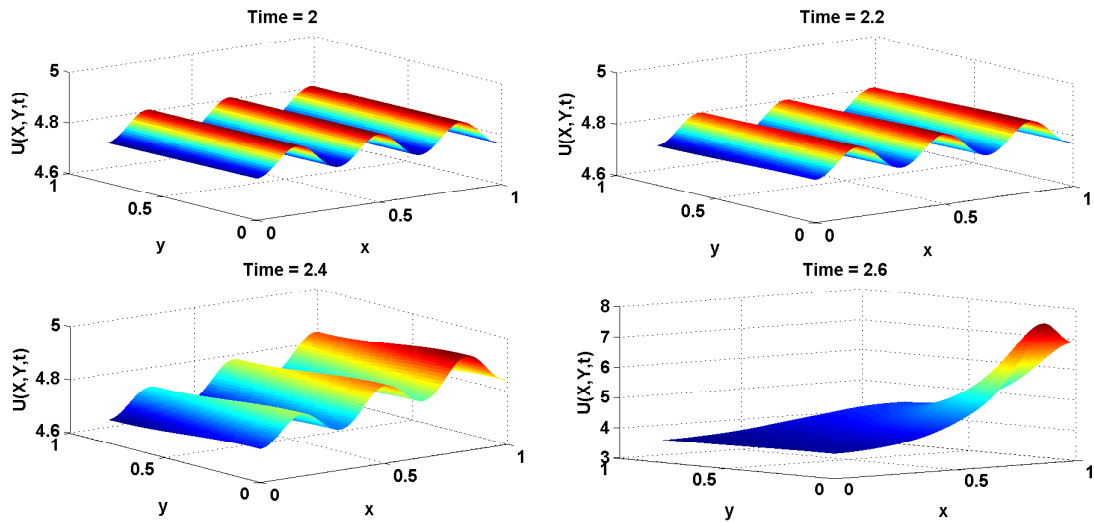


Figure 2.47 $U(x, y, t)$ for $N = 3, P \sim 3$ as it evolves. Initial condition: $\epsilon \cos(\frac{\pi y}{h})$.

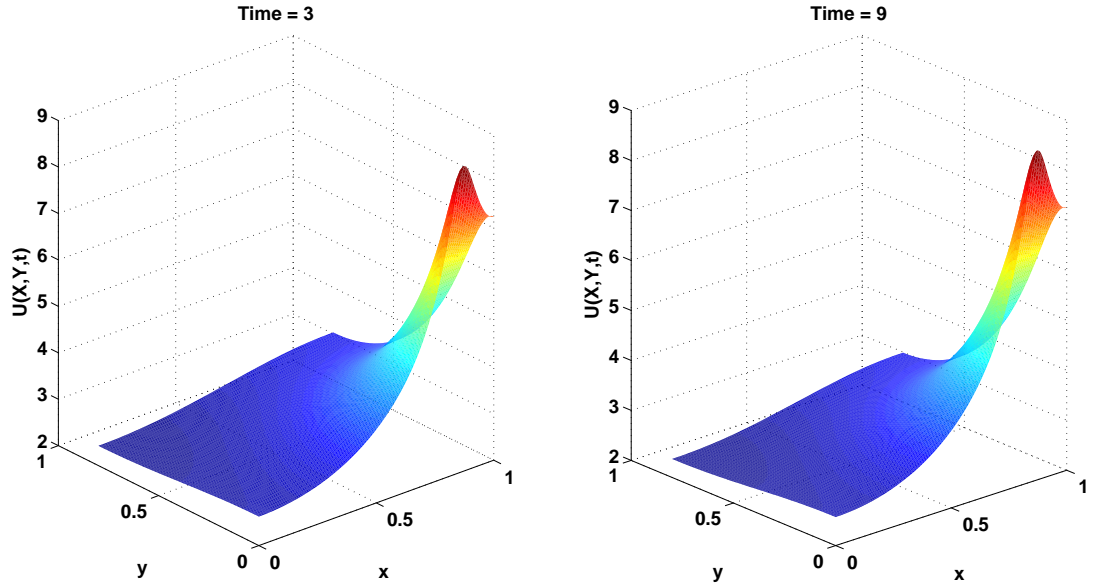


Figure 2.48 $U(x, y, t)$ at later times for $N = 3, P \sim 3$. Initial condition: $\epsilon \cos(\frac{\pi y}{h})$.

to choose one side. The solutions were observed at different times as they evolved to a spike for $N = 3$ and were recorded in Figures 2.46, 2.47 and 2.48. At $Time = 1$, the initial data have already reached the symmetric steady state and stay there for sometime. When $Time \sim 2.2$, instability can be seen due to λ_1^s and Λ_{10}^s becoming unstable and the heat moves to one corner of the slab. The solutions finally evolve to a spike. When $N(y)$ was replaced by $-N(y)$, the spike moved to the other side of the y boundary.

2.5 Conclusions

The heating of a thin ceramic slab in a highly resonant microwave cavity is studied mathematically by accurately approximating numerical solutions of the reaction diffusion equation (2.1a-d). Two different methods yield two different stationary solutions for $N \geq 2$ with different stability properties. The symmetric solution is less stable than the asymmetric solution. The solutions are more uniform and the maximum temperature decreases for a larger modal number N as long as the solutions stay

on the symmetric branch. On the asymmetric branch, maximum temperature and non-uniformity in temperature increase with N . Thus, to obtain uniform heating of the sample, initial data must be chosen so that they evolve to the symmetric branch of the response curve.

If uniform heating is to be achieved, then power should be less than P_b so as to stay on the symmetric branch. For $P > P_b$ it is impossible to obtain uniform heating of the slab since the symmetric solution is unstable. For large values of N , a stable uniform temperature can be obtained if initial data can be chosen so that they evolve to the part of the S-curve corresponding to $P_L < P < P_b$. This is true only for values of D larger than about 1.01. That is, the ceramic slab can be heated uniformly only for certain choices of P and D . A stable flat solution can therefore be obtained when $D > 1, N > 1$ and $P_L < P < P_b$. Also, if D and N are such that $P_c < P_b$, then any initial data with $P_c < P < P_b$ will give a stable uniform solution.

Table 2.3 lists values of power that will provide uniform heating for different values of D and N . For the values of D and N listed in the table, $P_c < P_b$ for all pairs of (N, D) except when $(N, D) = (2, 2.25)$. For this pair, initial data must be chosen to evolve to the part of the S-curve such that $P_L < P < P_b$. The higher the value of D and N , the flatter the solution will be.

Table 2.3 Parameter Values For Uniform Heating For Arbitrary Initial Data

N	$D = 2.25$	2.75	3.25	3.75
2	Restrictions on initial data	$1.12 < P < 1.64$	$1.12 < P < 2.53$	$1.12 < P < 3.81$
3	$1.12 < P < 1.18$	$1.12 < P < 1.87$	$1.12 < P < 2.92$	$1.12 < P < 4.45$
4	$1.12 < P < 1.22$	$1.12 < P < 1.95$	$1.12 < P < 3.05$	$1.12 < P < 4.65$

Higher values of D provide a better range of power values for which stable symmetric stationary solutions can be obtained. For this reason stationary solutions for $D = 2.25$ also will be studied in Chapter 3. The results to be used in next chapter using the methods described in this chapter are plotted below.

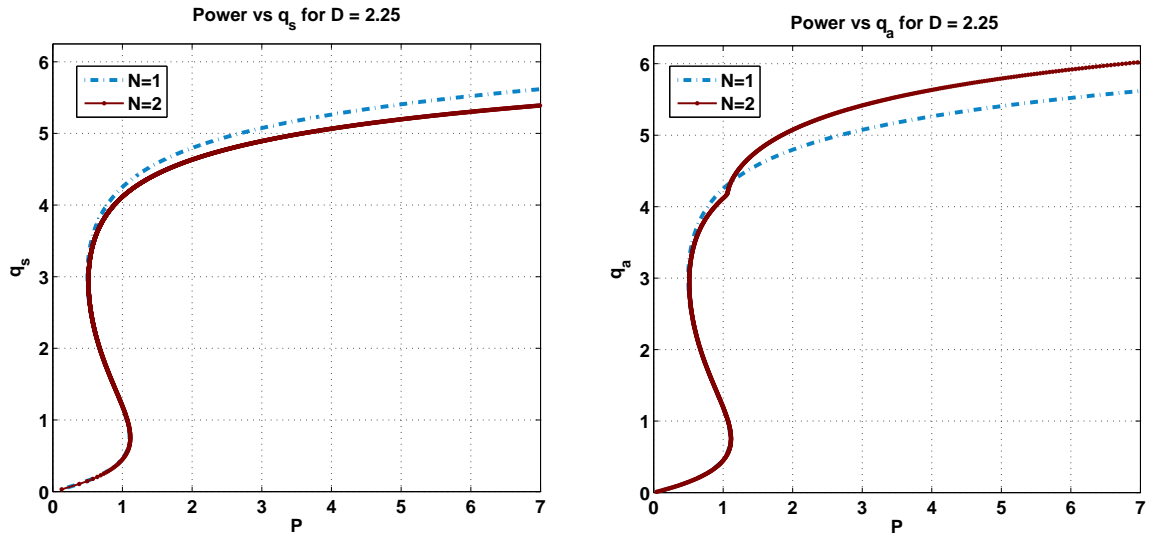


Figure 2.49 S-curves for $D = 2.25$, $N = 1, 2$.

2.6 Future Work

The number of unstable eigen-values increases with N when $N \geq 2$ which suggests the possibility of a rich bifurcation structure to symmetric stationary solutions. This also indicates that the number of asymmetric bifurcations to the symmetric stationary branch also increase with N . The determination of these branches is under further investigation.

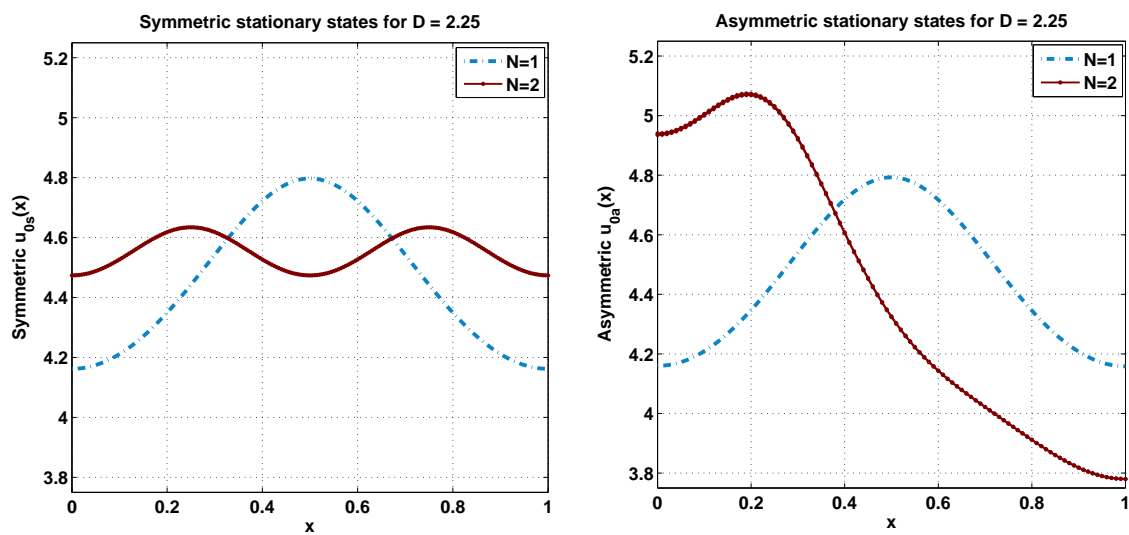


Figure 2.50 Stationary states for $D = 2.25$, $N = 1, 2$.

CHAPTER 3

TWO FUNCTIONAL PROBLEM

3.1 Introduction

This chapter deals with investigating the behavior of solutions for the geometry in Chapter 2 when the mode number N in the electric field source varies as the back wall is moved as a function of time. This was an experiment done by Morris Brodwin [2] with the goal of uniformly heating a sample. In heating applications, a typical microwave source frequency is $f = 2.45 \times 10^3$ Hertz so that the period of wall vibration is $\sim 4 \times 10^{-4}$ seconds. This time scale is very fast as compared to thermal time scales which are \sim seconds or minutes. The fast time scale will be considered here. The dimensionless time is given by $t = t'/\theta_H$ where the thermal time scale θ_H is given by $\theta_H = \rho C_p r h_e$. Here ρ is the density of the ceramic, C_p is its thermal capacity, r is the slab width and h_e is the effective heat transfer coefficient which measures how the slab loses heat to its surroundings by convection. Suppose N takes the form $N(t'/\theta_v)$ or $N(t/\epsilon)$, where $\epsilon = \theta_v/\theta_H \ll 1$ and θ_v is period of wall vibration. Assume t is periodic with period ϵ . This form of N in equation (2.1a) gives

$$\frac{\partial}{\partial t} U = D \nabla_{\perp}^2 U - 2L(U) + \frac{P e^{CU} \sin^2(N(\frac{t}{\epsilon})\pi x)}{[1 + \chi \int_0^1 \int_0^h e^{CU} \sin^2(N(\frac{t}{\epsilon})\pi \tilde{x}) d\tilde{y} d\tilde{x}]^2}, \quad (3.1)$$

Let

$$F\left(x, \frac{t}{\epsilon}\right) = \frac{P e^{CU} \sin^2(N(\frac{t}{\epsilon})\pi x)}{[1 + \chi \int_0^1 \int_0^h e^{CU} \sin^2(N(\frac{t}{\epsilon})\pi \tilde{x}) d\tilde{y} d\tilde{x}]^2}$$

and $U = U^*(x, y, t, \tau)$; $\tau = \frac{t}{\epsilon}$. Then

$$\frac{\partial U}{\partial t} = \frac{\partial U^*}{\partial t} + \frac{1}{\epsilon} \frac{\partial U^*}{\partial \tau}.$$

Inserting this in equation (3.1) gives

$$\frac{\partial U^*}{\partial t} + \frac{1}{\epsilon} \frac{\partial U^*}{\partial \tau} = D\nabla_{\perp}^2 U^* - 2L(U^*) + F(x, \tau)$$

i.e.,

$$U_{\tau}^* = \epsilon \left\{ -U_t^* + D\nabla_{\perp}^2 U^* - 2L(U^*) + F(x, \tau) \right\} \quad (3.2)$$

Expand U^* as

$$U^* \sim U_0^* + \epsilon U_1^* + \epsilon^2 U_2^* + \dots$$

Using the above expansion of U^* in equation (3.2) and equating powers of ϵ yields

$$\begin{aligned} U_{0\tau}^* &= 0 \quad \Rightarrow U_0^* \equiv U_0^*(x, y, t). \\ U_{1\tau}^* &= -U_{0t}^* + D\nabla_{\perp}^2 U_0^* - 2L(U_0^*) + F_1(x, \tau). \end{aligned}$$

where

$$F_1(x, \tau) = \frac{P e^{cU_0^*} \sin^2(N(\tau)\pi x)}{[1 + \chi \int_0^1 \int_0^h e^{cU_0^*} \sin^2(N(\tau)\pi \tilde{x}) d\tilde{y} d\tilde{x}]^2}$$

Integration w.r.t. τ gives

$$U_1^* = c(x, y, t) - \tau U_{0t}^* + D\nabla_{\perp}^2 U_0^* - 2\tau L(U_0^*) + \int_0^{\tau} F_1(x, s) ds,$$

where $c(x, y, t)$ is a constant depending on x, y and t . The author is interested in the behavior of U^* as $\tau \rightarrow \infty$. Since t is periodic, therefore, τ, F and F_1 are periodic with period 1. Let $\tau = n \in \mathbb{Z}^+, n \gg 1$. Then,

$$U_1^* = c(x, y, t) - n \left[U_{0t}^* + D\nabla_{\perp}^2 U_0^* - 2L(U_0^*) + \int_0^1 F_1(x, s) ds \right].$$

For a bounded solution the following must hold:

$$U_{0t}^* + D\nabla_{\perp}^2 U_0^* - 2L(U_0^*) + \int_0^1 F_1(x, s) ds = 0,$$

or

$$U_{0t}^* = D\nabla_{\perp}^2 U_0^* - 2L(U_0^*) + \langle F_1 \rangle(x), \quad (3.3)$$

with $\frac{\partial U_0^*}{\partial n} = 0$ on $\partial\Omega$ and $U_0^* = G$ at $t = 0$. Consider $\langle F_1 \rangle$, i.e.,

$$\begin{aligned} \langle F_1 \rangle &= P e^{CU_0^*} \int_0^1 \frac{\sin^2(N(s)\pi x) ds}{[1 + \chi \int_0^1 \int_0^h e^{CU_0^*} \sin^2(N(s)\pi \tilde{x}) d\tilde{y} d\tilde{x}]^2} \\ &= P e^{CU_0^*} \Delta s \sum_{k=1}^p \frac{\sin^2(N_k \pi x)}{[1 + \chi \int_0^1 \int_0^h e^{CU_0^*} \sin^2(N_k \pi \tilde{x}) d\tilde{y} d\tilde{x}]^2} \\ &= P e^{CU_0^*} \sum_{k=1}^p \frac{a_k \sin^2(N_k \pi x)}{[1 + \chi \int_0^1 \int_0^h e^{CU_0^*} \sin^2(N_k \pi \tilde{x}) d\tilde{y} d\tilde{x}]^2}, \end{aligned} \quad (3.4)$$

where p is the number of subintervals, each Δs wide such that $N = k$, $a_k = \frac{\Delta s}{p}$ and therefore, $\sum_{k=1}^p a_k = 1$. The example where N switches between 1 and 2 in one

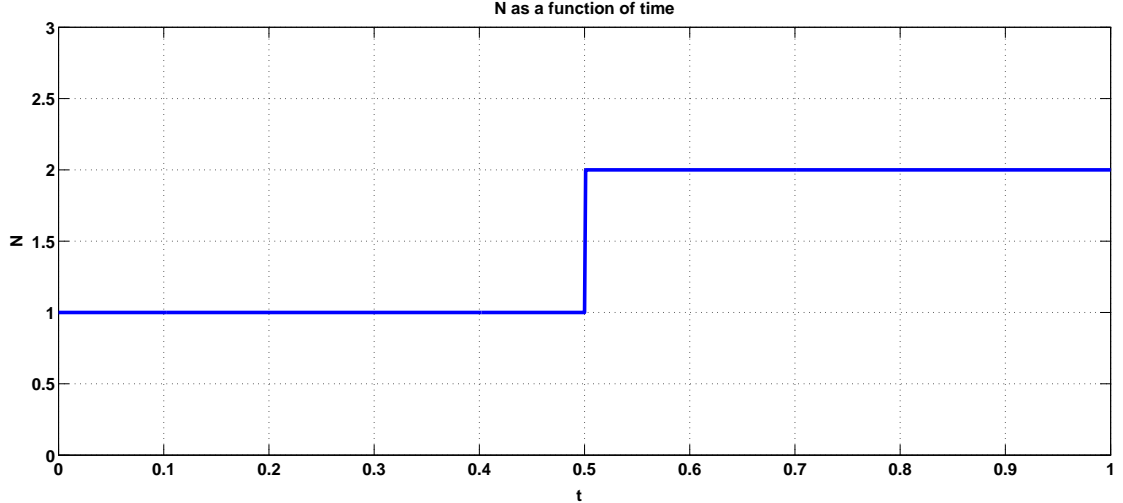


Figure 3.1 N as a periodic function of time in one period of t .

period of t as shown in Figure 3.1, is studied here. From equations (3.3) and (3.4), U_0^* satisfies

$$U_{0t}^* = D\nabla_{\perp}^2 U_0^* - 2L(U_0^*) + P e^{CU_0^*} [a_1 g_1 \sin^2(\pi x) + a_2 g_2 \sin^2(2\pi x)], \quad (3.5)$$

where

$$g_1 = \frac{1}{[1 + \chi \int_0^1 \int_0^h e^{CU_0^*} \sin^2(\pi \tilde{x}) d\tilde{y} d\tilde{x}]^2}, \quad (3.6a)$$

$$g_2 = \frac{1}{[1 + \chi \int_0^1 \int_0^h e^{CU_0^*} \sin^2(2\pi \tilde{x}) d\tilde{y} d\tilde{x}]^2}. \quad (3.6b)$$

For steady states, $\partial_t = 0$. Also, $\partial_y = 0$ for solutions independent of y .

$$DU_{0xx}^* - 2L(U_0^*) + Pe^{CU_0^*} [a_1 g_1 \sin^2(\pi x) + (1 - a_1) g_2 \sin^2(2\pi x)], \quad 0 < x < 1, \quad (3.7)$$

where g_1 and g_2 are functionals, as defined above. Using $U_{0x}^* = 0, x = 0, 1$ a "new" shooting method must be developed for this problem involving two functionals, and other more complicated problems.

3.2 Stationary Solutions

Since the solutions of equation (3.7) are independent of y , they are denoted by $u_0(x)$, i.e., $U_0^*(x) = u_0(x)$. These solutions provide a stationary solution for the two-dimensional steady state version of equation (3.5). As in the one functional case, equation (3.7) admits both symmetric ($u_{0s}(x)$) and asymmetric ($u_{0a}(x)$) stationary solutions. Physically, these solutions represent a symmetric or an asymmetric stripe pattern about $x = \frac{1}{2}$. It would be interesting to determine these stripes and how they evolve in time since they represent local maxima of temperature distribution along the slab. The number, location and temperature of symmetric stripes depends on the choice of N_1, N_2, a_1, a_2 . If $a_1 > a_2$, then N_1 number of stripes will be seen in the stationary solution. For the purposes of this dissertation, N_1 and N_2 have been fixed to be 1 and 2 respectively. Other pairs can be similarly dealt with. The solutions will be studied for $a_1 = 0.2, 0.5, 0.8$ and $D = 0.75, 1.25, 1.75, 2.25$. Other parameters $\beta = \chi = 0.01$ and $C = 1.5$ are fixed unless otherwise stated. The uniformity of temperature distribution along the slab and stability of these solutions will be

compared with solutions obtained in Chapter 2. A very clever application of Newton's method in the shooting method accurately approximates the stationary solutions to the problem. As in the previous chapter, the symmetric stationary solutions are found first.

3.2.1 A Symmetric Stationary Solution

The source used in the present problem is a combination of two symmetric sources about $x = \frac{1}{2}$, hence, stationary solutions with the same symmetry are desired. Consider the related initial value problem when N switches between $N_1 = 1$ and $N_2 = 2$:

$$D\psi_{xx} - 2L(\psi) + e^{C\psi} \sum_{i=1}^2 \Gamma_i S_i(x) = 0, \quad 0 < x < 1, \quad (3.8a)$$

$$S_i(x) = \sin^2(N_i \pi x), \quad \Gamma_i = a_i P_i g_i, \quad i = 1, 2, \quad (3.8b)$$

$$\psi(0) = \alpha, \quad (3.8c)$$

$$\psi_x(0) = 0, \quad (3.8d)$$

where a_i are as in equation (3.4), g_i are defined in equations (3.6a,b), P_1, P_2 are positive constants and N_1, N_2 are positive integers. The above initial value problem is solved using a fourth order Runge-Kutta scheme for a fixed α, Γ_1 and Γ_2 . In the physical space, a solution to equations (3.8a-d) satisfies equation (3.7) if

$$\psi_x(1) = 0, \quad (3.9a)$$

$$\|\psi\|_2^2 - \zeta = 0, \quad (3.9b)$$

$$P_1 = P_2. \quad (3.9c)$$

From (3.8b), equation (3.9c) is equivalent to $a_2g_2\Gamma_1 - a_1g_1\Gamma_2 = 0$. Define the functions

$$F(\Gamma_1; \Gamma_2; \alpha; \zeta) = \psi_x(1), \quad (3.10a)$$

$$G(\Gamma_1; \Gamma_2; \alpha; \zeta) = \|\psi\|_2^2 - \zeta, \quad (3.10b)$$

$$H(\Gamma_1; \Gamma_2; \alpha; \zeta) = a_2g_2\Gamma_1 - a_1g_1\Gamma_2. \quad (3.10c)$$

If for a fixed ζ , the three parameters Γ_1, Γ_2 and α can be found such that $F = G = H = 0$, then equations (3.8a-d) will be satisfied. This is done by fixing ζ and using a 3-dimensional Newton's method to find Γ_1, Γ_2 and α . A continuation procedure on ζ is used to obtain the starting values Γ_1^0, Γ_2^0 and α^0 . Choose $\zeta_0 \ll 1$ so that equation (3.7) can be linearized and solved to give:

$$\Gamma_2^0 = \frac{4\sqrt{2\zeta^0}}{\sqrt{\left(\frac{1+A}{2\rho}\right)^2 + \left(\frac{A}{\varrho_1}\right)^2 + \frac{1}{\varrho_2^2}}}, \quad (3.11a)$$

$$\Gamma_1^0 = A\Gamma_2^0, \quad (3.11b)$$

$$\alpha^0 = \frac{\Gamma_2^0}{4} \left(\frac{1+A}{\rho} - \frac{A}{\varrho_1} - \frac{1}{\varrho_2} \right). \quad (3.11c)$$

where $A = \frac{a_1}{a_2}$, $\rho = L'(0)$, $\varrho_i = \rho + 2DN_i^2\pi^2$, $i = 1, 2$. These values of Γ_1, Γ_2 and α are used as the initial guesses in Newton's method. Once $\Gamma_1(\zeta_0), \Gamma_2(\zeta_0)$ and $\alpha(\zeta_0)$ are obtained, a slightly larger value of ζ , say $\zeta_1 > \zeta_0$, is chosen and $\Gamma_1(\zeta_0), \Gamma_2(\zeta_0), \alpha(\zeta_0)$ are used respectively as initial guesses for $\Gamma_1(\zeta_1), \Gamma_2(\zeta_1)$ and $\alpha(\zeta_1)$. This process is continued and yields the functions $\Gamma_1(\zeta), \Gamma_2(\zeta)$ and $\alpha(\zeta)$. Each ζ yields a stationary solution on $[0, 1]$. Let

$$q_s = \max_{x \in [0, 1]} \psi(x), \quad (3.12)$$

where the subscript s stands for symmetric. It can be shown graphically that there is a 1-1 correspondence between ζ and q_s . Since the interest is to study how different parameters affect the maximum temperature of the slab, therefore, q_s is used for plotting. The solution of equations (3.8a-d) and (3.9a-c) will completely satisfy

equation (3.7) when

$$\begin{aligned} P &= \frac{\Gamma_1(q_s)}{a_1} \left[1 + \frac{\chi}{h} \int_0^h \int_0^1 \sin^2(N_1 \pi x) e^{C\psi} dx dy \right]^2 \\ &= \frac{\Gamma_2(q_s)}{a_2} \left[1 + \frac{\chi}{h} \int_0^h \int_0^1 \sin^2(N_2 \pi x) e^{C\psi} dx dy \right]^2. \end{aligned} \quad (3.13)$$

Equation (3.13) implicitly gives the maximum temperature along the surface of the slab as a function of power P .

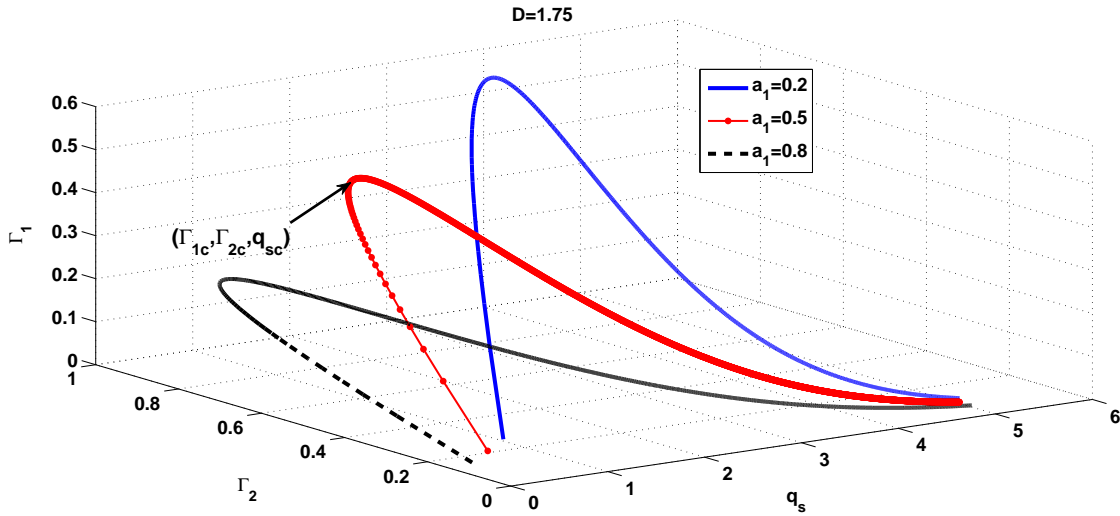


Figure 3.2 Γ_1 as a function of Γ_2 and q_s , $D = 1.75$.

Γ_1 is a multi-valued function of q_s and Γ_2 and traces a curve in the $(q_s, \Gamma_2, \Gamma_1)$ plane. In Figure 3.2, Γ_1 has been plotted as a function of Γ_2 and q_s for $D = 1.75$ and $a_1 = 0.2, 0.5, 0.8$. There are two solutions for $\Gamma_1 < \Gamma_{1c}$ and no solution for $\Gamma_1 > \Gamma_{1c}$. Γ_{1c} is bigger for a smaller value of a_1 .

Figures 3.3 and 3.4 represent q_s as a function of power for same three values of a_1 and $D = 0.75, 1.25, 1.75, 2.25$. The different values of D are obtained for a fixed d , the slab thickness, by varying h_e , the effective heat transfer coefficient. Maximum temperature increases as D decreases, i.e., as h_e decreases. In Chapter 2 it was observed that for the same value of power, maximum temperature is more for a smaller

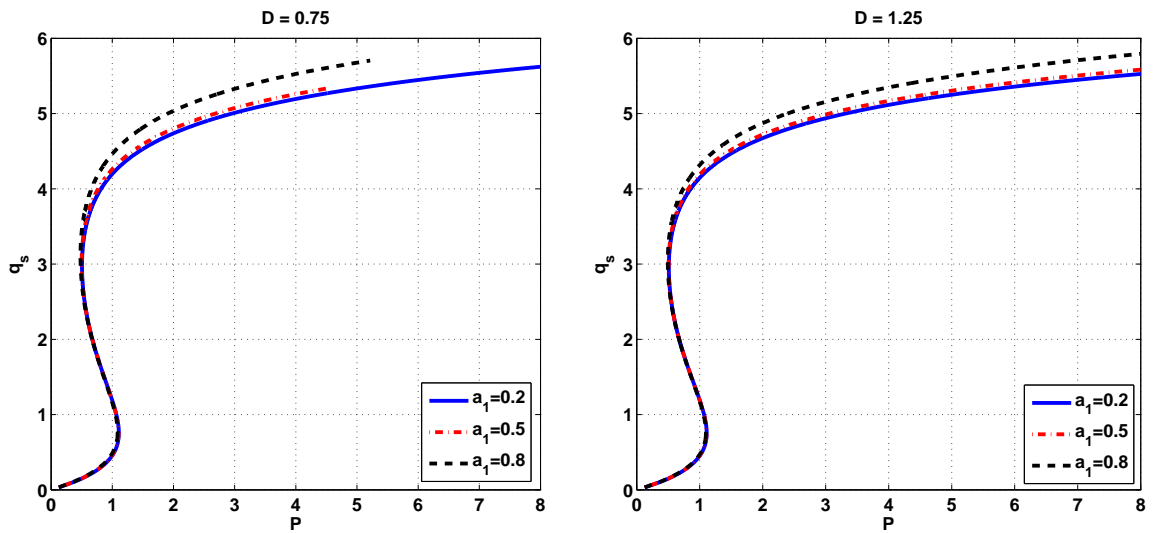


Figure 3.3 Maximum temperature as a function of power for $D = 0.75, 1.25$.

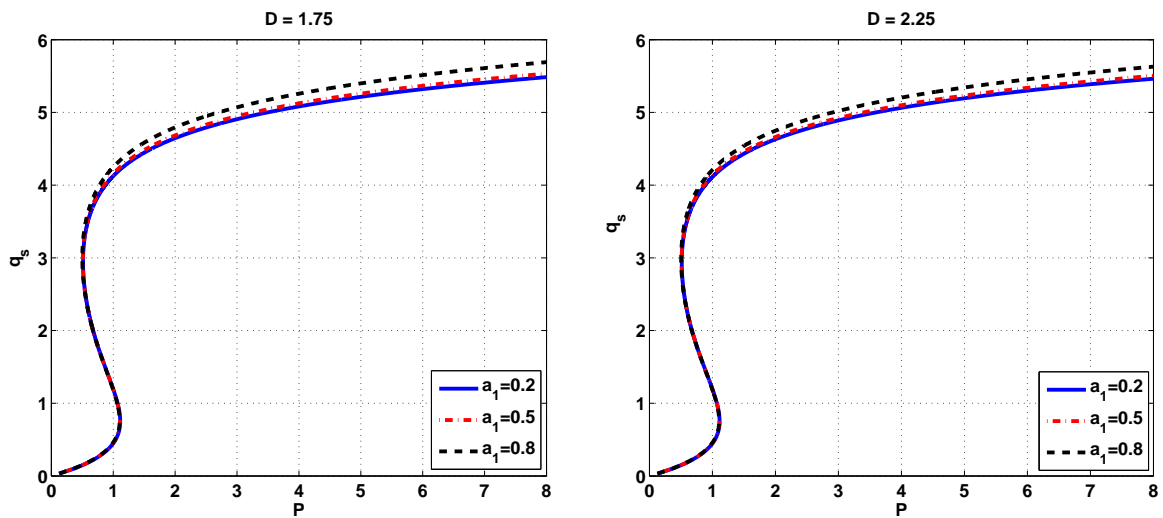


Figure 3.4 Maximum temperature as a function of power for $D = 1.75, 2, 2.5$.

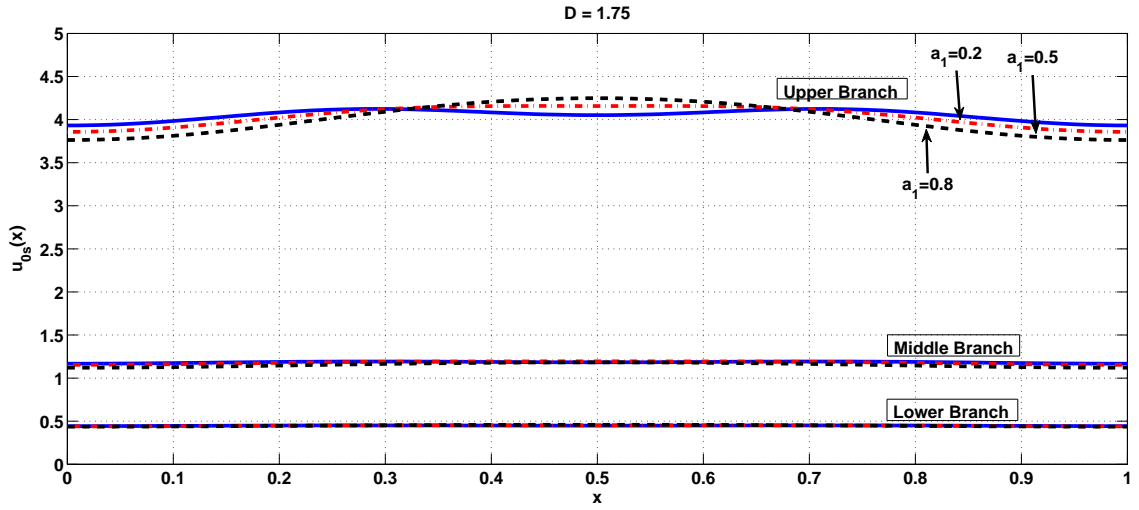


Figure 3.5 Stationary solution as a function of x , $P \sim 1$, $D = 1.75$.

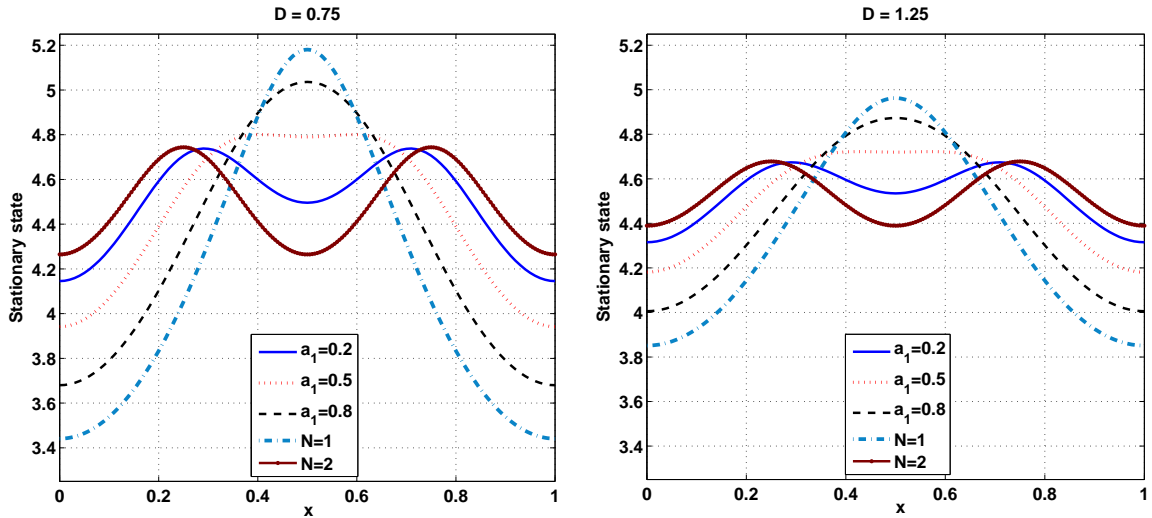


Figure 3.6 Comparison of symmetric states obtained from using one source with those that use a time-varying source when $P \sim 2$.

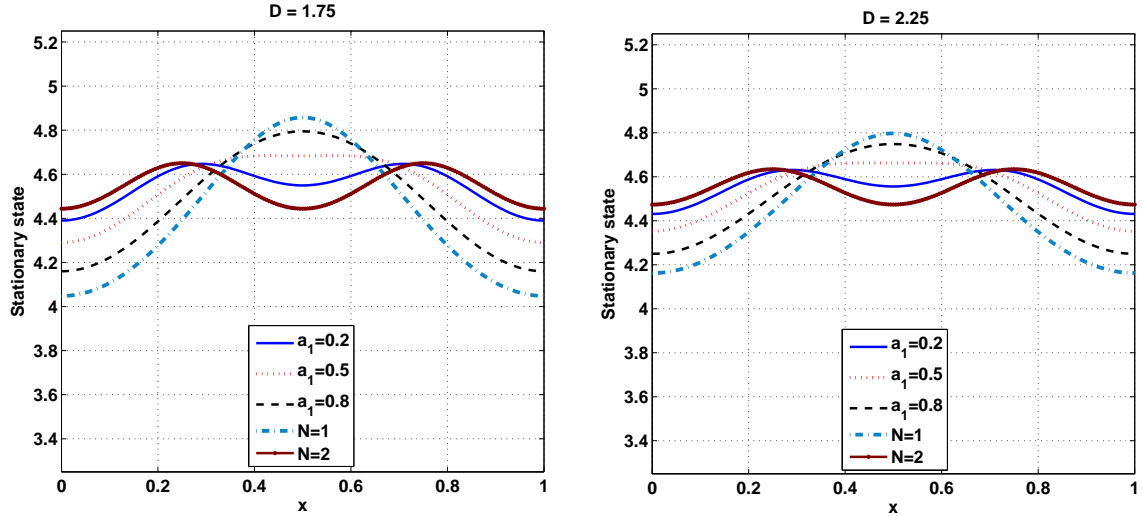


Figure 3.7 Comparison of symmetric states obtained from using one source with those that use a time-varying source when $P \sim 2$.

value of N . Since a_1 represents the weight given to $N_1 = 1$, therefore, maximum temperature increases and upper branches move higher with a_1 .

Next, stationary solutions in the upper, middle and lower branches have been depicted in Figure 3.5 for $P \sim 1$ and $D = 1.75$. As a_1 decreases, a_2 increases and so does the contribution of the source term with a larger modal number. Therefore, maximum temperature decreases and the temperature along the slab becomes more uniform.

Figures 3.6 and 3.7 compare symmetric stationary solutions for $N = 1$ and $N = 2$ from the one functional problem with those for $N_1 = 1, N_2 = 2, a_1 = 0.2, 0.5, 0.8$ for the two functional problem for different values of D . The maximum temperature is highest for the solution corresponding to $N = 1$ and this is also the most non-uniform solution. Although the solution for $N = 2$ is more uniform than the one for $N = 1$, the temperature variations are even lesser for the solution when $a_1 = 0.2$. Thus, the most uniform solution is the one corresponding to $a_1 = 0.2$. As the component of $N_1 = 1$ increases, the variations in temperature along the slab also increase.

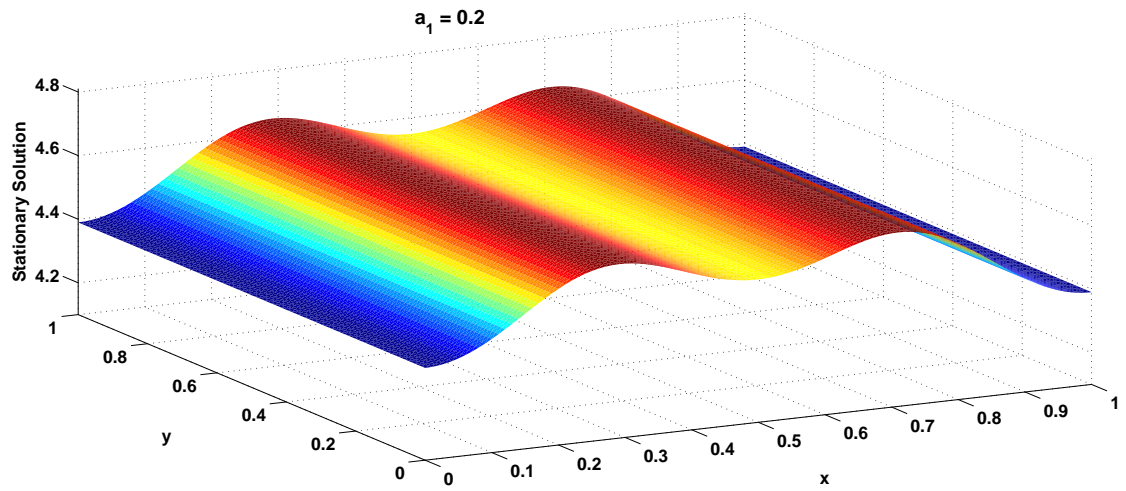


Figure 3.8 $U_{0s}^*(x)$, $a_1 = 0.2$, $P \sim 2$, $D = 1.75$.

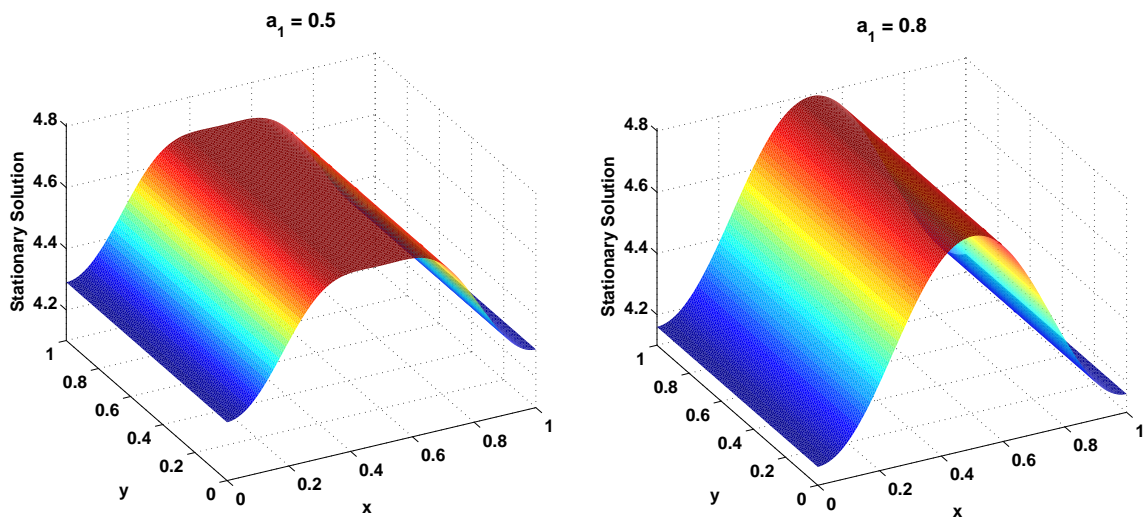


Figure 3.9 $U_{0s}^*(x)$, $a_1 = 0.5, 0.8$, $P \sim 2$, $D = 1.75$.

The symmetric stripe $U_{0s}^*(x)$ has been shown in Figures 3.8 and 3.9 for $P \sim 2, D = 1.75$. Uniformity in temperature distribution increases with a_2 , the weight of the source term with $N_2 = 2$. Two stripes are seen when $a_1 = 0.2$. Clearly, this solution is more uniform than those for $a_1 = 0.5, 0.8$. For $a_1 = 0.5$, there is a whole region where the temperature is almost constant but the temperature drops dramatically at the sides of the slab.

3.2.2 An Asymmetric Stationary Solution

It has already been observed in Chapter 2 that when an electric field source term with modal number $N > 1$ is excited at the aperture of a microwave cavity to heat a ceramic slab, then the temperature distribution along the slab admits both asymmetric and symmetric stationary states. For the same value of power, the asymmetric stationary solution was found to be more stable than the symmetric state. Since two source terms are involved in the current problem, one will be with $N > 1$ and therefore, this system also will yield asymmetric stationary states along with symmetric ones.

The asymmetric branch is found using α as the control parameter, similar to the method of finding the asymmetric branch for the one functional problem, instead of the L_2 norm to proceed along the S-shaped curve. The initial value problem (3.8) is solved using a fourth order Runge-Kutta method for a fixed α, Γ_1 and Γ_2 . For the solution of this initial value problem to be a candidate for equation (3.7), equations (3.9a) and (3.9c) must be satisfied. Define the functions

$$F_a(\Gamma_1; \Gamma_2; \alpha;) = \psi_x(1), \quad (3.14a)$$

$$G_a(\Gamma_1; \Gamma_2; \alpha;) = a_2 g_2 \Gamma_1 - a_1 g_1 \Gamma_2. \quad (3.14b)$$

If for a fixed α, Γ_1 and Γ_2 can be found such that $F_a = G_a = 0$, then equations (3.8a-d) will be satisfied. This is done by fixing α and using a 2-dimensional Newton's

method to find Γ_1 and Γ_2 . A continuation procedure on α is then used to obtain $\Gamma_1(\alpha)$ and $\Gamma_2(\alpha)$ as functions of α .

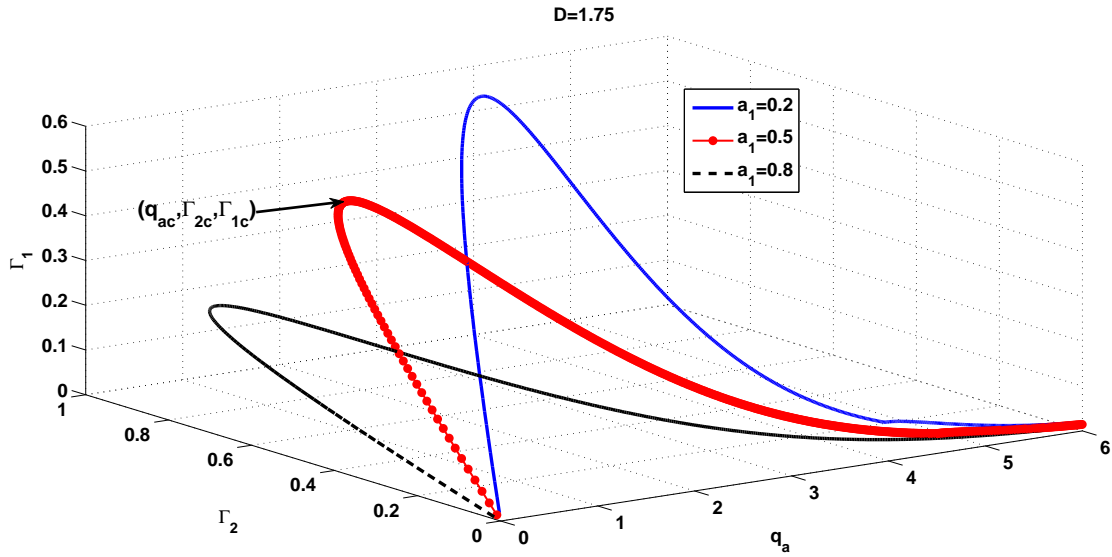


Figure 3.10 Γ_1 as a function of Γ_2 and q_a , $D = 1.75$.

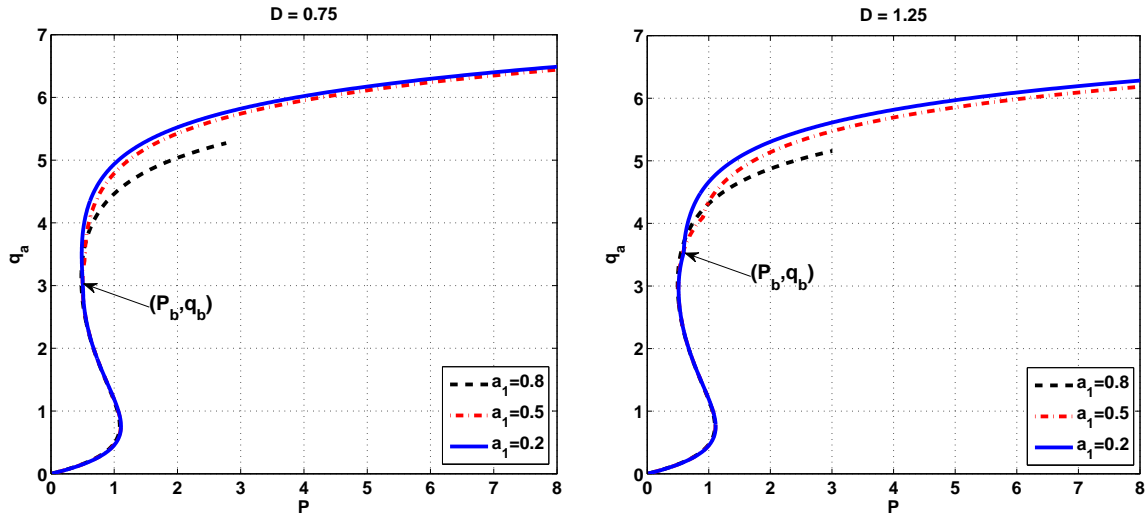


Figure 3.11 P vs q_a for $D = 0.75, 1.25$ and $a_1 = 0.2, 0.5, 0.8$.

Let q_a be the maximum temperature for the asymmetric stationary solution. Again, since it is desired to study different parameters as a function of maximum temperature, q_a instead of α is used for plotting results. Figure 3.10 is a plot of Γ_1

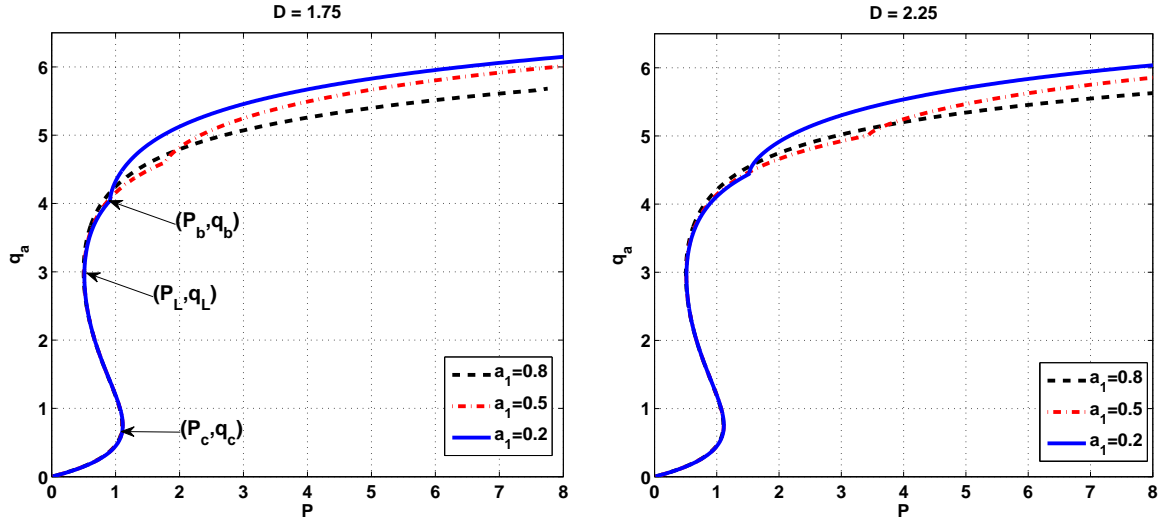


Figure 3.12 P vs q_a for $D = 1.75, 2.25$ and $a_1 = 0.2, 0.5, 0.8$.

as a multi-valued function of q_a and Γ_2 for $D = 1.75$. There are two solutions for $(\Gamma_1, \Gamma_2) < (\Gamma_{1c}, \Gamma_{2c})$ and no solution for $(\Gamma_1, \Gamma_2) > (\Gamma_{1c}, \Gamma_{2c})$.

Maximum temperature q_a as function of power is an S-shaped curve as depicted in Figures 3.11 and 3.12 for four different values of D . Maximum temperature increases on moving up along the curve. At a special point (P_b, q_b) on the S-curve, another asymmetric bifurcation branch emerges in addition to the symmetric branch studied in the previous section. As a_1 increases, the bifurcation point moves up along the S-curve and the asymmetric solutions tend to move closer to the symmetric branch. A higher diffusion coefficient smoothes the solutions and hence they move even closer to the symmetric branch.

Next, stationary solutions in the upper, middle and lower branches have been plotted in Figure 3.13 for $P \sim 1$ and $D = 1.75$. The lower and middle branch solutions are almost constant. At the upper branch, solution for $a_1 = 0.2$ only is on the asymmetric branch for this value of power, the rest are still on the symmetric branch. For this reason, the solution for $a_1 = 0.5$ is most uniform in this case.

Figures 3.14 and 3.15 compare asymmetric solutions from one functional problem with those for the two functional problem for $P \sim 2$. The solution corresponding to

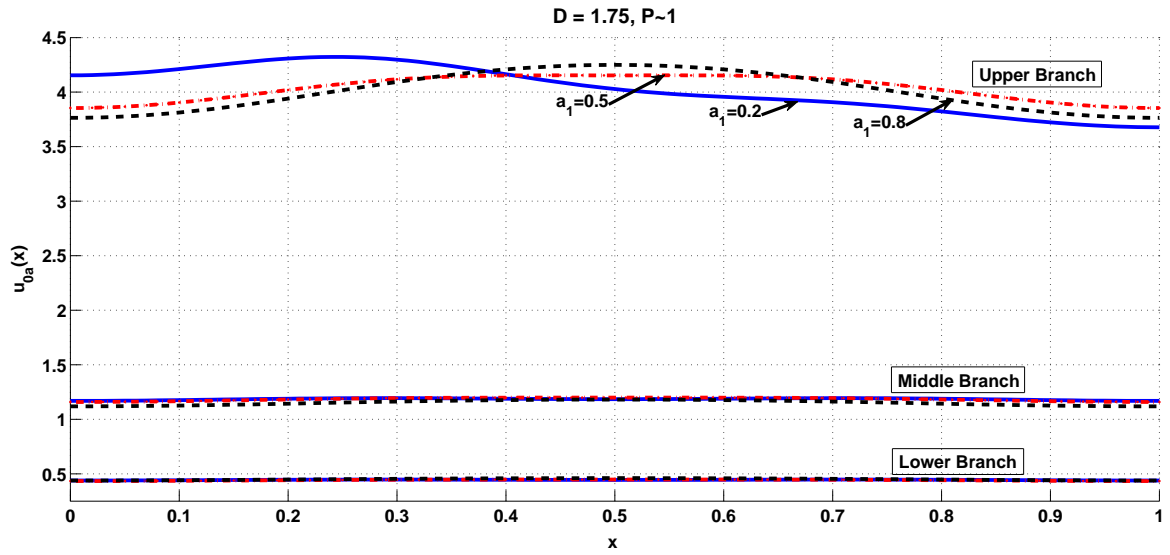


Figure 3.13 $u_{0a}(x)$ for $P \sim 1$, $D = 1.75$ and $a_1 = 0.2, 0.5, 0.8$.

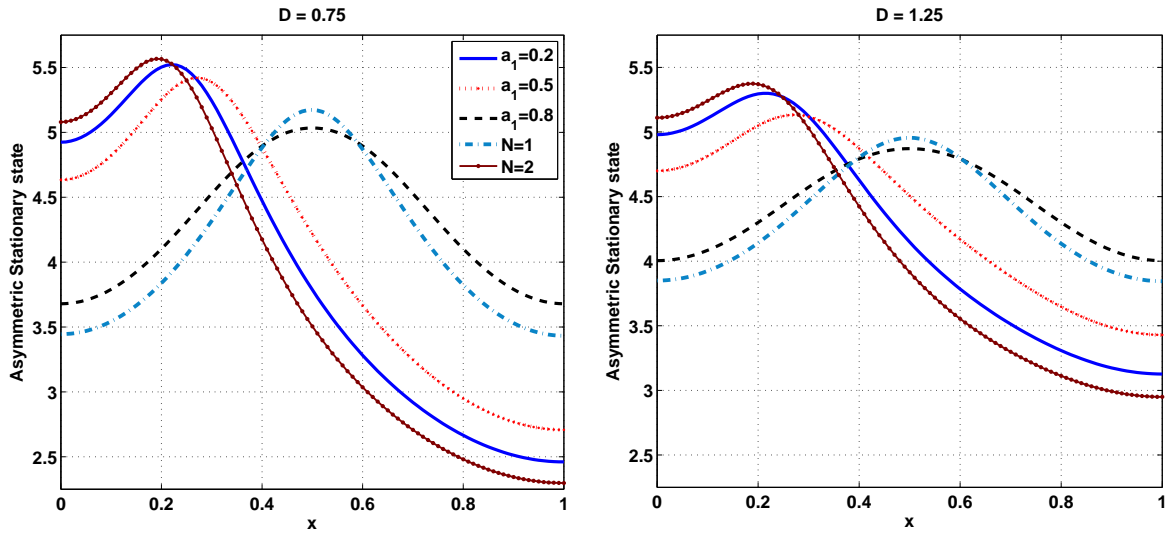


Figure 3.14 Asymmetric states obtained from using one source vs those that use two sources for $P \sim 2$, $D = 0.75, 1.25$.

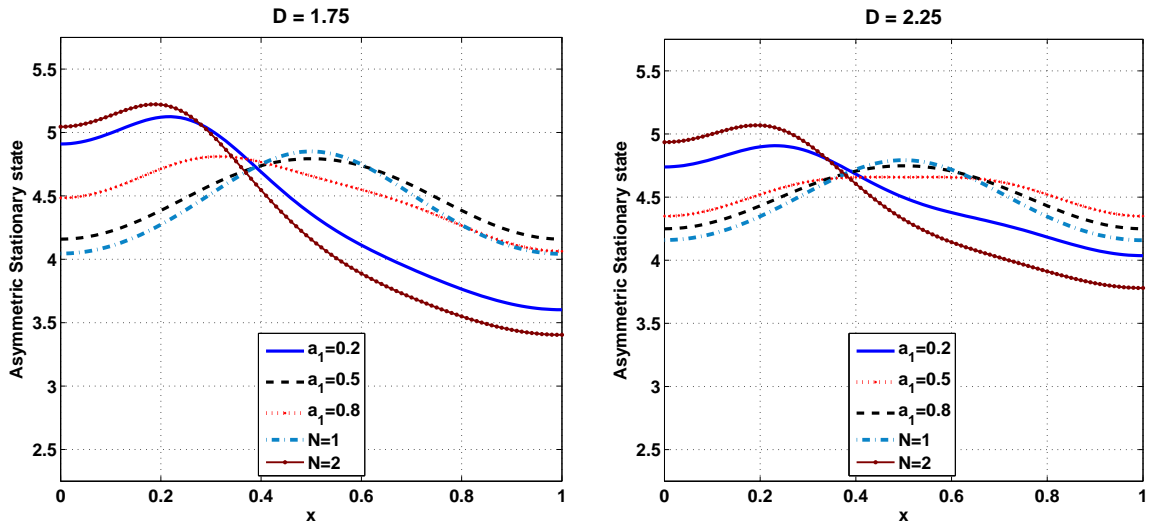


Figure 3.15 Asymmetric states obtained from using one source vs those that use two sources for $P \sim 2$, $D = 1.75, 2.25$.

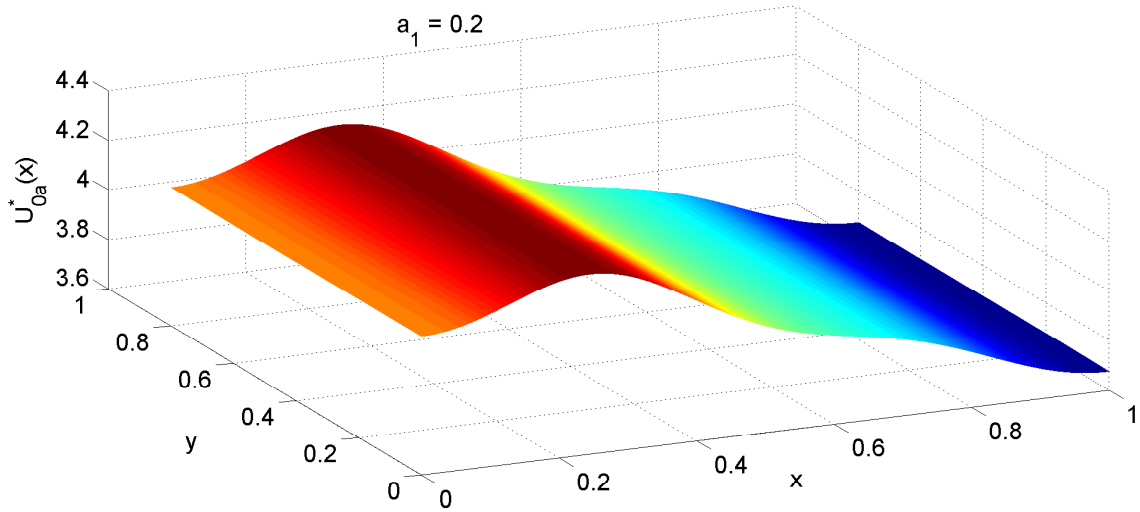


Figure 3.16 $U_{0a}^*(x)$, $a_1 = 0.2$, $P \sim 1$, $D = 1.75$.

$a_1 = 0.8$ is still on the symmetric branch and is more uniform compared to the solution for $N = 1$. On the asymmetric branch, the solutions corresponding to $a_1 = 0.5$ are more uniform than those for $a_1 = 0.2$ or $N = 2$. This shows that uniformity increases with a_1 . This is because on the asymmetric branch, asymmetry increases with N and a bigger value of a_1 corresponds to greater weight of $N_1 = 1$ which adds symmetry to the solution.

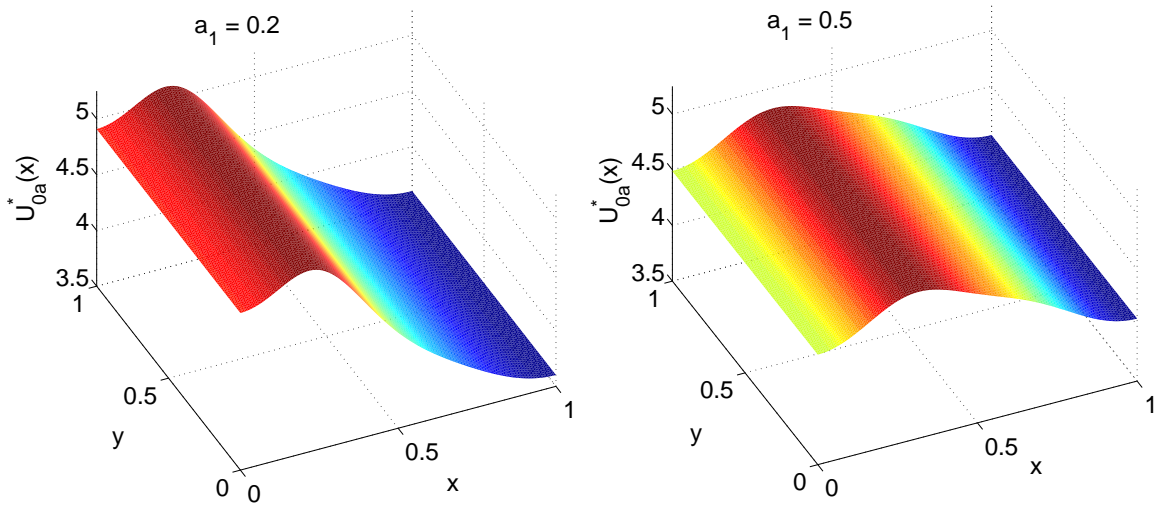


Figure 3.17 $U_{0a}^*(x)$, $P \sim 2$, $D = 1.75$.

The stationary solutions as a function of x and y represent distribution of stationary temperature along the surface of the ceramic slab. When $P \sim 1$, the stationary solutions for $a_1 = 0.2$ only have moved to the asymmetric branch. This asymmetric striped solution has been presented in Figure 3.16. The solutions for $a_1 = 0.5$ and $a_1 = 0.8$ are on the symmetric branch and therefore, the temperature is more uniform for these values of a_1 . When the power applied by the source is increased to $P \sim 2$, then the solution for $a_1 = 0.5$ also moves to the asymmetric branch. This shows that as a_1 increases, a bifurcation occurs for a higher value of P .

Figure 3.17 depicts asymmetric stripes for $a_1 = 0.2, 0.5$. The uniformity of the asymmetric striped solution increases with a_1 . The behaviour of asymmetric states moves closer to that of symmetric states as a_1 increases. The stationary states for

$a_1 = 0.8$ move to the asymmetric branch when the power is as high as $P \sim 7.71$. Even at this value of power, the solution is very close to the symmetric state. This suggests that for high values of power, solutions from higher values of a_1 provide better uniformity in heating. In Figures 3.18 and 3.19 the asymmetric solutions as a function of x and as function of x and y have been shown for same three values of a_1 . As a_1 decreases, the maximum temperature increases and the hot stripe moves from the center to one edge of the slab.

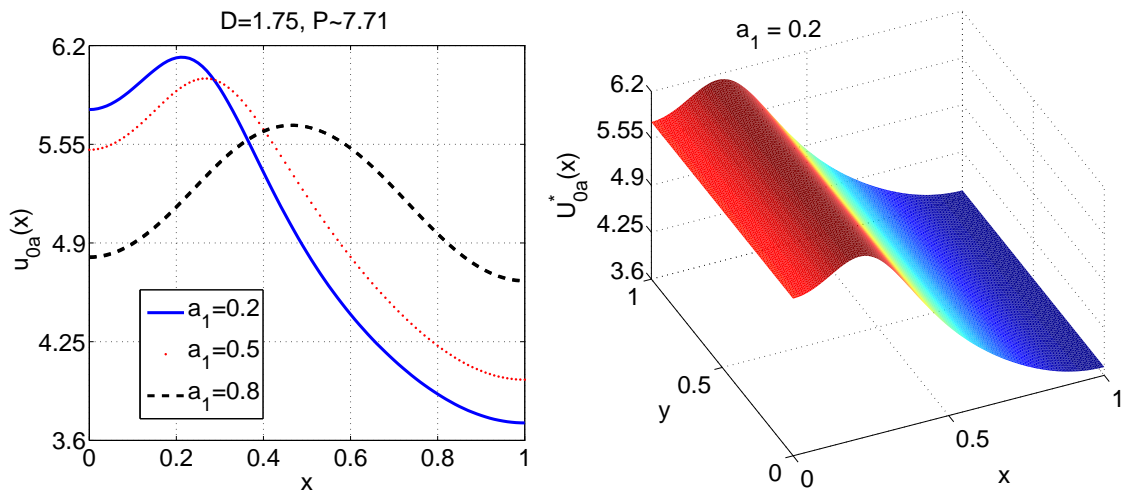


Figure 3.18 $u_{0a}(x)$ and $U_{0a}^*(x)$ for $P \sim 7.71, D = 1.75$.

Next section deals with linear stability of symmetric and asymmetric stripes found in this section. It is known from Chapter 2 that if D is such that a value of power can be chosen so that solutions stay on the symmetric branch, then uniform heating can be obtained for a large value of N . Section 3.3 deals with studying the effect of varying parameters P and D on the stationary solutions and determining their values so that solutions stay on the symmetric branch without getting unstable.

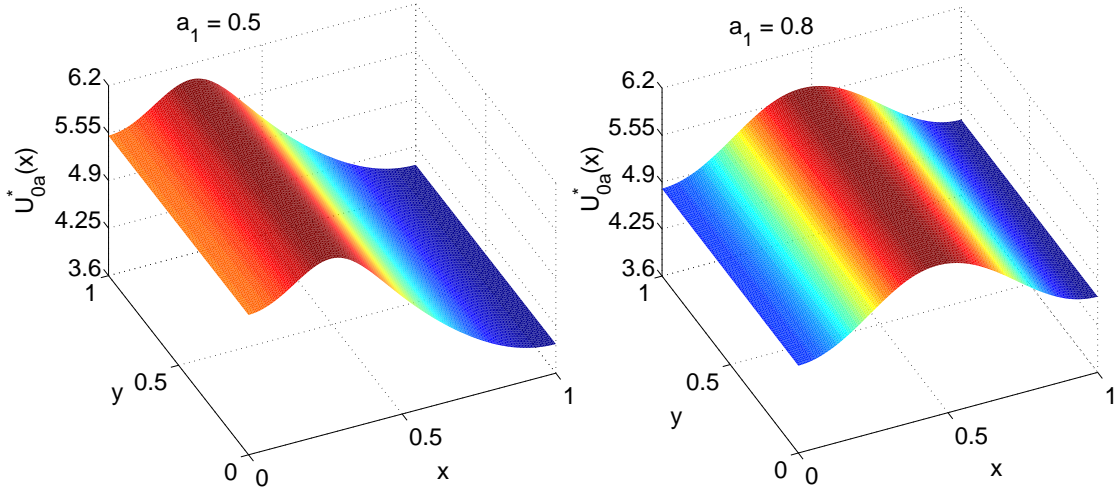


Figure 3.19 $U_{0a}^*(x)$ for $P \sim 7.71$, $D = 1.75$, $a_1 = 0.5, 0.8$.

3.3 Linear Stability

The linear stability of stationary solutions follows a pattern similar to stability of stationary solutions in section 2.2 and is therefore, analyzed using a procedure similar to that followed in Section 2.3. Let $U_0^*(x, y, t) = u_0(x) + V(x, y)e^{-\Lambda t}$, where Λ are the eigen-values. These eigen-values are a function of the dimensionless diffusion coefficient D and the behaviour of the most sensitive eigen-values is studied as D varies. The sign of Λ will determine whether the solution is stable or unstable as it evolves in time. Using the above form of U_0^* in equation (3.5) and replacing 1, 2 by N_1, N_2 in the sine terms, the following non-local eigen-value problem is obtained:

$$D\nabla_{\perp}^2 V + [\Lambda - 2\dot{L}(u_0) + Ce^{Cu_0} \sum_{i=1}^2 I_i(x)]V = 2\chi Ce^{Cu_0} \sum_{i=1}^2 \frac{I_i(x)}{Q_i} \mathcal{L}_i(V), \quad (3.15a)$$

$$\text{where } \mathcal{L}_i(V) = \frac{1}{h} \int_0^h \int_0^1 e^{Cu_0} S_i(x) V(x', y') dx' dy', \quad (3.15b)$$

$$S_i(x) = \sin^2(N_i \pi x), \quad I_i(x) = \Gamma_i a_i S_i(x), \quad (3.15c)$$

$$Q_i = 1 + \chi \int_0^1 e^{Cu_0} S_i(x) dx. \quad (3.15d)$$

V can be expanded in the cosine series:

$$V(x, y) = \sum_{n=0}^{\infty} A_n(x) \cos\left(\frac{n\pi y}{h}\right). \quad (3.16)$$

Inserting the above form of V in equation (3.15a) yields an eigen-value problem for $A_n(x)$:

$$\frac{d^2 A_n}{dx^2} + [\Lambda - l_n^2 - 2\dot{L}(u_0) + Ce^{Cu_0} \sum_{i=1}^2 I_i(x)] A_n \quad (3.17a)$$

$$= \delta_{n0} 2\chi Ce^{Cu_0} \sum_{i=1}^2 \frac{I_i(x)}{Q_i} \int_0^1 g_i(x') A_n(x') dx',$$

$$\frac{dA_n}{dx}(0) = \frac{dA_n}{dx}(1) = 0, \quad (3.17b)$$

where the $g_i, i = 1, 2$ are as defined in equations (3.6a,b), δ_{n0} is the Kronecker delta and

$$l_n^2 = \frac{Dn^2\pi^2}{h^2}, \quad n = 0, 1, 2, \dots$$

When $n = 0$, the right hand side is present which gives rise to a non-local eigen-value problem. The eigen-values are real and well ordered and determine the stability of stationary solutions when there perturbations only in x direction. These eigen-values can be divided into even λ_{2j} and odd λ_{2j+1} depending on the value of j . When j is odd, the right hand side of equation (3.17a) vanishes since the eigen-function is anti-symmetric. Thus, the odd eigen-values are found following the method mentioned in Section 2.3.1.1 used to determine odd eigen-values of the one functional problem for $n = 0$. The even eigen-values can be found by using a slight modification of the method in [13] used to find the non-local eigen-values for the one functional problem. This method will be described shortly.

The right hand side of equation (3.17a) vanishes when $n \geq 1$. This gives rise to an infinite number of Sturm-Liouville problems for the A_n . These problems can be dealt with similarly as the local eigen-value problems for the one functional

problem with $CTg(x)$ in equation (2.10a) replaced by $Ce^{Cu_0} \sum_{i=1}^2 I_i(x)$. Thus, the local eigen-values are

$$\Lambda_{nj} = \mu_j(q, D) + \frac{Dn^2\pi^2}{h^2}, \quad n = 1, 2, 3, \dots, j = 0, 1, 2, \dots \quad (3.18)$$

where μ_j , $j = 0, 1, 2, \dots$ depend on q , the point on the S-shaped curve in Figures 3.3, 3.4 (symmetric stationary solution) or Figures 3.11, 3.12 (asymmetric stationary solution) and the dimensionless diffusion constant D . Also, $\mu_1 = \lambda_1$, which splits into a stable and an unstable portion as a function of q . Applying a similar shooting technique it was found that μ_0 as a function of q is positive for $0 < q < q_c$ and negative for $q > q_c$, regardless of the value of D .

The procedure for determining the non-local eigen-values will now be described.

Consider the related initial value problem

$$D \frac{d^2\phi}{dx^2} + [\lambda - 2\dot{L}(u_0) + Ce^{Cu_0} \sum_{i=1}^2 I_i(x)]\phi = 2C\chi e^{Cu_0} \sum_{i=1}^2 \frac{I_i S_i}{Q_i} \frac{1}{\nu_i}, \quad (3.19a)$$

$$\text{with} \quad \phi(0) = \nu_1\nu_2, \quad \phi_x(0) = 0. \quad (3.19b)$$

Define

$$F(\lambda, \nu_1, \nu_2) = \phi_x(1, \lambda, \nu_1, \nu_2), \quad (3.20a)$$

$$G(\lambda, \nu_1, \nu_2) = \nu_2 - \int_0^1 g_1(x)\phi(x', \lambda, \nu_1, \nu_2)dx', \quad (3.20b)$$

$$H(\lambda, \nu_1, \nu_2) = \nu_1 - \int_0^1 g_2(x)\phi(x', \lambda, \nu_1, \nu_2)dx'. \quad (3.20c)$$

The function $v = \frac{1}{\nu_1\nu_2}\phi$ will satisfy equations (3.17a-3.17c) if there exists a pair (λ, ν_1, ν_2) that satisfies $F = G = H = 0$. To prove this note that $v_x(0) = 0$ by (3.19b) and $v_x(1) = 0$ since $F = 0$. Next, let $v = \frac{\phi}{\nu_1\nu_2}$. Inserting this form of v into equation

(3.19a) and into $G = 0$ and $H = 0$ gives

$$D \frac{d^2 v}{dx^2} + [\lambda - 2\dot{L}(u_0) + C e^{C u_0} \sum_{i=1}^2 I_i(x)] v = 2C \chi e^{C u_0} \left[\frac{I_1 S_1}{Q_1} \nu_2 + \frac{I_2 S_2}{Q_2} \nu_1 \right], \quad (3.21a)$$

$$\nu_2 = \int_0^1 e^{C u_0} S_1(x') \phi(x') dx', \quad (3.21b)$$

$$\text{and } \nu_1 = \int_0^1 e^{C u_0} S_2(x') \phi(x') dx', \quad (3.21c)$$

respectively. Equations (3.21a-c) show that $v = \frac{\phi}{\nu_1 \nu_2}$ satisfies equations (3.17a,b) and is thus, an eigen-function of (3.17a,b) and λ the corresponding eigen-value. A fourth-order Runge-Kutta method is used to numerically solve the initial-value problem (3.19a,b) and a three-dimensional Newton's method is used to find the root (λ, ν_1, ν_2) of the equations $F = G = H = 0$. The continuation procedure described in [13] then yields λ_j, ν_1 and ν_2 as functions of maximum temperature q .

3.3.1 Linear Stability of Symmetric Stationary Solution

The stability of symmetric stripes is determined by using u_{0s} in equation (3.15a). Negative eigen-value represents unstable solution while positive refers to stable solution.

3.3.1.1 Case $n = 0$: Non-Local Eigen-values $\Lambda_{0j}^s = \lambda_j^s$. These eigen-values determine how stable the solutions are to perturbations in x . Figures 3.20 and 3.21 represent the lowest non local eigen-value λ_0^s for $D = 0.75, 1.25$ and $D = 1.75, 2.25$ respectively. The mode λ_0^s is negative and therefore, unstable on the middle branch and stable otherwise.

Next non local eigen-value λ_1^s has been plotted in Figures 3.22 and 3.23 for the same four values of D . This eigen-value has simple zeros at q_b and these zeros are increasing functions of D . Eigen-value λ_1^s is positive before the bifurcation point (P_b, q_b) but is negative after that because another asymmetric stationary branch emerges at this point. The stability of this branch will be studied in Section 3.3.2. As

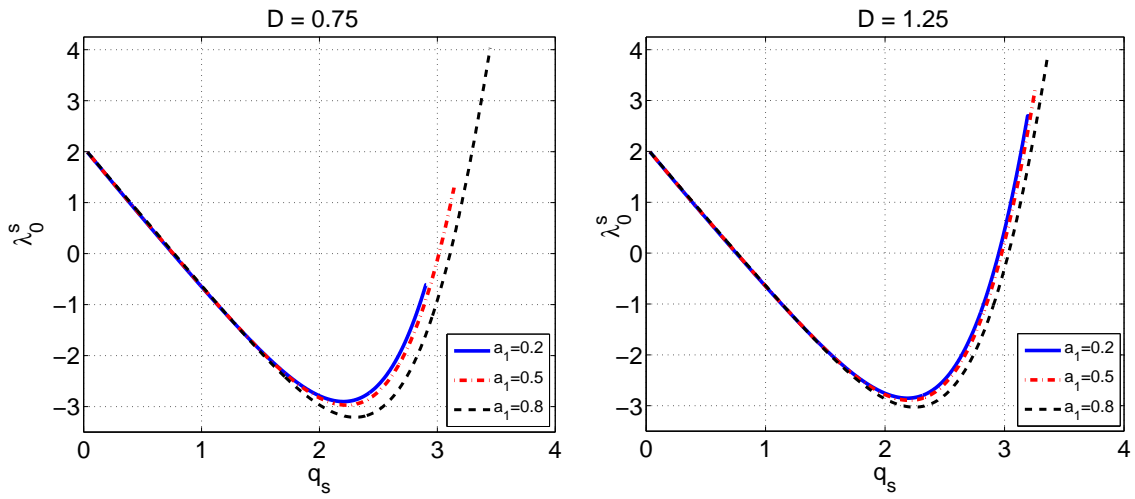


Figure 3.20 Lowest non local eigen-value $\Lambda_{00}^s = \lambda_0^s$ for $D = 0.75, 1.25$.

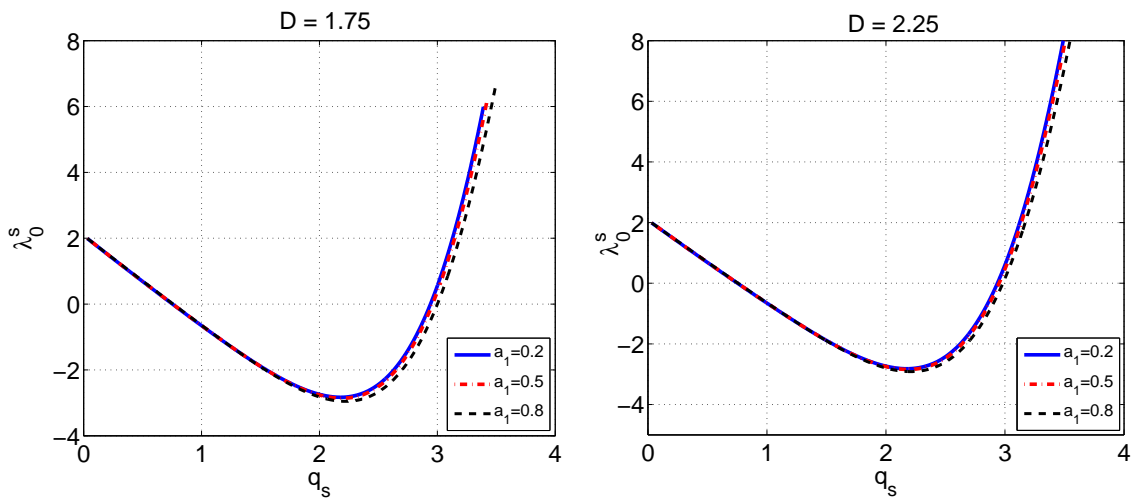


Figure 3.21 Lowest non local eigen-value $\Lambda_{00}^s = \lambda_0^s$ for $D = 1.75, 2.25$.

a_1 increases, the mode λ_1^s becomes more stable since it becomes negative at a higher value of q_s . The stability also increases with D .

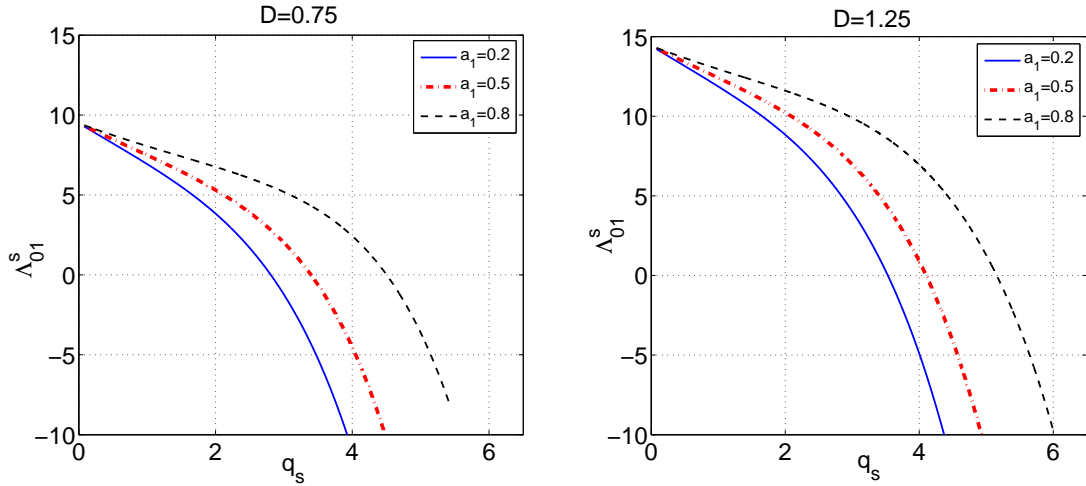


Figure 3.22 Non local eigen-value $\Lambda_{01}^s = \lambda_1^s$ for $D = 0.75, 1.25$.

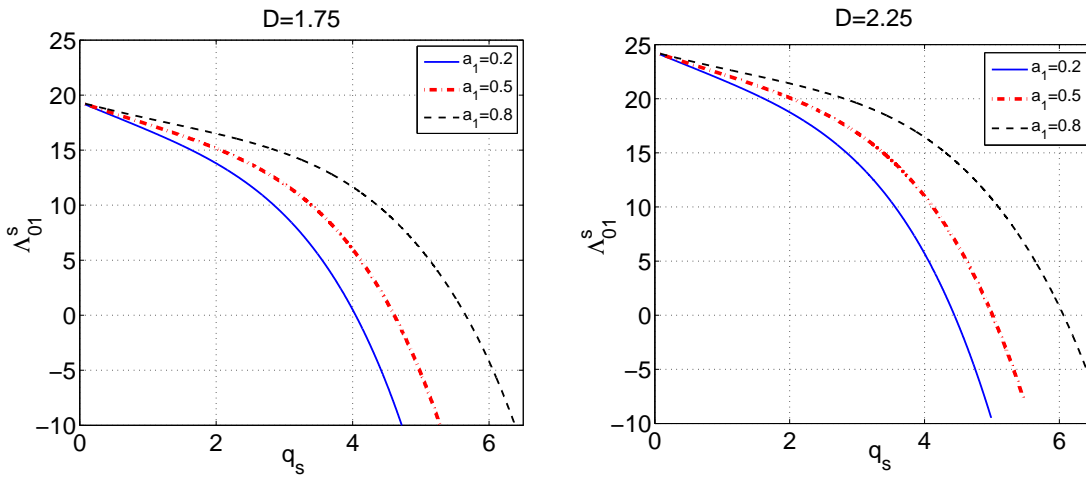


Figure 3.23 Non local eigen-value $\Lambda_{01}^s = \lambda_1^s$ for $D = 1.75, 2.25$.

3.3.1.2 Case $n \geq 1$: Local Eigen-values Λ_{nj}^s . Figures 3.24 and 3.25 depict curves for the first local eigen-value for the symmetric stationary state for four different values of D . This is the most sensitive eigen-value to instabilities in y .

These eigen-values have simple zeros q_{10}^{*s} . These zeros are increasing functions of D and decreasing functions of a_1 .

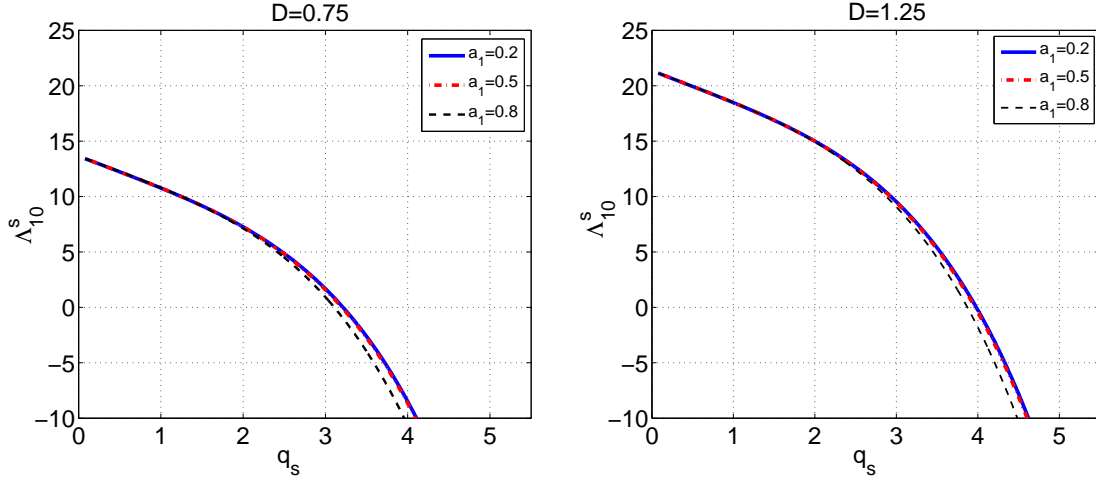


Figure 3.24 First local eigen-value Λ_{10}^s for $D = 0.75, 1.25$.

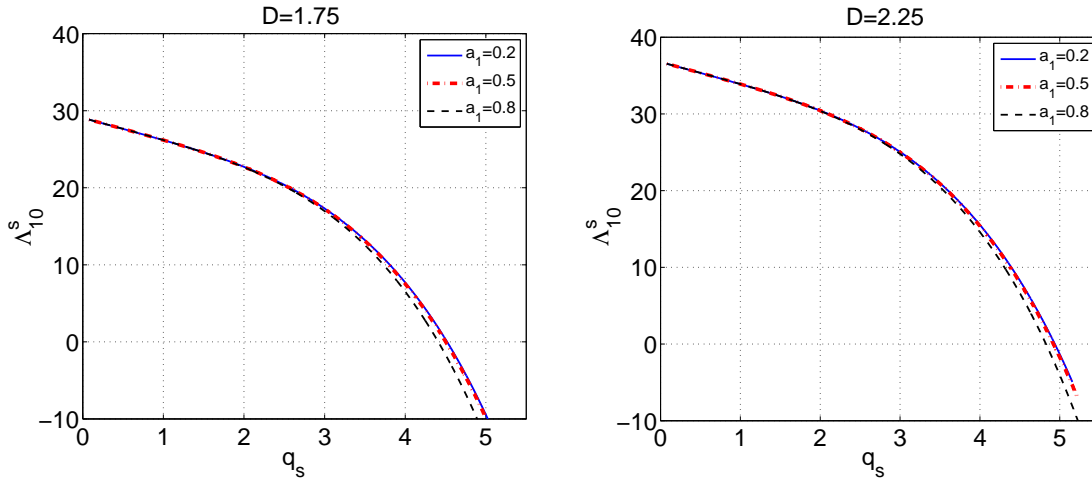


Figure 3.25 First local eigen-value Λ_{10}^s for $D = 1.75, 2.25$.

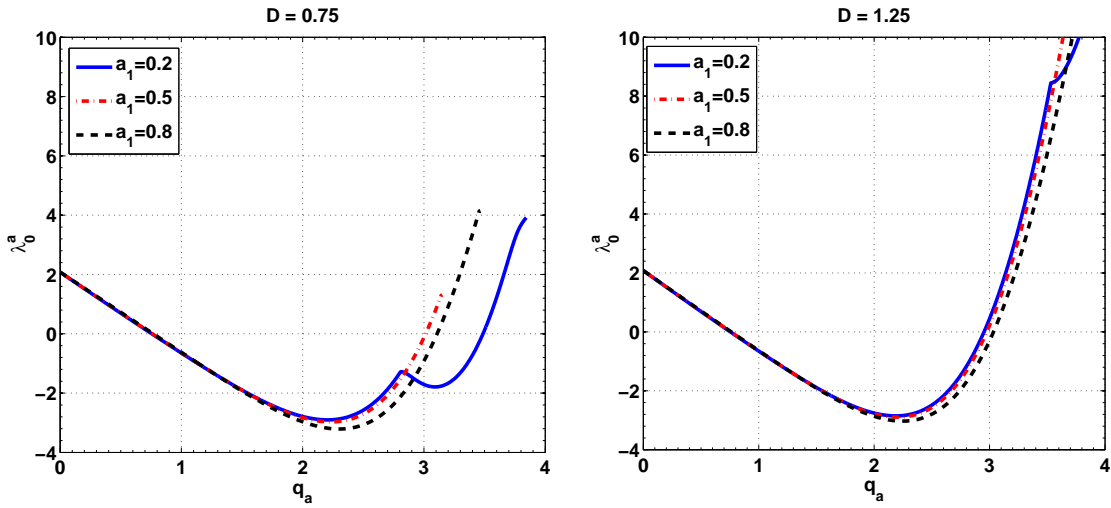
Table 3.1 gives the critical points at which the non-local eigen-value λ_1^s and the local eigen-value Λ_{10}^s become unstable for $D = 1.75$ and $a_1 = 0.2, 0.5, 0.8$.

3.3.2 Linear Stability of Asymmetric Stationary Solution

The stability of asymmetric stripes is determined by using u_{0a} in equation (3.15a).

Table 3.1 Critical Points (P_{crit}, q_{scrit}) for $D = 1.75$, Time Varying Source

a_1	Λ_{01}^s	Λ_{10}^s
0.2	(0.91,4.04)	(1.664,4.52)
0.5	(1.795,4.61)	(1.54,4.5)
0.8	(7.6,5.66)	(1.21,4.41)

**Figure 3.26** Lowest non local eigen-value $\Lambda_{00}^a = \lambda_0^a$ for $D = 0.75, 1.25$.

3.3.2.1 Case $n = 0$: Non-Local Eigen-values $\Lambda_{0j}^a = \lambda_j^a$. Figures 3.26 and 3.27 represent the lowest non local eigen-value λ_0^a and Figures 3.28 and 3.29 depict the next non local eigen-value λ_1^a . As in the symmetric case, λ_0^a is unstable on the middle branch and stable otherwise. For $a_1 = 0.2$ and 0.5 , λ_1^a is zero at the bifurcation point and is positive after that which means that this mode is stable. On the other hand for $a_1 = 0.8$, the eigen-value touches zero but could not be computed beyond that. It appeared that the eigen-value wanted to behave like the one for the symmetric case and go negative beyond zero. This was because of the greater weight of the source term with $N_1 = 1$ but even the small presence of the source with $N_2 = 2$ wanted it to be positive. The result was that the Newton's iterations to compute the eigen-value

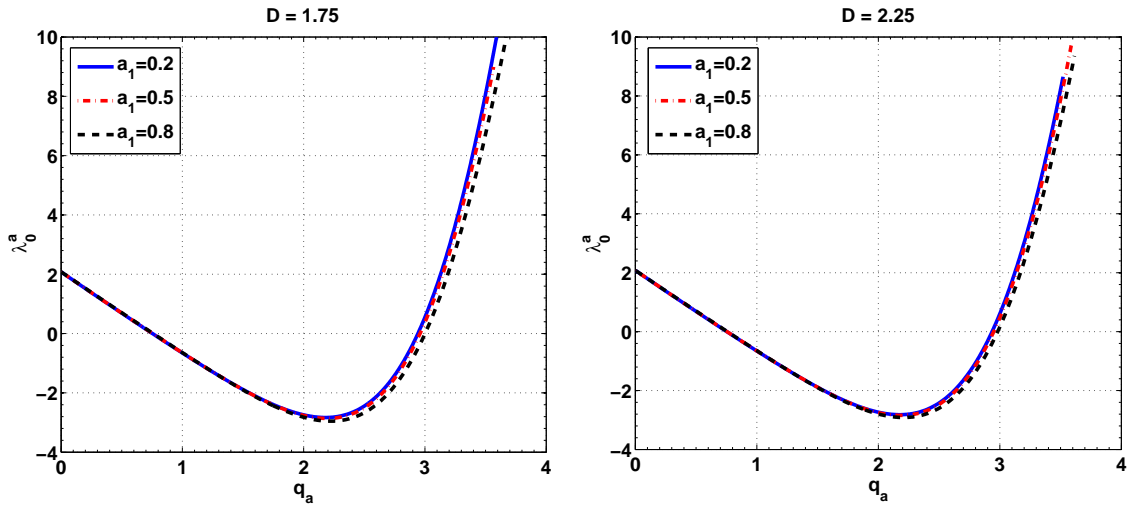


Figure 3.27 Lowest non local eigen-value $\Lambda_{00}^a = \lambda_0^a$ for $D = 1.75, 2.25$.

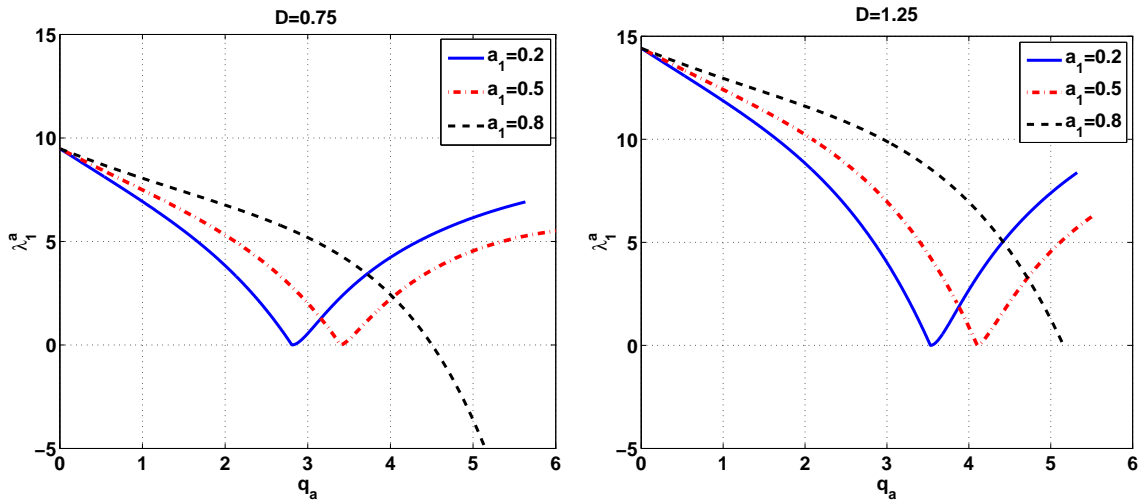


Figure 3.28 Non local eigen-value $\Lambda_{01}^a = \lambda_1^a$.

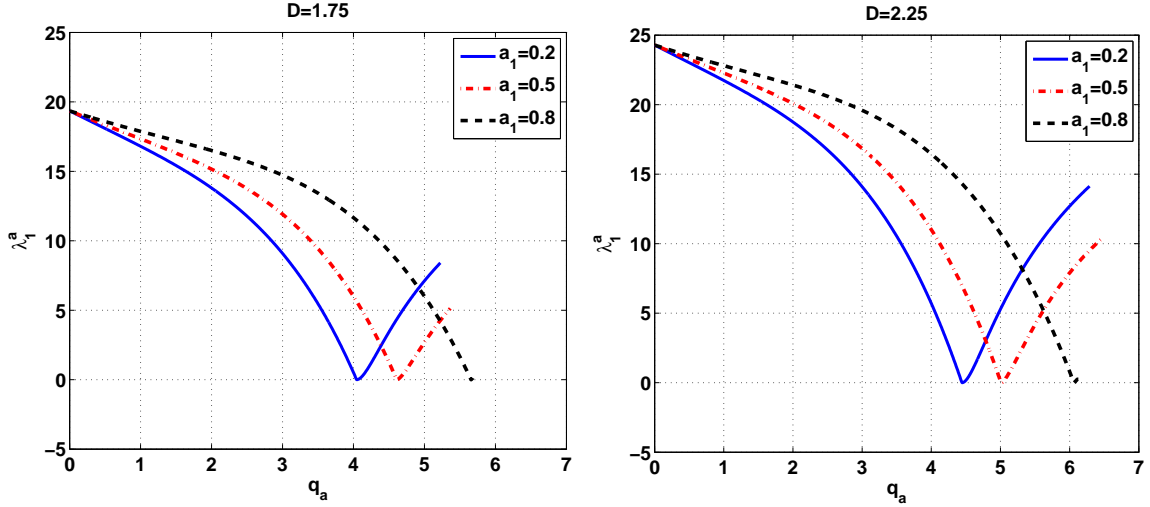


Figure 3.29 Non local eigen-value $\Lambda_{01}^a = \lambda_1^a$.

could not converge to the desired accuracy. Such behaviour of eigen-values requires more analysis and this is under investigation.

3.3.2.2 Case $n \geq 1$: Local Eigen-values Λ_{nj}^a . The curves in Figures 3.30 and 3.31 represent first local eigen-value Λ_{10}^a for four values of D . This eigen-value becomes negative when the lowest anti-symmetric mode in y goes unstable. This eigen-value has simple zeros q_{10}^{*a} so that once this eigen-value is negative, it stays negative thereafter.

The tools for determining which solutions will go unstable at what power for different values of diffusion coefficient are now in place. With the knowledge of stable and unstable eigen-values, values of power can be chosen to get stable symmetric stationary states. The evolution of stationary solutions in time will be studied in next section. If the solution is stable, it will stay at the stationary state. If it is unstable, it will deviate away from the stationary state and evolve to some other state.

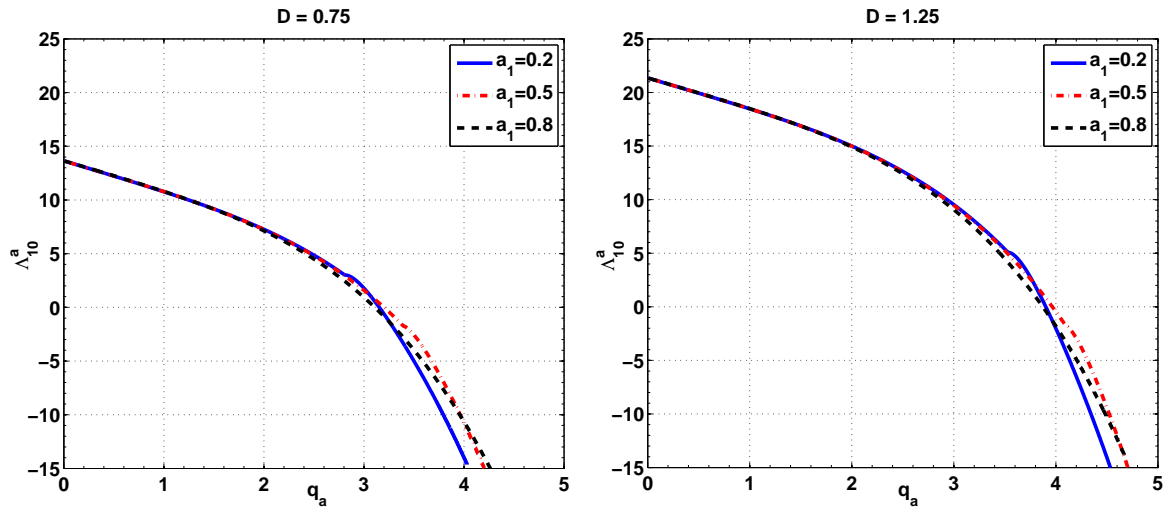


Figure 3.30 Local eigen-value Λ_{10}^a for $D = 0.75, 1.25$.

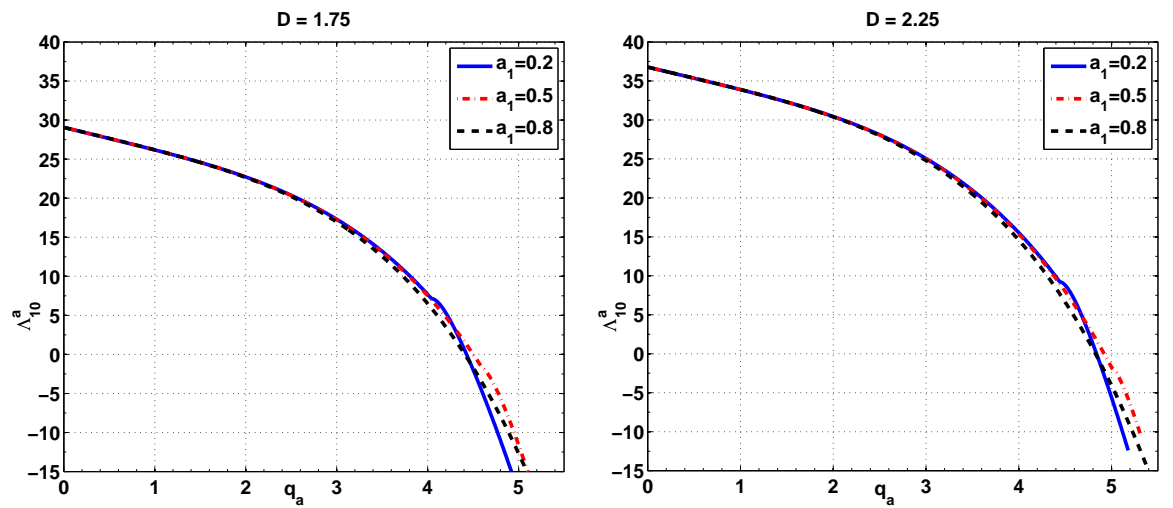


Figure 3.31 Local eigen-value Λ_{10}^a for $D = 1.75, 2.25$.

3.4 Dynamical Simulations

Eigen-values $\lambda_0^s, \lambda_1^s, \Lambda_{10}^s, \lambda_0^a, \lambda_1^a$ and Λ_{10}^a becoming negative suggests that the symmetric stripe solution $U_{0s}^*(x)$ and the asymmetric stripe solution $U_{0a}^*(x)$ are unstable to certain choices of P and D . An explicit two-dimensional finite difference scheme was developed to approximate the solutions of equation (3.5). Time evolution of solutions for $a_1 = 0.2, 0.5, 0.8$ has been analyzed for different values of power. To compare the solutions with those from Chapter 2, the solutions will be studied in greater detail for $D = 1.75$. The other parameters are again fixed:- $\chi = \beta = 0.01, C = 1.5$, values characteristic of the ceramic material being studied.

The time evolution of solutions to equation (3.5) will now be examined. Several different sets of initial data were chosen to understand the dynamics of the heating process. First, homogeneous initial data were chosen for different values of power. When $P < P_c$, initial data evolve to the symmetric stationary state corresponding to the lower branch. On the other hand, when $P > P_c$, initial data evolve to symmetric steady state on the upper branch if $P_c < P < P_b$. When $P > P_b$, the solutions first reach the symmetric steady state on the upper branch but finally evolve to the asymmetric steady state. Even when the power is big enough, there is not enough numerical noise to trigger an instability in the y direction. Numerical noise could only excite the asymmetric mode Λ_{01}^s and the initial data evolve to the asymmetric steady state.

Next, the homogeneous initial data were replaced by the symmetric stationary solution $U_{0s}(x)$ and the corresponding power on the S-shaped curve in Figures 3.3 and 3.4. It took a shorter time to reach the same final state. For $a_1 = 0.2$, λ_1^s becomes unstable when $P \sim 0.91$ (Table 3.1). In simulations with $P < 0.91$, any initial data whether symmetric or not about $x = \frac{1}{2}$ that averaged to stationary solutions corresponding to the upper branch evolved to the symmetric states on the upper branch. On the other hand, when $P > 0.91$, initial data that smoothed out to

symmetric states corresponding to the upper branch evolved to asymmetric stationary states corresponding to the same value of power. If the average was closer to the stationary states on the lower branch, then the initial data evolved to the lower branch solutions for $0.91 < P < P_c$. When $P > P_c$, any initial data evolve to asymmetric steady state.

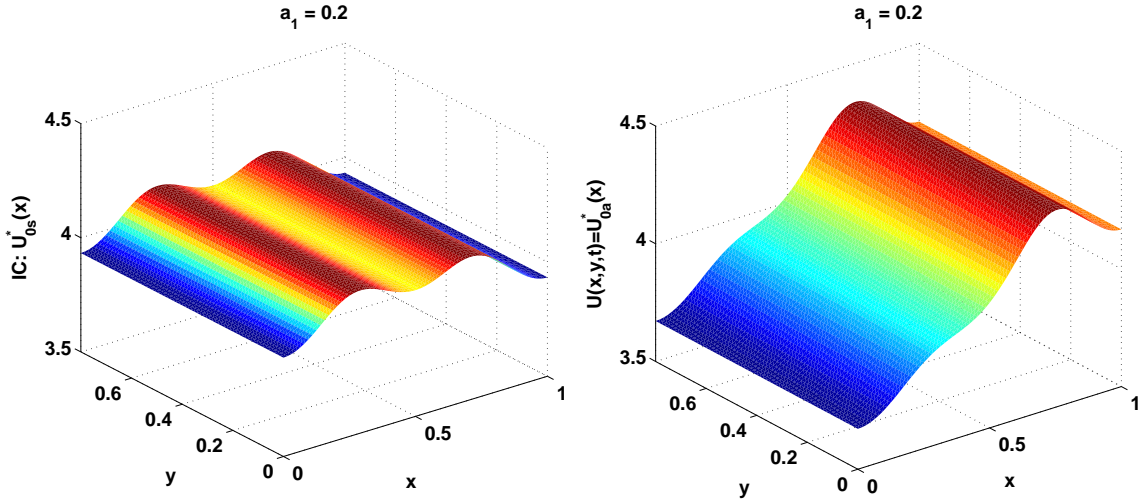


Figure 3.32 $U(x, y, t)$ for $P = 1, D = 1.75$. Initial condition: $U_{0s}^*(x)$.

Figure 3.32 is a plot of solutions for $P \sim 1, D = 1.75, a_1 = 0.2$ when the symmetric steady state was used as the initial condition. At this value of power, Λ_{01}^s is unstable on the upper branch only for $a_1 = 0.2$ and therefore, the symmetric stationary state evolves to the asymmetric steady state. When symmetric steady states for $a_1 = 0.5, 0.8$ were allowed to evolve for the same values of power and D , the solutions just stayed there. This shows that stability increases with a_1 and the possibility of staying on the symmetric branch is greater for a bigger value of a_1 .

Figures 3.33 and 3.34 contain solutions for $P \sim 2$ when Λ_{10}^s is unstable for $a_1 = 0.2, 0.5, 0.8$. Although Λ_{10}^s is unstable at this power, it did not get excited by numerical noise. Instability in solutions was only seen in x -direction due to asymmetric mode Λ_{01}^s in x getting excited by numerical noise.

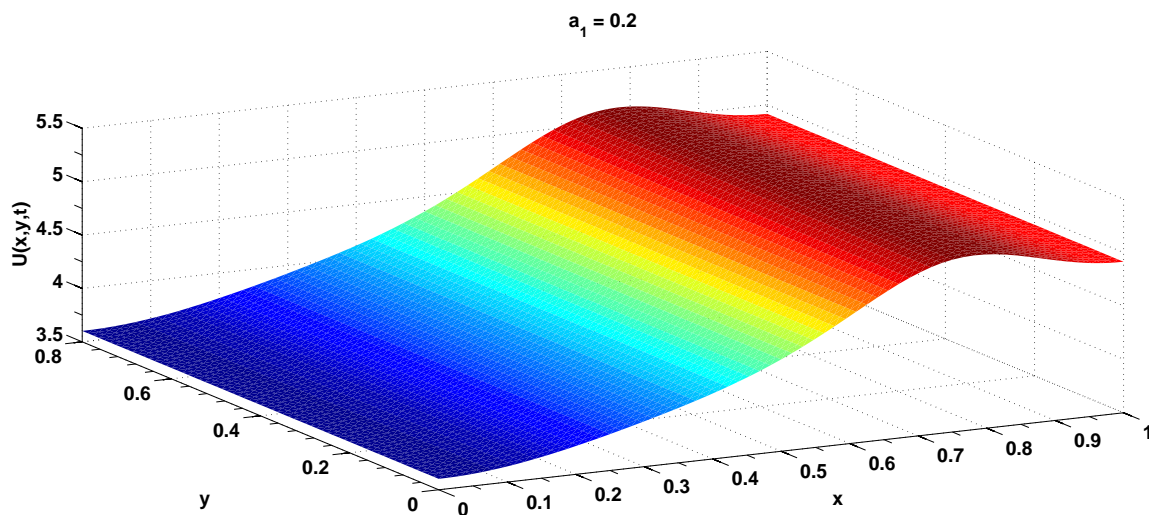


Figure 3.33 $U(x, y, t) = U_{0a}^*(x)$ for $P = 2, a_1 = 0.2$. Initial condition: $U_{0s}^*(x)$.

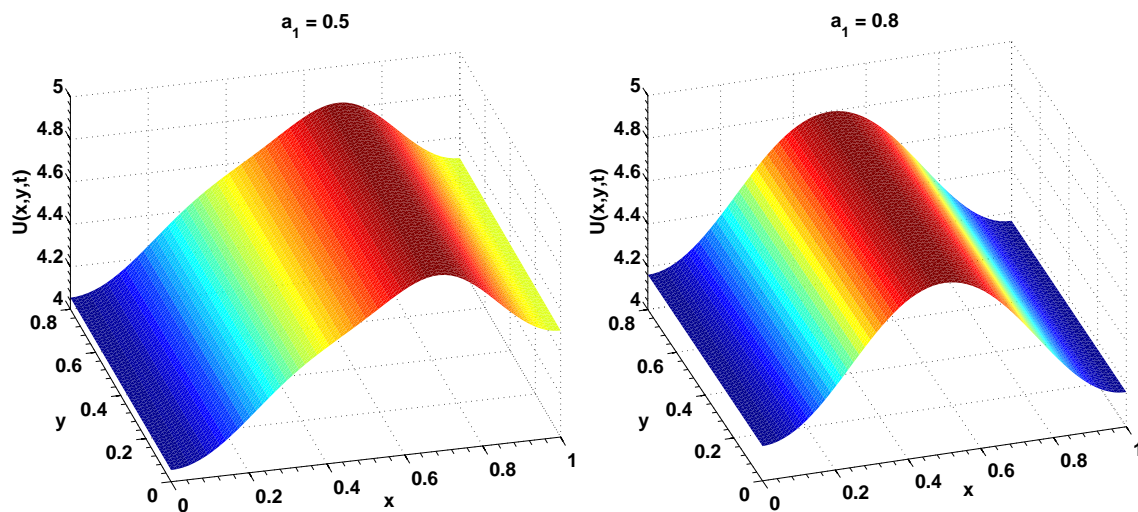


Figure 3.34 $U(x, y, t) = U_{0a}^*(x)$ for $P = 2, a_1 = 0.5, 0.8$. Initial condition: $U_{0s}^*(x)$.

Third, an antisymmetric noise $N(y) = \cos(\frac{\pi y}{h})$ in y was added to the data when the initial data had evolved to the symmetric steady state. That is, the initial data are now

$$U(x, 0) = U_{0s}^*(x) + \epsilon N(y), \quad (3.22)$$

where $\epsilon = 0.01$ is the strength of the noise. The mode Λ_{10}^s becomes unstable when $P \sim 1.664$ for $a_1 = 0.2$. In simulations with $P < 1.664$, solutions evolve either to the symmetric or the asymmetric stationary state. But when $P > 1.664$, a spike was observed at the lower y boundary. The solutions evolved to a spike near $(0.8, 0)$ for $a_1 = 0.2$ as seen in Figure 3.35. These observations hold for $a_1 = 0.5, 0.8$ also since Λ_{10}^s and Λ_{10}^a are unstable for these a_1 when $P \sim 2$. These observations have been presented in Figures 3.36 and 3.37. As a_1 increases, the peaks become lower and also move to the left in x direction.

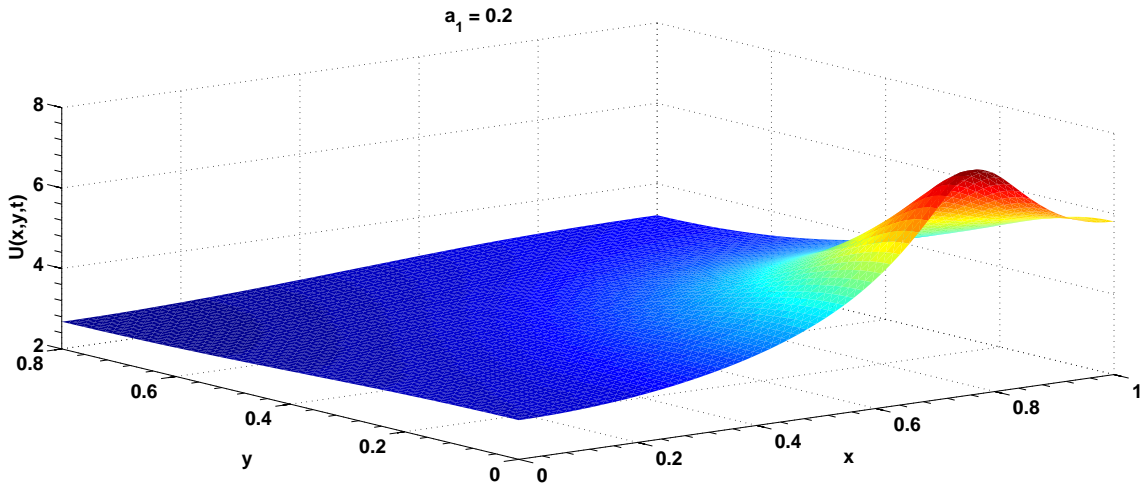


Figure 3.35 $U(x, y, t)$ for $P = 2$. Initial condition: $U_{0s}^*(x) + \epsilon \cos(\frac{\pi y}{h})$.

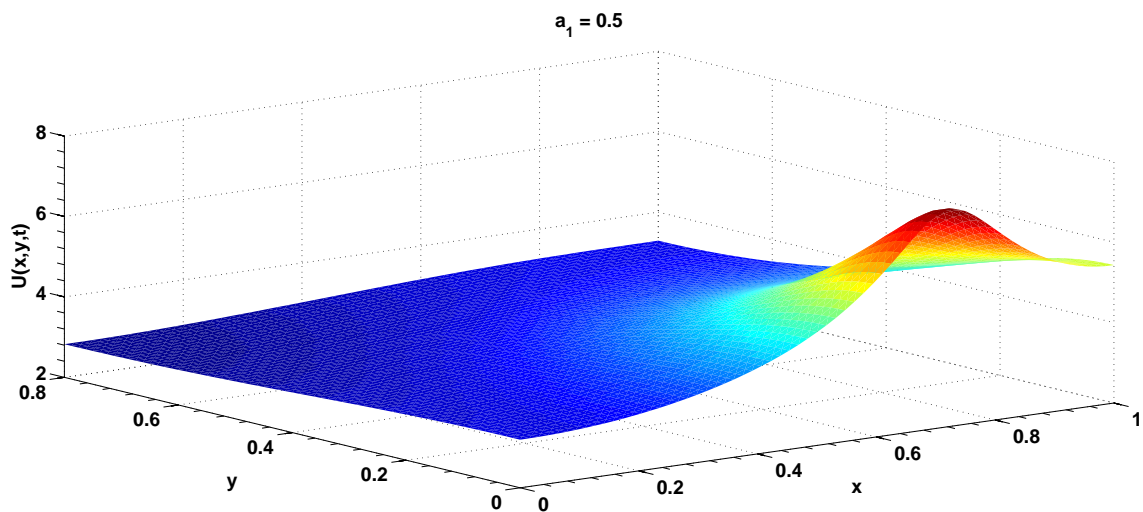


Figure 3.36 $U(x, y, t)$ for $P = 2$. Initial condition: $U_{0s}^*(x) + \epsilon \cos(\frac{\pi y}{h})$.

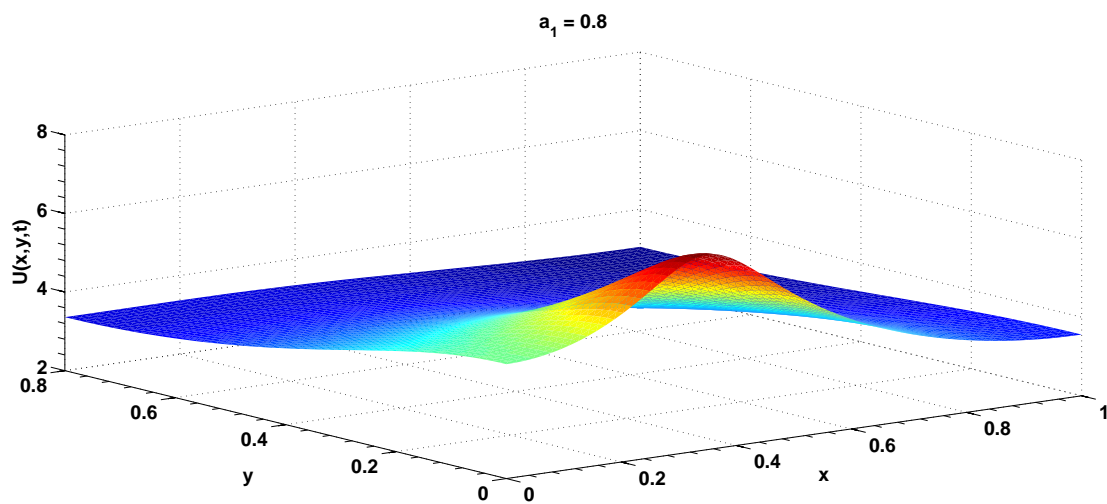


Figure 3.37 $U(x, y, t)$ for $P = 2$. Initial condition: $U_{0s}^*(x) + \epsilon \cos(\frac{\pi y}{h})$.

3.5 Conclusions

The results found in this chapter follow closely the results found for the one functional problem. As mentioned in the introduction, the study of this chapter was motivated by an experiment done by Morris Brodwin [2] to determine whether moving the back wall of the microwave cavity and changing the electric field modal number with time produced more uniform temperature distribution along the surface of the ceramic material. It was found that it is possible to obtain more uniform temperature when the contribution of the larger modal number is more. Thus, the most uniform solution falls somewhere between the solutions from the one functional problem and those from the solutions found in this chapter. If uniformity of solutions is all that is desired then it is enough to use one source and increase the modal number of the electric field. This problem is much simpler than the two functional problem and provides good uniformity for a large enough D as long as the solutions stay on the symmetric branch of the S-shaped curve.

3.6 Future Work

There were problems in computing stationary solutions and eigen-values when certain values of parameters D and a_1 were used. These are:

1. The asymmetric stationary solutions could not be computed for large values of a_1 beyond the bifurcation point. The behaviour of solutions near this point is under further investigation.
2. The lowest non-local eigen-value λ_0^s for the symmetric case could not be computed beyond the point where this eigen-value intersects first local eigen-value Λ_{10s} . This was the case for all four values of D and all three values of a_1 used in this chapter.
3. The second non-local eigen-value λ_1^s for the symmetric case could only be computed till the point where it intersects the lowest non-local asymmetric eigen-value λ_0^a .

4. The second non-local asymmetric eigen-value λ_1^a could not be computed beyond the bifurcation point for large values of a_1 . Further analysis is required to deal with the above problems.

CHAPTER 4

CIRCULAR GEOMETRY

4.1 Introduction

Booske and his colleagues [21, 20] conducted experiments to heat silicon wafers in cylindrical TM_{101} and TM_{111} cavities. They found that the wafers could be rapidly heated, with moderate power in such cavities which suggested that microwave heating may be used as an efficient mechanism for annealing single wafers and bonding several wafers together.

Kriegsmann presented the mathematical problem that described the microwave heating of silicon wafers in cylindrical TM_{101} and TM_{111} cavities [14]. The model took the form of a two-dimensional non-linear heat equation that was solved numerically. Stationary temperature was described as a function of microwave power. Numerical results were in good qualitative agreement with experiments. Modal patterns were observed both in experiments [21, 20] and through numerical simulations [14].

This chapter deals with the study of stability and hot spot formation of solutions in a circular geometry when the modal source is TM_{101} and the time independent solution is a radial solution. When the TM_{101} mode is excited, the heat equation has no angular dependence, so the equation is one-dimensional and the steady state temperature can be efficiently found numerically by using a shooting method, similar to the one for asymmetric stationary solution in Chapter 2.

4.2 Radial Stationary Solutions

The model described in [14] will be studied here. The assumption made in this model is that the thickness of the wafer is much less than its radius so that the fineness ratio $\delta = l/a \ll 1$, where a is the radius and l is the thickness of the wafer, is a small

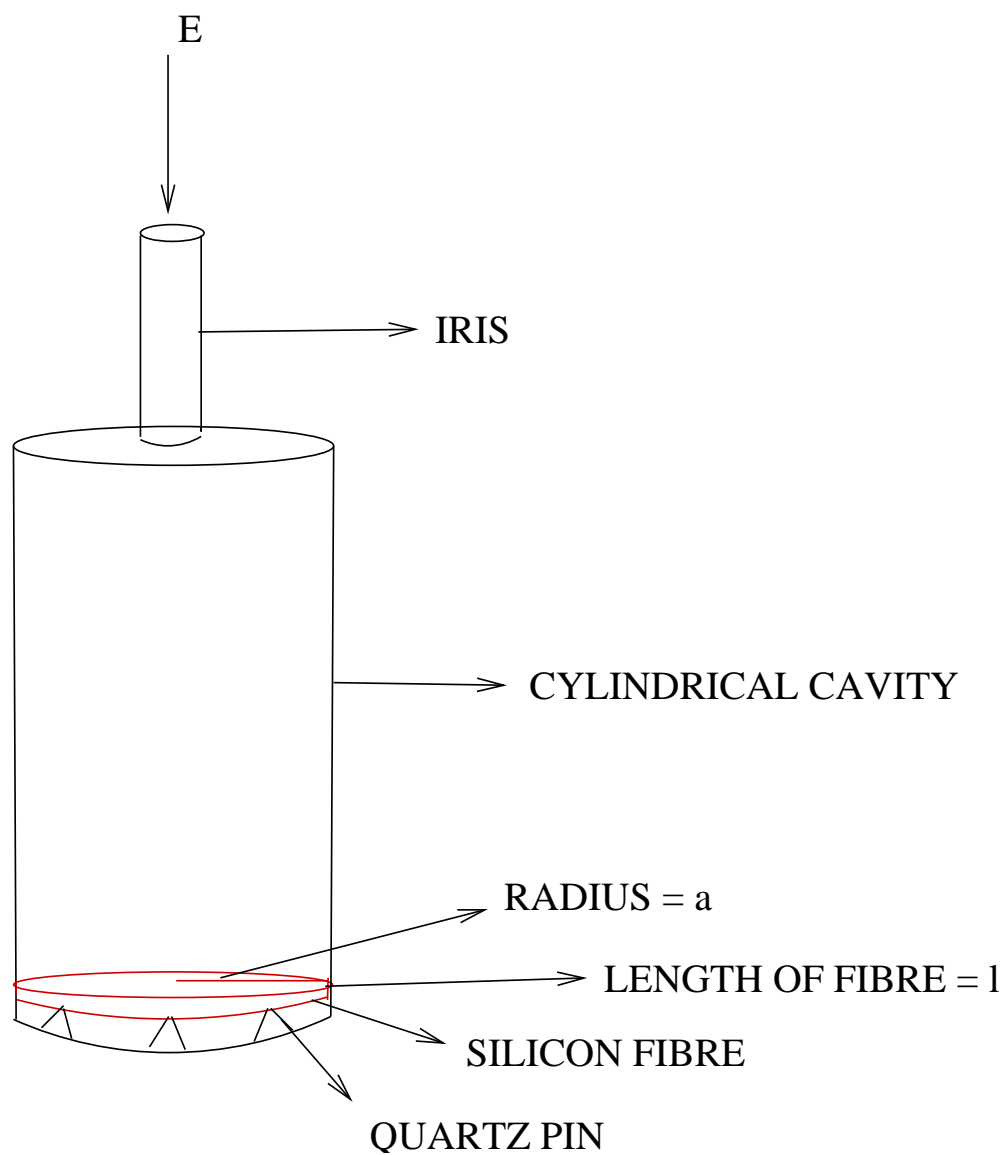


Figure 4.1 Cylindrical Geometry.

parameter. Accordingly, the leading order term $U(r, \theta, t)$ in the asymptotic expansion of the dimensionless temperature in this limit is independent of z and satisfies the non-dimensional reaction diffusion equation

$$U_t = D\nabla_{\perp}^2 U - 2L(U) + Pg(U)\mathbf{S} \quad ; t > 0; 0 < r < 1, \quad (4.1a)$$

$$g(U) = \frac{P}{\left\{1 + \chi \int_0^1 \int_0^{2\pi} e^{CU} \mathbf{S}' dr' d\theta\right\}^2}, \quad (4.1b)$$

$$\mathbf{S} = \begin{cases} J_0^2(z_1^0 r), & z_1^0 = \text{first root of } J_0(r), \\ J_1^2(z_1^1 r), & z_1^1 = \text{first non-zero root of } J_1(r), \end{cases} \quad (4.1c)$$

$$U(r, \theta, 0) = 0, \quad (4.1d)$$

$$\frac{\partial U}{\partial r} = 0, \quad r = 0, 1, \quad (4.1e)$$

where ∇_{\perp}^2 is the Laplacian in r and θ , \mathbf{S} is the electric field source, P is the power applied by the source, C is a positive constant and e^{CU} is the effective electrical conductivity. The boundary loss term $L(U) = U + \delta[(1+U)^4 - 1]$ takes into account the heat losses on the two faces of the wafer. The ambient temperature of the environment including the cavity walls is taken to be 300 °K.

Although the source $J_1^2(z_1^1 r)$ does not admit a physical solution, nevertheless it gives rise to an interesting mathematical problem and is therefore, studied here. The stationary solutions corresponding to the two sources in equation (4.1c) are approximated using the same shooting method and therefore, in this section \mathbf{S} will represent any of the two sources. For convenience, $J_0^2(z_1^0 r)$ and $J_1^2(z_1^1 r)$ are denoted by J_0^2 and J_1^2 respectively. In Figure 4.2, J_0^2 and J_1^2 have been plotted as functions of r . The maximum of J_0^2 is at $r = 0$ and is higher than maximum of J_1^2 which is near $r = \frac{1}{2}$.

When the TM_{101} mode is excited, the heat equation has no angular dependence, so the equation is one-dimensional. Let the θ -independent solution be denoted by u

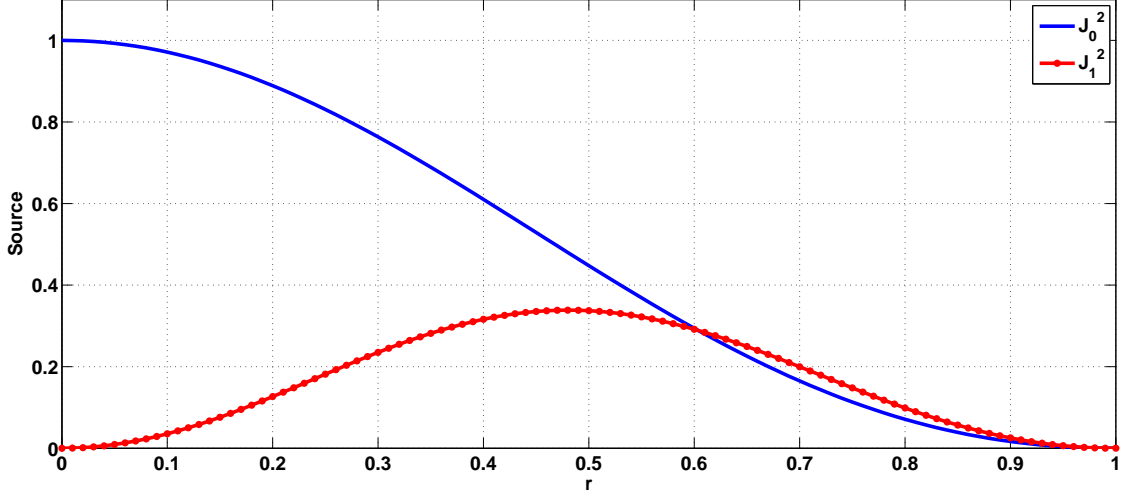


Figure 4.2 Electric field sources J_0^2, J_1^2 as a function of r .

so that the initial boundary value problem is

$$u_t = D(u_{rr} + \frac{1}{r}u_r) - 2L(u) + Pg(u)\mathbf{S}, \quad t > 0; 0 < r < 1, \quad (4.2a)$$

$$u(r, 0) = 0, \quad (4.2b)$$

$$\frac{\partial u}{\partial r} = 0, \quad r = 0, 1. \quad (4.2c)$$

The steady state version of equations (4.2a-c) is a boundary value problem and is similar to equation (2.3a) with a different source and an extra term $\frac{1}{r}u_r$. Thus, the stationary solution u_0 to equations (4.3a-b) below can be found by using a shooting method similar to the one described in [13].

$$D(u_{0rr} + \frac{1}{r}u_{0r}) - 2L(u_0) + Pg(u_0)\mathbf{S} = 0, \quad 0 < r < 1, \quad (4.3a)$$

$$\frac{du_0}{dr} = 0, \quad r = 0, 1. \quad (4.3b)$$

To find u_0 , first consider the related initial value problem

$$D(\varphi_{rr} + \frac{1}{r}\varphi_r) - 2L(\varphi) + \Gamma\mathbf{S}e^{C\varphi} = 0, \quad 0 < r < 1, \quad (4.4a)$$

$$\varphi(0) = \alpha, \quad (4.4b)$$

$$\varphi_r(0) = 0, \quad (4.4c)$$

where Γ is a positive constant. The above initial value problem is solved numerically using a fourth order Runge-Kutta scheme for a fixed α and Γ . The solution of equations (4.4a-c) satisfies equations (4.3a-b) if

$$\varphi_r(1) = 0. \quad (4.5)$$

To begin with, a small value is chosen for α , say α_0 so that equation (4.4a) can be linearized to give

$$D(\varphi_{rr} + \frac{1}{r}\varphi_r) - 2(1 + 4\delta)\varphi + \Gamma\mathbf{S} = 0, \quad 0 < r < 1, \quad (4.6a)$$

$$\frac{d\varphi}{dr} = 0, \quad r = 0, 1. \quad (4.6b)$$

The linear equation (4.6a) can be solved exactly for φ using Green's Function $G(r, r_0)$ for the operator $D(\varphi_{rr} + \frac{1}{r}\varphi_r) - 2(1 + 4\delta)\varphi$:

$$G(r, r_0) = \frac{-1}{DI_1(\nu)} \begin{cases} [K_1(\nu)I_0(\nu r_0) + I_1(\nu)K_0(\nu r_0)] I_0(\nu r), & 0 \leq r < r_0 \leq 1 \\ [K_1(\nu)I_0(\nu r) + I_1(\nu)K_0(\nu r)] I_0(\nu r_0), & 0 \leq r_0 < r \leq 1, \end{cases}$$

In the above equation, $I_i, K_i, i = 0, 1$ are modified Bessel functions of order i and $\nu = \sqrt{\frac{2}{D}}$. Now φ can be found at any point $r_0 \in [0, 1]$:

$$\varphi(r_0) = -\Gamma \int_0^1 G(r, r_0) \mathbf{S} r dr, \quad (4.7a)$$

$$= \frac{\Gamma}{DI_1(\nu)} [A_1 \text{Int}_1 + A_2 \text{Int}_2 + A_3 \text{Int}_3], \quad (4.7b)$$

$$\text{where, } A_1 = K_1(\nu)I_0(\nu r_0) + I_1(\nu)K_0(\nu r_0),$$

$$A_2 = K_1(\nu)I_0(\nu r_0),$$

$$A_3 = I_1(\nu)I_0(\nu r_0),$$

$$\text{Int}_1 = \int_0^{r_0} I_0(\nu r) \mathbf{S} r dr,$$

$$\text{Int}_2 = \int_{r_0}^1 I_0(\nu r) \mathbf{S} r dr,$$

$$\text{Int}_3 = \int_{r_0}^1 K_0(\nu r) \mathbf{S} r dr.$$

Int_1 vanishes when $r_0 = 0$. The value of φ obtained from equation (4.7a) together with α_0 provide an estimate Γ^0 for Γ :

$$\Gamma^0 = \frac{D\alpha_0 I_1(\nu)}{\left[K_1(\nu) \int_0^1 I_0(\nu r) \mathbf{S} r dr + I_1(\nu) \int_0^1 K_0(\nu r) \mathbf{S} r dr \right]}. \quad (4.8)$$

The first integral is regular and can be calculated using the trapezoidal rule. The second integral is singular at the origin and can be broken into a singular and a regular part:

$$\int_0^1 K_0(\nu r) \mathbf{S} r dr = \int_0^h K_0(\nu r) \mathbf{S} r dr + \int_h^1 K_0(\nu r) \mathbf{S} r dr \quad (4.9)$$

The first integral on the right is the singular part and can be written as

$$\int_0^h K_0(\nu r) \mathbf{S} r dr = - \int_0^h \log\left(\frac{\nu r}{2}\right) I_0(\nu r) \mathbf{S} r dr + \int_0^h \frac{(\frac{\nu r}{2})^{2m}}{(m!)^2} \Psi(m+1) \mathbf{S} r dr, \quad (4.10)$$

where $\Psi(m+1) = \frac{\Upsilon'(m+1)}{\Upsilon(m+1)}$ and Υ is the Gamma function. The first integral is $\sim \frac{h^2}{2} (\log(\frac{\nu h}{2}) - \frac{1}{2}) \sim 0$ and the second integral vanishes near $r = 0$. Thus,

$$\Gamma^0 = \frac{D\alpha I_1(\nu)}{\left[K_1(\nu) \int_0^1 I_0(\nu r) \mathbf{S} r dr + I_1(\nu) \int_h^1 K_0(\nu r) \mathbf{S} r dr \right]}. \quad (4.11)$$

Newton's method is then applied using Γ^0 as the initial guess which then yields the true value Γ_0 . Once Γ_0 is obtained, a slightly larger value of α say $\alpha_1 = \alpha_0 + d\alpha$ is chosen and Γ_0 is taken as the initial guess to obtain Γ_1 . This procedure is continued which yields the function $\Gamma(\alpha)$. Equation (4.3a) will be completely satisfied when

$$P = \Gamma(\alpha) \left\{ 1 + 2\pi\chi \int_0^1 e^{C\varphi} \mathbf{S}' dr' \right\}^2. \quad (4.12)$$

Equation (4.12) implicitly defines the temperature at the center of the fibre as a function of dimensionless power P . This temperature is maximum along the fibre when $\mathbf{S} = J_0^2$. Each value of α yields a stationary solution. For each solution it can be shown graphically that there is a one-one correspondence between α and the

maximum temperature q . Since it is of interest to study different parameters as a function of maximum temperature, therefore, Γ is treated as a function of q and q is used for plotting results. The parameters $C = 1.5, \delta = 0.01, \chi = 0.01$ are fixed.

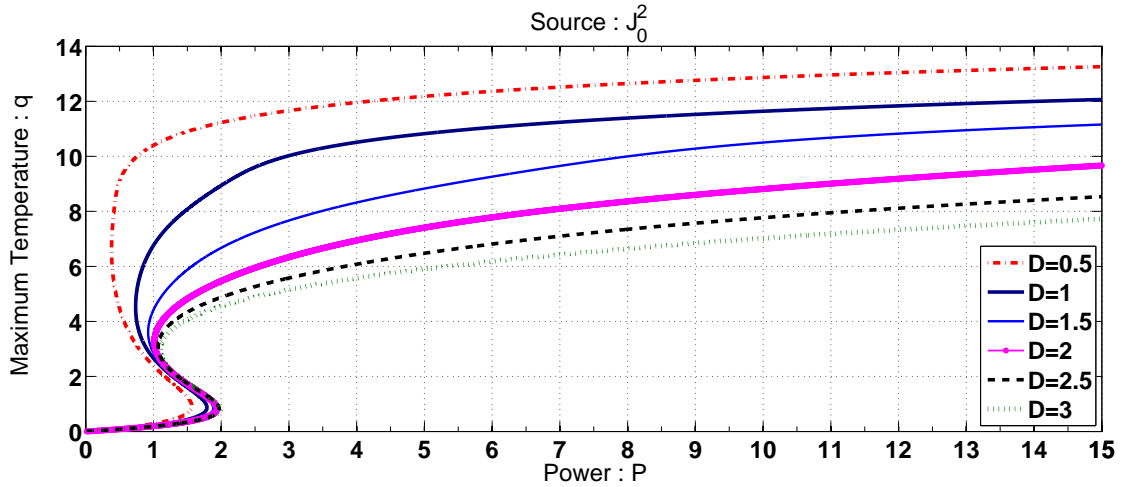


Figure 4.3 q as a function of P ; $S = J_0^2$.

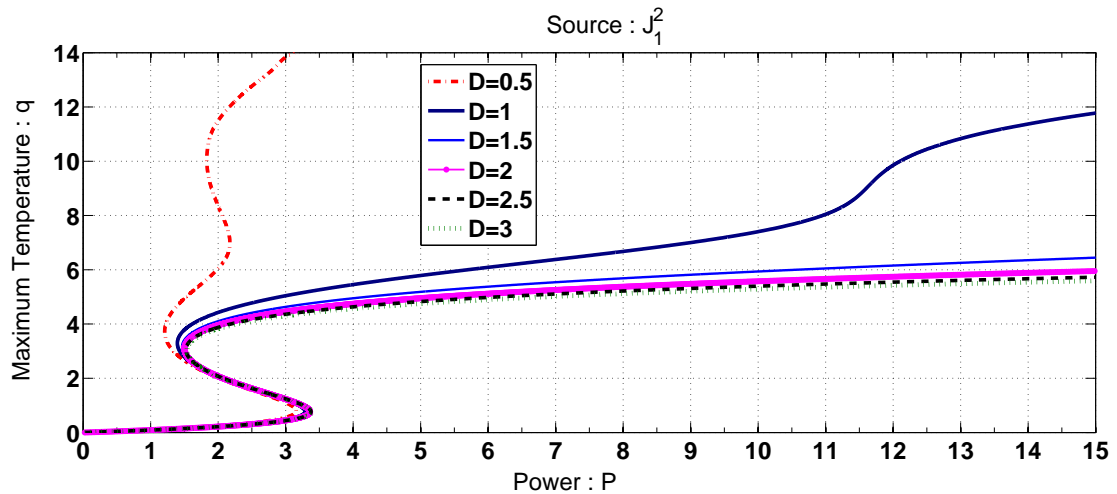


Figure 4.4 q as a function of P ; $S = J_1^2$.

Figures 4.3 and 4.4 represent maximum temperature as a function of power for six different values of D . For the same value of power, maximum temperature increases as the diffusion coefficient decreases. Figures 4.5 and 4.6 depict the profile of stationary solutions u_0 as they vary with r for $D = 2$ and $P \sim 1.75$ corresponding

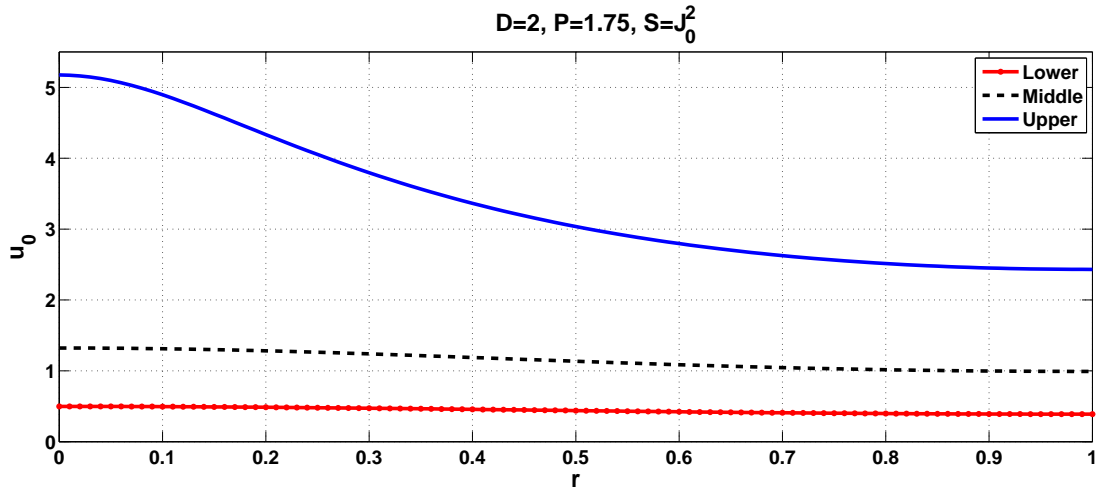


Figure 4.5 $u_0(r)$ for $S = J_0^2$, $D = 2$, $P \sim 1.75$, three branches.

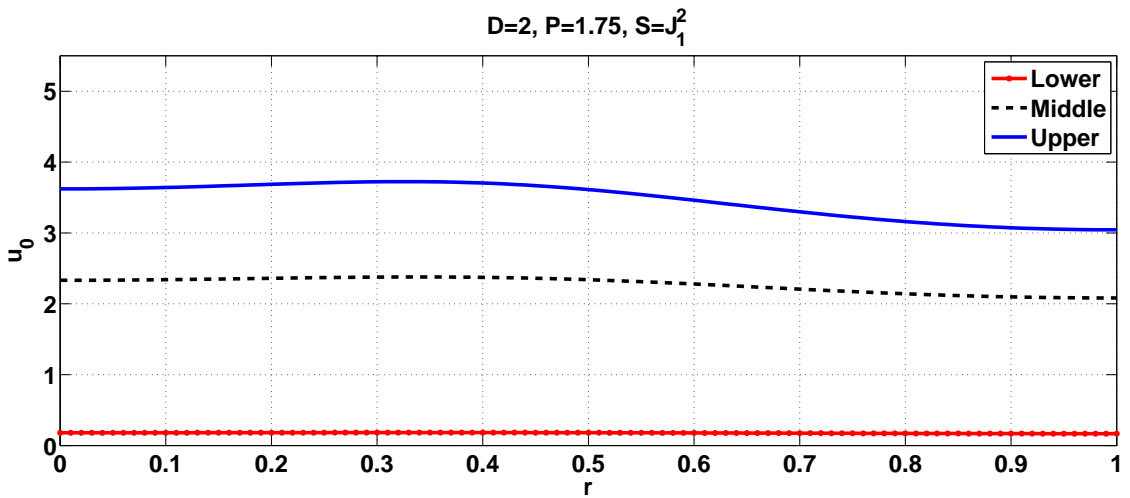


Figure 4.6 $u_0(r)$ for $S = J_1^2$, $D = 2$, $P \sim 1.75$, three branches.

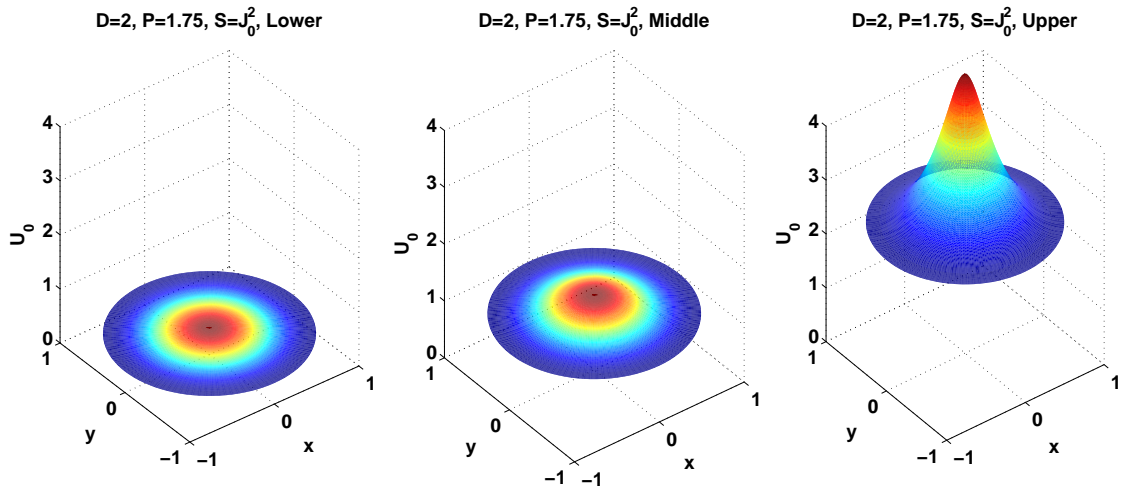


Figure 4.7 $U_0(x, y)$ for $S = J_0^2$, $D = 2$, $P \sim 1.75$, three branches.

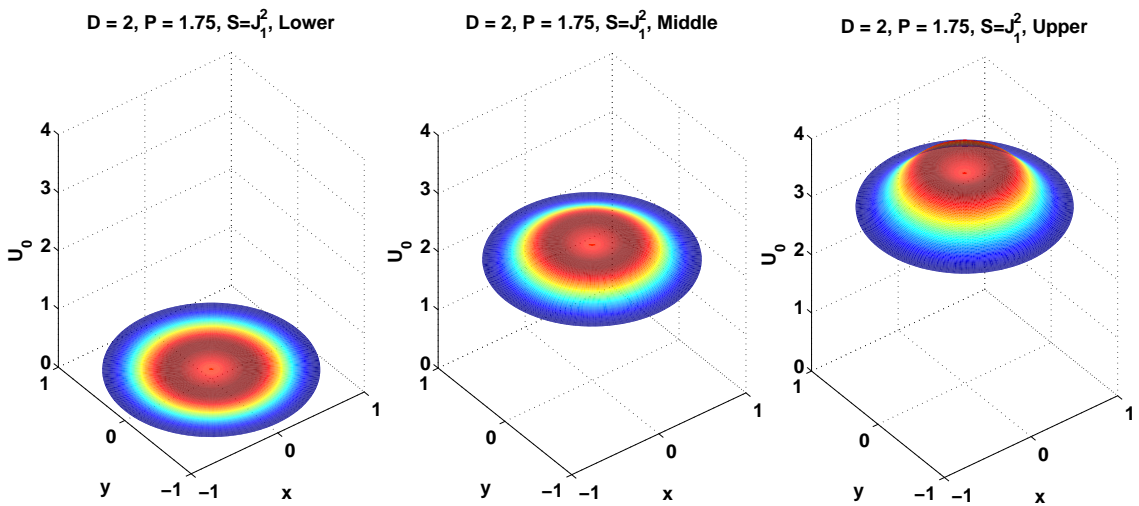


Figure 4.8 $U_0(x, y)$ for $S = J_1^2$, $D = 2$, $P \sim 1.75$, three branches.

to lower middle and upper branches of curves in Figures 4.3 and 4.4 respectively. A 3-dimensional version in rectangular coordinates has been shown in Figures 4.7 and 4.8 by using the conversion $x = r \cos(\theta), y = r \sin(\theta)$. Since x, y and u_0 are all functions of r and θ , therefore, $u_0(r) \equiv U_0(x, y)$ and thus, U_0 is plotted as a function of x and y .

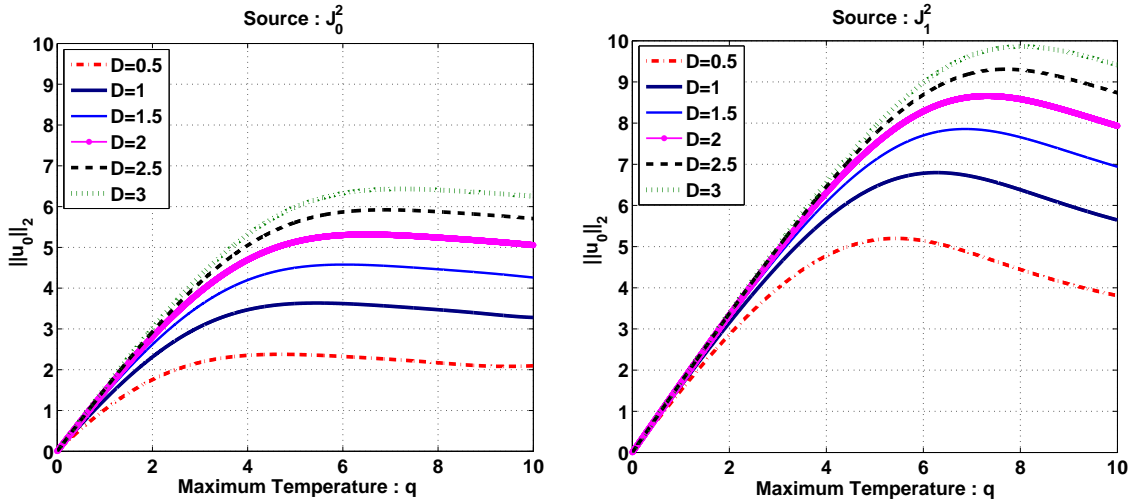


Figure 4.9 $\|u_0\|_2$ as a function of q ; $S = J_0^2, J_1^2$.

The stationary solution u_0 has only one local maxima in $[0, 1]$, a property similar to the solutions of equation 2.3a for $N = 1$. This suggests that there are no bifurcations to the solutions. The L_2 norm gives a measure of the total energy of the solution. Figure 4.9 plots $\|u_0\|_2$ as a function of maximum temperature. The L_2 norm increases initially but then begins to decrease. This shows that $\|u_0\|_2$ is not a monotonic function of q . Although maximum temperatures were higher for J_0^2 than those for J_1^2 , $\|u_0\|_2$ is higher for J_1^2 when comparisons are done for the same value of power.

Next, Figures 4.10 and 4.11 contain curves for $u_0(r)$ for six values of D when $P \sim 1.75$. As the diffusion coefficient decreases, maximum temperature increases and the solutions become more localized. Figures 4.12, 4.13, 4.14 and 4.15 show a

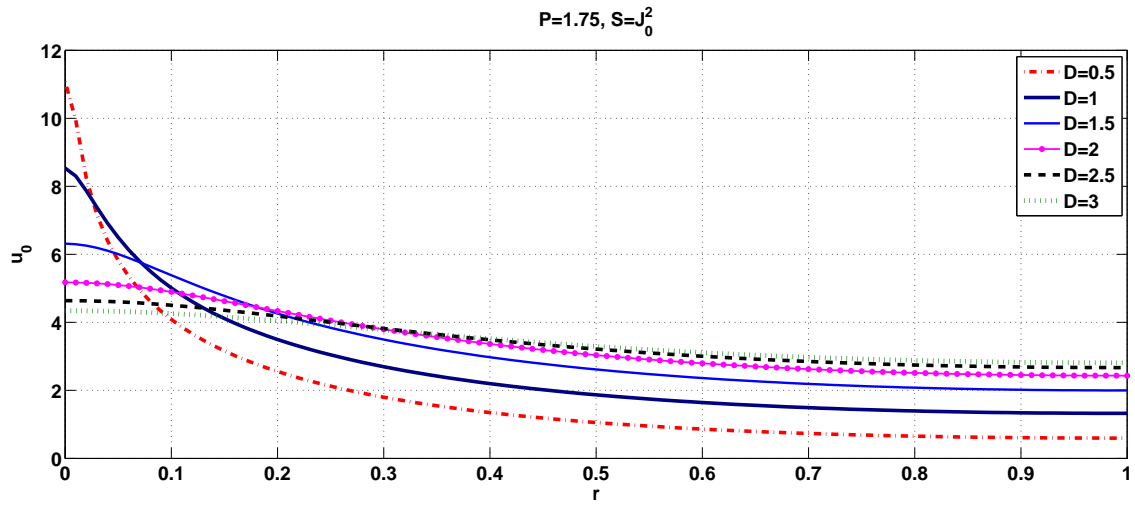


Figure 4.10 $u_0(r)$ for $P \sim 1.75, S = J_0^2$, upper branch.

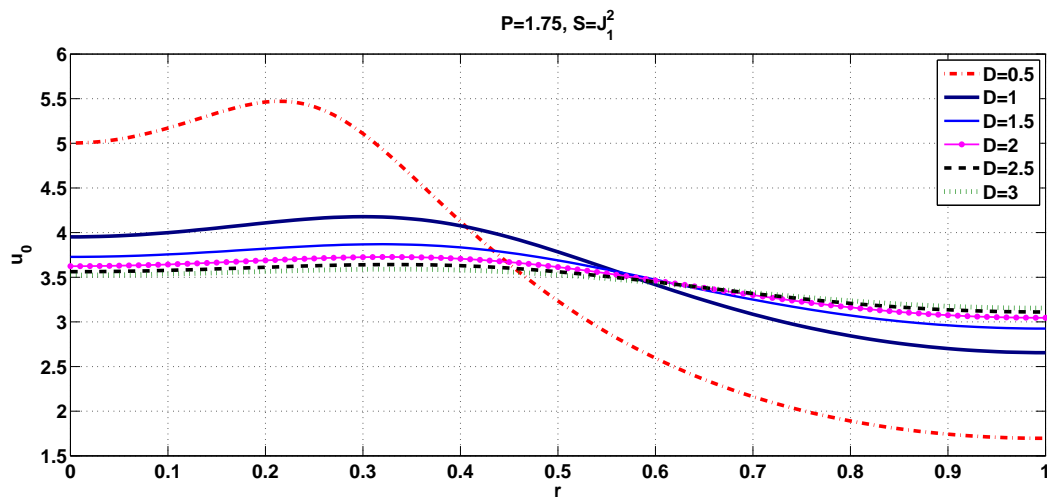


Figure 4.11 $u_0(r)$ for $P \sim 1.75, S = J_1^2$, upper branch.

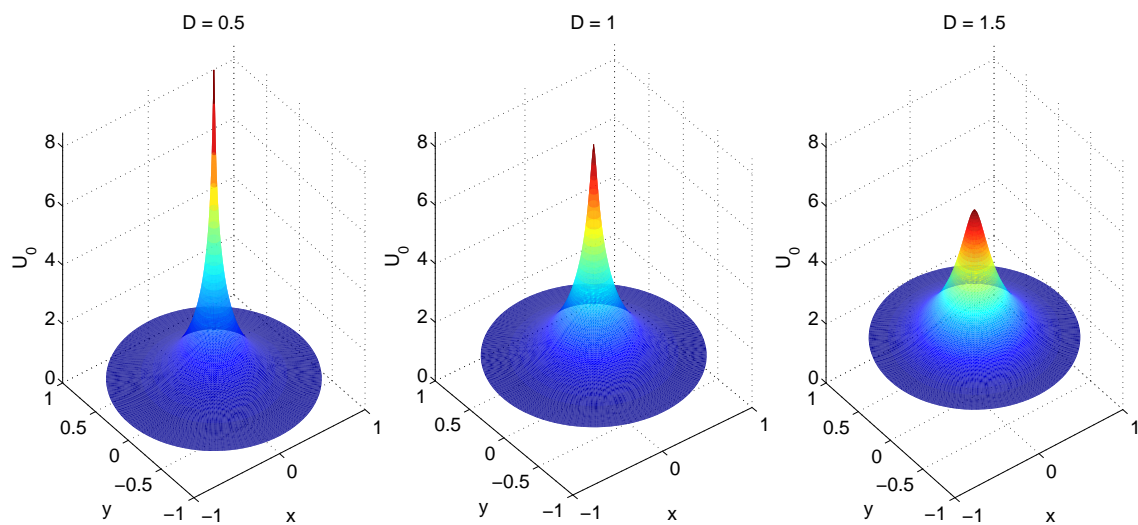


Figure 4.12 $U_0(x, y)$ for $P \sim 1.75$, upper branch, $\mathbf{S} = J_0^2$.

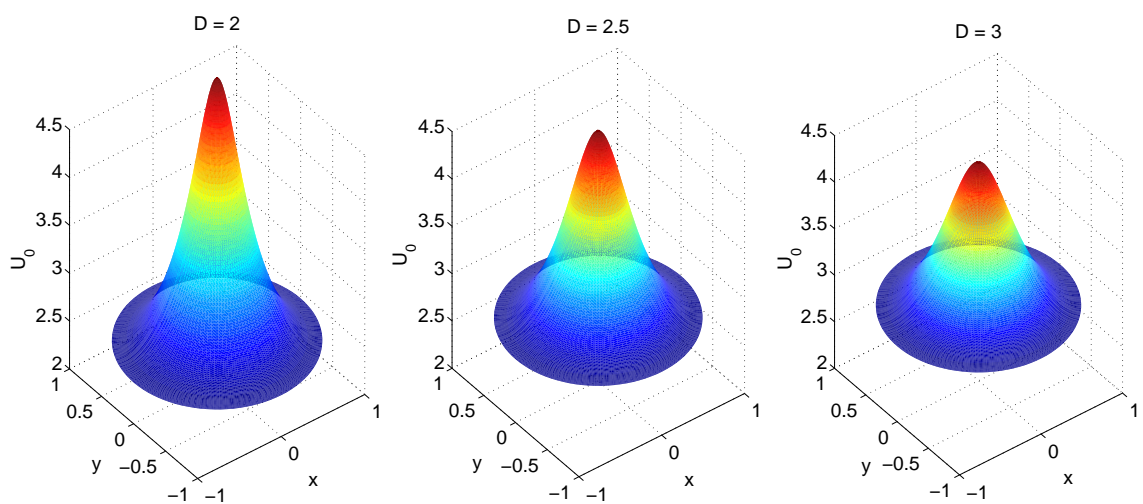


Figure 4.13 $U_0(x, y)$ for $P \sim 1.75$, upper branch, $\mathbf{S} = J_0^2$.

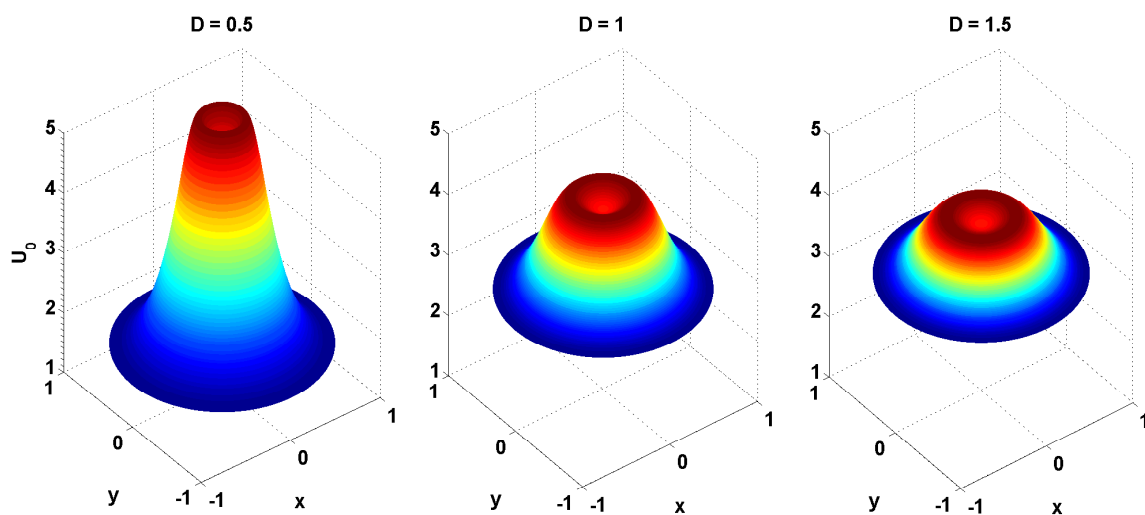


Figure 4.14 $U_0(x, y)$ for $P \sim 1.75$, upper branch, $S = J_1^2$.

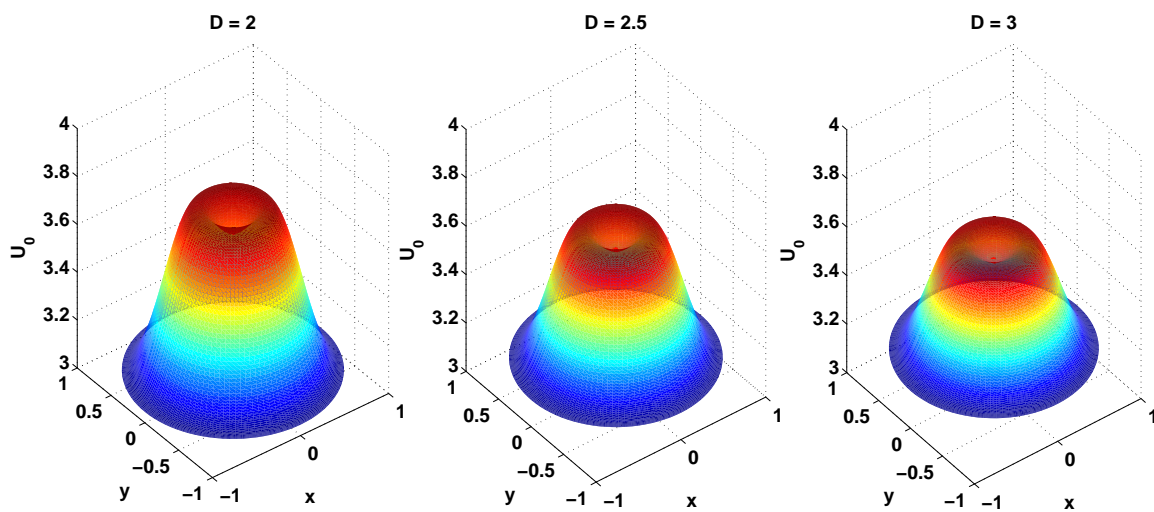


Figure 4.15 $U_0(x, y)$ for $P \sim 1.75$, upper branch, $S = J_1^2$.

three-dimensional version $U_0(x, y)$ for $P = 1.75$ for same six values of D . Next section addresses the stability of these solutions as they evolve in time.

4.3 Linear Stability

The linear stability of the stationary solution $u_0(r)$ will now be investigated numerically.

Let $U(r, \theta, \tau) = u_0(r) + e^{-\Lambda\tau}V(r, \theta)$. Inserting this in equation (4.1a) gives:

$$D \left\{ V_{rr} + \frac{1}{r}V_r + \frac{1}{r^2}V_{\theta\theta} \right\} + \left\{ \Lambda - 2\dot{L}(u_0) + \Gamma Cg(r) \right\} V = \frac{2\chi C\Gamma}{Q} \mathcal{L}(V), \quad (4.13a)$$

$$\text{where } g(r) = \mathbf{S}e^{Cu_0}, \quad \mathcal{L}(V) = \int_0^{2\pi} \int_0^1 g(r)g(r')V(r', \theta')r'dr'd\theta', \quad (4.13b)$$

$$Q = 1 + \chi \int_0^1 g(r)dr, \quad \Gamma = \frac{P}{Q^2}, \quad (4.13c)$$

$$\frac{dV}{dr} = 0, \quad r = 0, 1. \quad (4.13d)$$

V can be expanded in the cosine series:

$$V(r, \theta) = \sum_{n=0}^{\infty} A_n(r) \cos(n\theta). \quad (4.14)$$

Using the above expansion of V in equation (4.13a) gives an eigen-value problem for A_n :

$$D \left\{ \frac{d^2 A_n}{dr^2} + \frac{1}{r} \frac{dA_n}{dr} \right\} + \left\{ \Lambda - \frac{n^2}{r^2} - 2\dot{L}(u_0) + C\Gamma g(r) \right\} A_n = \delta_{n0} \frac{2C\chi\Gamma}{Q} \mathcal{L}(A_n), \quad (4.15a)$$

$$\mathcal{L}(A_n) = \int_0^{2\pi} \int_0^1 g(r)g(r')A_n(r')r'dr'd\theta', \quad (4.15b)$$

$$\frac{dA_n}{dr}(0) = \frac{dA_n}{dr}(1) = 0, \quad (4.15c)$$

where δ_{n0} is the Kronecker delta. The above eigen-value problem is non-local when $n = 0$, due to the presence of the inhomogeneous term on the right side of the equation. In this case, the spectrum is real, discrete and well-ordered. The non-local eigen-values are denoted by (λ_j, ψ_j) and are found following the procedure described in [13]. When $P \ll 1$, a simple perturbation expansion of equation (4.13a) as $P \rightarrow 0$

yields

$$\psi_0 = 1 + O(P), \quad (4.16)$$

$$\psi_j = J_0(z_1^j r) + O(P), j \geq 1 \quad (4.17)$$

$$\lambda_0 = 2(1 + 4\delta) + O(P), \quad (4.18)$$

$$\lambda_j = D(z_1^j)^2 + 2(1 + 4\delta) + O(P), j \geq 1 \quad (4.19)$$

where again $\delta = l/a$, where a is the radius and l is the thickness of the wafer, $z_1^j, j \geq 1$ is the j^{th} root of Bessel function J_1 and λ_0 and λ_j depend on the source \mathbf{S} being considered. Newton's method is now used to determine λ_j as a function of q . The eigen-values and eigen-functions are computed using the values of P and $u_0(r)$ found in Section 4.2.

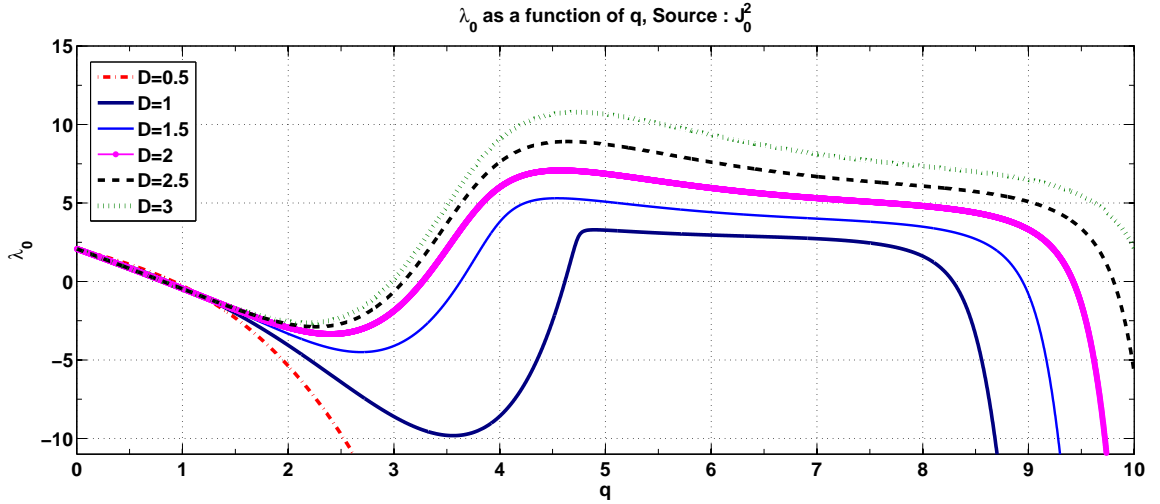


Figure 4.16 Lowest eigen-value λ_0 as a function of q , $\mathbf{S} = J_0^2$.

The stability of stationary solutions depends on the lowest non-local eigen-value λ_0 . In Figures 4.16, 4.17, 4.18 and 4.19, the λ_0 and next non-local eigen-value λ_1 have been plotted as a function of q for $D = 0.5, 1, 1.5, 2, 2.5, 3$. A usual trend is observed initially where λ_0 is negative on the middle branch ($P_L < P < P_c$) and positive on lower and upper branches. But further on the upper branch of the response curve, λ_0 becomes negative again. It is not clear why the eigen-value λ_0 becomes negative

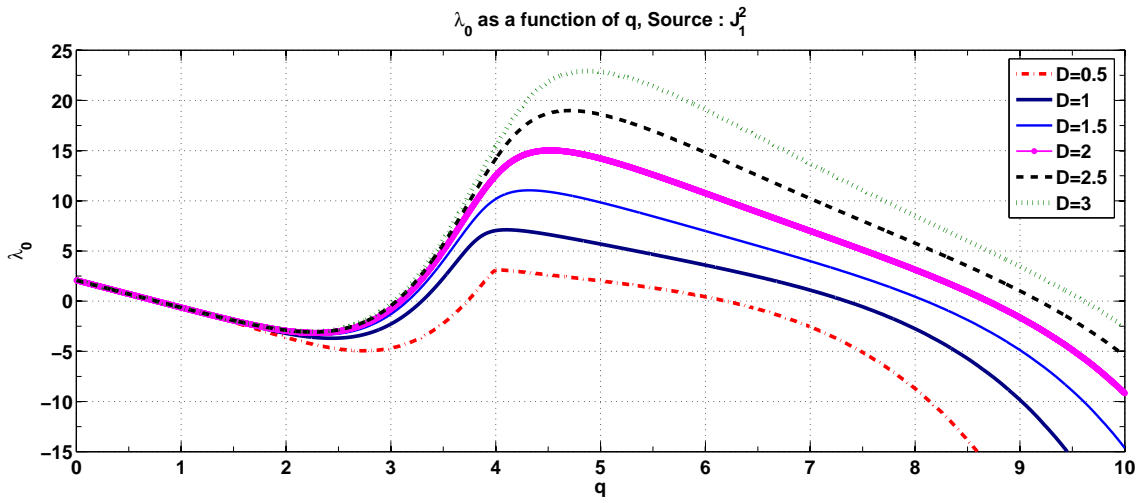


Figure 4.17 Lowest eigen-value λ_0 as a function of q , $S = J_1^2$.

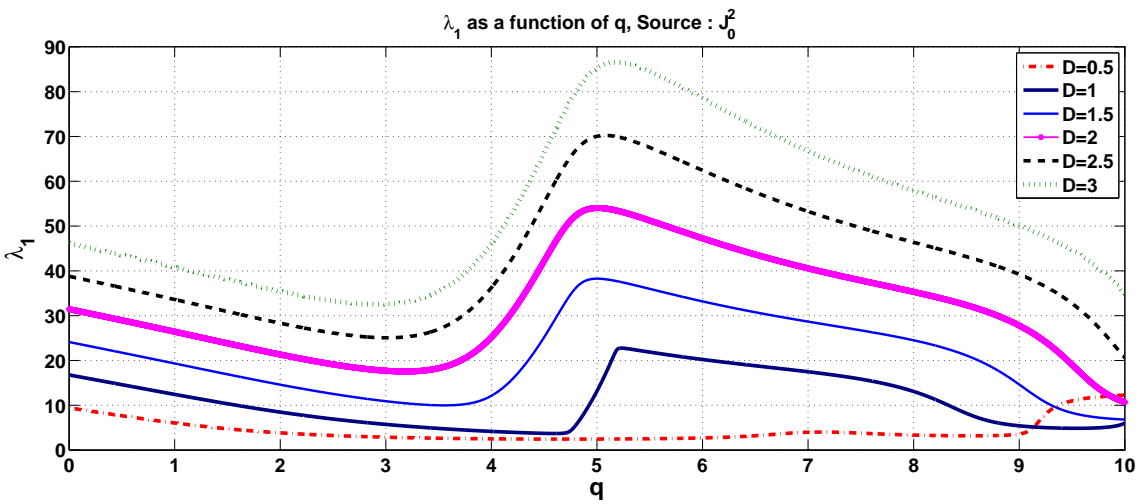


Figure 4.18 λ_1 as a function of q , $S = J_0^2$.

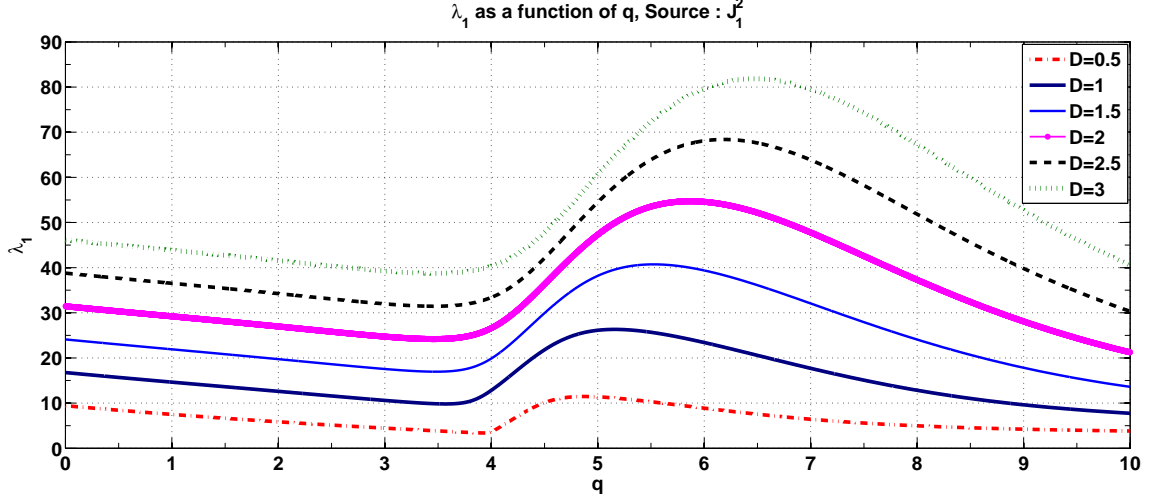


Figure 4.19 λ_1 as a function of q , $\mathbf{S} = J_1^2$.

again on the upper branch and what kind of instability triggers at this point. The L_2 norm of the solutions was found to start decreasing at this point. The behaviour of solutions near this point is under further investigation. Several other eigen-values were computed and they were all positive.

The non local eigen-values reveal some information about the linear stability of $u_0(r)$ for points (P, q) on the response curves in Figures 4.3 and 4.4. Stability of these solutions will be fully determined when the local eigen-values are also in hand. Now consider the case when $n \geq 1$. The right hand side of equation (4.15a) vanishes when $n \geq 1$. This gives rise to an infinite number of local eigen-value problems for A_n . All these problems are singular due to the presence of the $\frac{n^2}{r^2}$ term which is singular at the origin. In the limit when $P \rightarrow 0$, equation (4.15a) can be linearized to give

$$\frac{d^2 A_n}{dr^2} + \frac{1}{r} \frac{dA_n}{dr} + \frac{1}{D} \left\{ \Lambda - \frac{n^2}{r^2} - 2(1 + 4\delta) + O(P) \right\} A_n = 0, \quad (4.20a)$$

$$\frac{dA_n}{dr}(0) = \frac{dA_n}{dr}(1) = 0. \quad (4.20b)$$

The above eigen-value problem is in the form of Bessel's equation of order ν with parameter μ where $\nu = n/\sqrt{D}$ and $\mu = \frac{1}{D}(\Lambda - 2(1 + 4\delta) + O(P))$. The linearly independent solutions of equation (4.20a) are $J_\nu(\sqrt{\mu}r)$ and $N_\nu(\sqrt{\mu}r)$, where J_ν and

N_ν are Bessel functions of first and second kind. Since $N_\nu(\sqrt{\mu}r)$ is singular at the origin, eigen-functions look like $J_\nu(\sqrt{\mu_j}r)$, where μ_j are the eigen-values and $\sqrt{\mu_j}$ is the j^{th} zero w_j^ν of $\frac{dJ_\nu}{dr}$. So $\Lambda_{nj} = (w_j^\nu)^2 + 2(1 + 4\delta) - O(P)$ and $A_{nj}(r) = J_\nu(w_j^\nu r)$. Let $A_n = r^n \phi_n(r)$. This form of A_n brings all the singularity out in r_n . Inserting this form of A_n in equation (4.20a) gives:

$$\frac{d^2 \phi_n}{dr^2} + \left(\frac{2n+1}{r} \right) \frac{d\phi_n}{dr} + \frac{1}{D} \{ \Lambda - 2(1 + 4\delta) + O(P) \} \phi_n = 0, \quad (4.21a)$$

$$\frac{d\phi_n}{dr}(0) = \frac{d\phi_n}{dr}(1) = 0. \quad (4.21b)$$

Newton's method is now used to determine Λ_{nj} as a function of q . The eigen-values and eigen-functions are computed using the values of P and $u_0(r)$ found in Section 4.2. The first local eigen-value Λ_{11} as a function of q is shown in Figure 4.20 for $D = 1$. This eigen-value has simple zeros q_{11}^* . These zeros are decreasing functions of D .

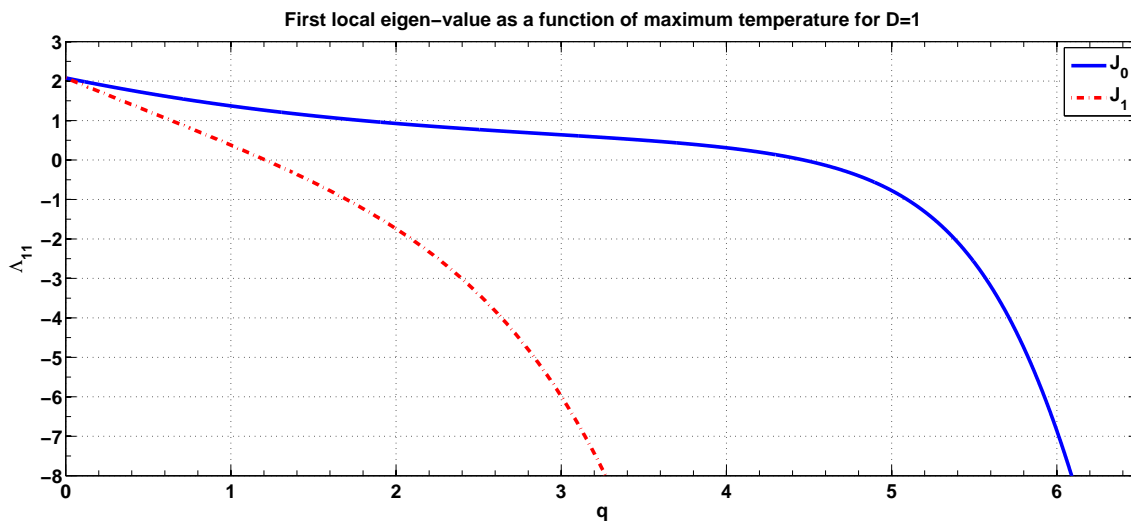


Figure 4.20 Λ_{11} as a function of q , $D = 1$.

4.4 Dynamical Simulations

Eigen-value λ_0 becoming negative suggests that the stationary solution $u_0(r)$ is unstable to certain choices of P and D . An explicit second order two-dimensional finite difference scheme was developed to approximate the solutions of equation (4.1a-c).

Different sets of initial data were chosen to study the time evolution of solutions and to understand the dynamics of the heating process. First, homogeneous initial data were chosen for different values of power. When $P < P_c$, initial data evolve to the stationary state corresponding to the lower branch. On the other hand, when $P > P_c$, initial data evolve to stationary state on the upper branch.

Next, the homogeneous initial data were replaced by the stationary solution $U_0(x, y)$ and the corresponding power on the S-shaped curve in Figures 4.3 and 4.4. In simulations with $P < P_L$, any initial data evolved to the stationary states on the lower branch. In simulations with $P > P_L$, any initial data that averaged to stationary solutions corresponding to the lower branch evolved to the stationary states on the lower branch. On the other hand, if the initial data that averaged to stationary solutions corresponding to the upper branch evolved to the stationary states on the upper branch.

It is well known that there are advantages of using explicit schemes over implicit schemes in that they are much simpler to use and also the computation time is much lower. However, the explicit scheme used above was not stable to perturbations in θ . To come around this problem, a locally one dimensional Crank Nicolson scheme in its polar form can be used [16] in which the original problem is written as a sequence of simpler problems so that each problem can be solved using a simple tri-diagonal solver. The splitting in time causes one order loss of accuracy in Δt but is worthwhile since the scheme is unconditionally stable so that larger time steps can be used and is more efficient than an implicit scheme. The results from this scheme have not been shown here and will be studied in detail in the future.

4.5 Conclusions

The heating of a thin silicon fibre in a highly resonant microwave cavity is studied mathematically by accurately approximating stationary solutions of the reaction diffusion equation (4.2a). The stability of stationary solutions depends on the lowest eigen-value λ_0 . This eigen-value becoming negative on the middle branch shows that the stationary solutions are unstable in r for certain choice of P and D . The local eigen-value Λ_{11} becoming negative shows that the stationary solutions become unstable to perturbations in θ for a certain value of power.

4.6 Future Work

1. Time evolution of steady state solutions to study the structure of modal patterns observed in experiments [21, 20].

2. When TM_{111} mode is excited, then the source term is given by $\cos^2(\theta)J_1^2(z_1^1 r)$. This gives rise to a physical problem where the source has strong angular dependence and the heat equation is two-dimensional. The corresponding time independent solution is a p.d.e. in r and θ and finite differences must be used to produce accurate approximate answers to the equation.

APPENDIX A

DELTA FUNCTION AS A SOURCE

Two mathematical models related to the physical models for $N = 1$ and $N = 2$ studied in Chapter 2 will be discussed in this chapter by purely analytical methods. The equations arising from these models have steady state solutions that have properties similar to the stationary solutions of the more realistic model.

A.1 A Model Problem: $N = 1$

The model that will be studied here is the initial, boundary value problem

$$\frac{\partial u}{\partial t} = D\nabla^2 u - 2u + \Gamma \delta(x - \frac{1}{2}) e^{Cu}, \quad t > 0, \quad (x, y) \in R, \quad (\text{A.1a})$$

$$\frac{\partial u}{\partial n} = 0, \quad (x, y) \in R, \quad u(x, y, 0) = 0, \quad (x, y) \in R, \quad (\text{A.1b})$$

$$\Gamma = \frac{p}{(1 + \chi \iint_R e^{cu} \delta(x - \frac{1}{2}) dx dy)^2}, \quad (\text{A.1c})$$

where $R = \{(x, y) | 0 < x < 1, 0 < y < 1\}$ and $\frac{\partial u}{\partial n}$ is the normal derivative. There are two differences between equation (A.1) and the real problem considered in Chapter 2. The first is the replacement of the modal power $\sin^2 \pi x$ by a delta function that fires at $x = 1/2$, the point of maximum power. The second is the linear loss term $-2u$ that neglects radiative losses from the slabs lateral surfaces.

Equation (A.1) admits a solution independent of t and y . Denoting this solution by $u_0(x)$ it satisfies the nonlinear functional boundary value problem

$$D \frac{d^2 u_0}{dx^2} - 2u_0 + \Gamma_0 \delta(x - \frac{1}{2}) e^{Cu_0} = 0, \quad 0 < x < 1, \quad (\text{A.2a})$$

$$\frac{du_0}{dx} = 0, \quad x = 0, 1, \quad (\text{A.2b})$$

$$\Gamma_0 = \frac{p}{(1 + \chi \int_0^1 e^{Cu_0} \delta(x - \frac{1}{2}) dx)^2}. \quad (\text{A.2c})$$

The function u_0 is continuous at $x = 1/2$, and its first derivative satisfies the jump condition $[D \frac{du_0}{dx}]_{x=1/2} = -\Gamma_0 e^{C u_0(1/2)}$ there. Since u_0 satisfies a linear differential equation for all $x \neq 1/2$, the solution can be constructed readily using the conditions at $x = 1/2$ and the boundary data at $x = 0, 1$. The result is

$$u_0 = A \begin{cases} \cosh \nu x, & 0 < x < \frac{1}{2} \\ \cosh \nu(1 - x), & \frac{1}{2} < x < 1, \end{cases}, \quad (\text{A.3a})$$

where $\nu = \sqrt{2/D}$, $A = u_0(0)$ satisfies

$$\Gamma_0 = \alpha A e^{-\beta A}, \quad (\text{A.3b})$$

$\alpha = 2\nu D \sinh(\frac{\nu}{2})$, and $\beta = C \cosh(\frac{\nu}{2})$. Finally, equation (A.2c) is evaluated using equation (A.3a) and equation (A.3b) is rearranged to obtain

$$p = \alpha A e^{-\beta A} (1 + \chi e^{\beta A})^2. \quad (\text{A.3c})$$

Two observations can be made about the solution. First, u_0 is symmetric about $x = 1/2$. This was shown numerically in Section 2.2.1 to be true for the more realistic source. Secondly, since the maximum of u_0 is $u_0^* = A \cosh \frac{\nu}{2}$, equation (A.3c) affords a relationship between p , the dimensionless power, and u_0^* the maximum norm of the dimensionless temperature. A typical result is shown in Figure A.1 with the parameter values $C = 1.5$, $\nu = 1.0$, $D = 1.25$ and $\chi = 0.01$, a typical value for a highly resonant cavity. For these typical values the response curve shown in Figure A.1 is S-shaped with turning points at A_1 and A_2 , where $\frac{dp}{dA} = 0$. These occur at the roots of the transcendental function

$$f(\theta) \equiv \theta \frac{1 - \chi e^\theta}{1 + \chi e^\theta} - 1, \quad \theta = \beta A, \quad (\text{A.3d})$$

which for small χ occur approximately at $A_1 = 1/\beta$ and $A_2 = \frac{1}{\beta} \ln(1/\chi)$.

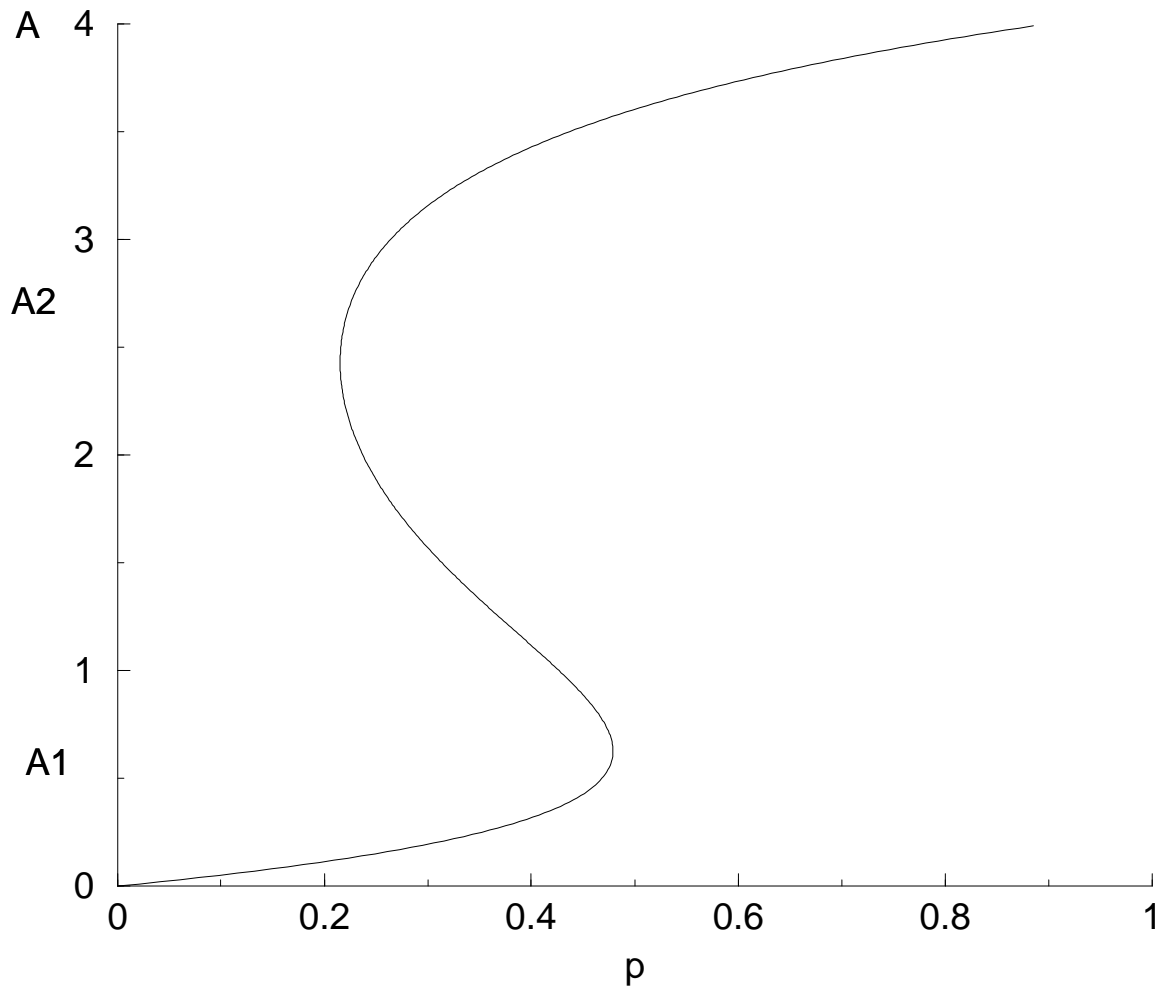


Figure A.1 u_0^* as a function of p .

The linear stability of the explicit solution i.e., equations (A.3a-c) will now be checked. Accordingly, look for a solution to equation (A.1a) of the form $u(x, y, t) = u_0(x) + v(x, y)e^{-\Lambda t}$, insert this into equation (A.1a), neglect any nonlinear terms in v , and obtain a linear eigenvalue problem for v and Λ . If any of the eigenvalues $\Lambda < 0$, then u_0 is linearly unstable. This problem is simplified by expanding $v(x, y)$ in the series

$$v(x, y) = \sum_{n=0}^{\infty} A_n(x) \cos n\pi y,$$

using equation (A.3b), and the fact that $f(x)\delta(x - 1/2) = f(1/2)$, for any continuous function. It is found that the amplitudes A_n satisfy

$$D \frac{d^2 A_0}{dx^2} + \left\{ \Lambda - 2 + G(A)\delta\left(x - \frac{1}{2}\right) \right\} A_0 = 0, \quad (\text{A.3a})$$

$$D \frac{d^2 A_n}{dx^2} + \left\{ \Lambda - 2 - l_n^2 + c\alpha A \delta\left(x - \frac{1}{2}\right) \right\} A_n = 0, \quad n \geq 1 \quad (\text{A.3b})$$

$$G(A) = \alpha c \left\{ \frac{1 - \chi e^{\beta A}}{1 + \chi e^{\beta A}} \right\} A, \quad (\text{A.3c})$$

$$l_n^2 = n^2 \pi^2 D^2, \quad (\text{A.3d})$$

along with the Neumann conditions $A_{nx} = 0$ at $x = 0, 1$. The difference between the coefficient $G(A)$ of the delta function in equation (A.3a) and $C\alpha A$ in equation (A.3b) is caused by the integral operator in equation (A.2c). The linearization of this operator only affects the zeroth order amplitude A_0 .

The spectrum of equation (A.3a) will now be described. Setting $\Lambda = 2 + D\lambda^2$ and exploiting the linearity of the problem and boundary conditions yields

$$A_0 = \begin{cases} \cos \lambda x, & 0 < x < \frac{1}{2} \\ \cos \lambda(1 - x), & \frac{1}{2} < x < 1, \end{cases} \quad (\text{A.5a})$$

where $A_0(0) = 1$ is the normalization. The function A_0 is continuous at $x = 1/2$ and has the jump $[DA_{0x}]_{x=1/2} = -\frac{G(A)}{D} A_0(1/2)$ there. Taking these facts into account and

equation (A.3c) one arrives at the transcendental equation

$$\frac{\lambda}{2} \tan \frac{\lambda}{2} = -\frac{C\nu}{2} \sinh \frac{\nu}{2} \left\{ \frac{1 - \chi e^{\beta A}}{1 + \chi e^{\beta A}} \right\} A. \quad (\text{A.5b})$$

A cursory graphical study of this equation shows that for all $A > 0$ there are an infinite number of eigenvalues $\{\lambda_n\}$, where $\lambda_n \rightarrow \pm\infty$ as $n \rightarrow \pm\infty$. These give $\Lambda_n = 2 + D\lambda_n^2 > 0$, the stable portion of the spectrum.

The remaining portion of the spectrum is found by setting $\Lambda = 2 - D\lambda^2$ in equation (A.3a), again exploiting the linearity of the problem and boundary conditions. One finds that A_0 is now given by

$$A_0 = \begin{cases} \cosh \lambda x, & 0 < x < \frac{1}{2} \\ \cosh \lambda(1 - x), & \frac{1}{2} < x < 1, \end{cases} \quad (\text{A.6a})$$

where $A_0(0) = 1$ is again the normalization. Taking these facts into account and equation (A.3c) one now arrives at the transcendental equation

$$\frac{\lambda}{2} \tanh \frac{\lambda}{2} = \frac{\nu}{2} \tanh \frac{\nu}{2} f(\theta), \quad (\text{A.6b})$$

where again $\theta = \beta A$ and $f(\theta)$ is defined in equation (A.3d). It is easy to show that $f(\beta A)$ initially increases with A reaching a maximum of $f_M = f(\beta A_M)$, where $A_1 < A_M, A_2$. Thus the root λ increases with A until A_M and decreases thereafter until $A = A_F = \frac{1}{\beta} \ln \frac{1}{\chi}$. For $A > A_F$, the function f is negative and equation (A.6b) no longer has a root. In the disjoint intervals $0 < A < A_1$ and $A_2 < A < A_F$ the function f satisfies $0 < f < 1$ and from equation (A.6b) we deduce that $0 < \lambda < \nu$. It follows from the definition of Λ and ν that $\Lambda > 0$ in this range, which corresponds to the upper and middle branches of the S-shaped response curve. When $A_1 < A < A_2$, $f > 1$ and one again deduces from equation (A.6b) that now $\lambda > \nu$ and hence, $\Lambda < 0$. This states that the middle branch is unstable. Finally, $f = 1$ at $A = A_1$ and $A = A_2$.

This implies that $\lambda = \nu$ at these points, where it follows that $\Lambda = 0$. These points correspond to the stationary points of $p(A)$.

Next consider the eigenvalue problem (A.3b) for A_n , $n \geq 1$ and first set $\Lambda = 2 + l_n^2 + D\lambda^2$. Following the same path as above one finds that A_n is given again by equation (A.5a). But now the jump condition consistent with equation (A.3b) gives the transcendental equation

$$\frac{\lambda}{2} \tan\left(\frac{\lambda}{2}\right) = -\frac{cA\nu}{2} \sinh\left(\frac{\nu}{2}\right). \quad (\text{A.7a})$$

Another cursory graphical study, of equation (A.7a), shows that for all $A > 0$ there are an infinite number of eigenvalues $\{\lambda_j\}$, where $\lambda_j \rightarrow \pm\infty$ as $n \rightarrow \pm\infty$. These give $\Lambda_j = 2 + l_n^2 + D\lambda_j^2 > 0$, the stable portion of the spectrum for each nodal number n .

Finally, set $\Lambda = 2 + l_n^2 - D\lambda^2$ and look for the remainder of the spectrum for each n . Again the eigenfunction satisfies equation (A.6a) but the jump condition consistent with equation (A.3b) yields

$$\frac{\lambda}{2} \tanh\left(\frac{\lambda}{2}\right) = \frac{cA\nu}{2} \sinh\left(\frac{\nu}{2}\right). \quad (\text{A.7b})$$

It is easy to graphically see that this equation has only two roots $\pm\lambda_*(A)$ with $\lambda_*(-\lambda^*)$ being an increasing (decreasing) function of A . The single corresponding Λ is given by

$$\Lambda = 2 + l_n^2 - D\lambda_*^2. \quad (\text{A.8})$$

From this result it is found that for a fixed n , $\Lambda < 0$ for A sufficiently large. That is every mode in the y direction becomes unstable for sufficiently large values of p . This was seen purely by numerical studies of the full problem.

A.2 The Model: $N = 2$

Now the same initial, boundary problem considered in Section 2 will be studied with modifications that equation (A.1a) is replaced by

$$u_t = D\nabla^2 u - 2u + \Gamma \left\{ \delta\left(x - \frac{1}{4}\right) + \delta\left(x - \frac{3}{4}\right) \right\} e^{Cu}, \quad t > 0, \quad (\text{A.9a})$$

and the functional in equation (A.1c) by

$$\Gamma = \frac{p}{(1 + \chi \iint_R e^{Cu} \{ \delta(x - \frac{1}{4}) + \delta(x - \frac{3}{4}) \} dx dy)^2}. \quad (\text{A.9b})$$

The domain R , boundary and initial conditions remain the same. The two delta functions model the more realistic source term $\sin^2 2\pi x$, which has maxima at the singular points.

Again, denote by u_0 the solution of the problem that is independent of y and t .

It now satisfies the nonlinear functional boundary value problem

$$Du_{0xx} - 2u_0 + \Gamma_0 \left\{ \delta\left(x - \frac{1}{4}\right) + \delta\left(x - \frac{3}{4}\right) \right\} e^{Cu_0} = 0, \quad 0 < x < 1, \quad (\text{A.10a})$$

$$u_{0x} = 0, \quad x = 0, 1 \quad (\text{A.10b})$$

$$\Gamma_0 = \frac{p}{(1 + \chi \int_0^1 e^{Cu_0} \{ \delta(x - \frac{1}{4}) + \delta(x - \frac{3}{4}) \} dx)^2}. \quad (\text{A.10c})$$

The function u_0 is continuous at $x_1 = 1/4$ and $x_2 = 3/4$ with corresponding jumps $[Du_{0x}]_{x=x_j} = -\Gamma_0 e^{Cu_0(x_j)}$ at these points.

Since equations (A.10a-c) are linear, one readily obtains the solution

$$u_0 = \begin{cases} A \cosh \nu x, & 0 < x < \frac{1}{4} \\ B \cosh \nu(x - \frac{1}{4}) + C \sinh \nu(x - \frac{1}{4}), & \frac{1}{4} < x < \frac{3}{4}, \\ E \cosh \nu(1 - x), & \frac{3}{4} < x < 1. \end{cases} \quad (\text{A.11a})$$

Applying the continuity and jump conditions at x_1, x_2 , and eliminating the coefficients B and C , one finds that A and E satisfy two coupled nonlinear transcendental equations. Setting

$$u = \frac{c}{2} \cosh \frac{\nu}{4} (A - E) \quad (\text{A.11b})$$

and

$$v = \frac{c}{2} \cosh \frac{\nu}{4} (A + E) \quad (\text{A.11c})$$

one finds after some simplifications that u and v satisfy

$$c_1 v = \gamma_0 e^v \cosh u \quad (\text{A.11d})$$

$$c_2 u = \gamma_0 e^v \sinh u, \quad (\text{A.11e})$$

where $c_1 = 2 \sinh \frac{\nu}{2} \sinh \frac{\nu}{4}$, $c_2 = 2 \cosh \frac{\nu}{2} \cosh \frac{\nu}{4}$, and $\gamma_0 = \frac{c\Gamma_0}{\nu D} \sinh \frac{\nu}{2} \cosh \frac{\nu}{4}$.

One solution of these equations gives $u = 0$ and v implicitly by $\gamma_0 = c_1 v e^{-v}$. Using the definition of γ_0 in terms of Γ_0 , evaluating equation (A.10c), applying equations (A.11b-11c), and noting $u = 0$, one obtains

$$p = p_0 v e^{-v} \{1 + 2\chi e^v\}^2, \quad p_0 = \frac{2\nu D}{c} \tanh \frac{\nu}{4}. \quad (\text{A.12})$$

Since $u = 0$, it follows from equation (A.11b) that $A = E$ and from equation (A.11c) that $v = c \cosh \frac{\nu}{4} A$. Inserting this last result into equation (A.12), it is seen that $p(A)$ is of the same exact form as equation (A.3c). Thus again, the response curve is S-shaped. Moreover, it follows from equation (A.11a) with $E = A$ and the continuity at x_1 and x_2 that $u_0(x)$ is symmetric about $x = 1/2$ with a maximum of $u_0(1/2) = A$.

Equations (A.11d-11e) admit another type of solution, where $u \neq 0$. Then, we can divide (A.11d) by (A.11e) and find that v satisfies

$$v = c_3 u \coth u, \quad c_3 = \coth \frac{\nu}{2} \coth \frac{\nu}{4}. \quad (\text{A.13a})$$

Inserting this result into equation (A.11e) and again evaluating equation (A.10c), now with $u \neq 0$, one arrives at

$$p = p_1 \frac{u}{\sinh u} e^{-c_3 u \coth u} \{1 + 2\chi \cosh u e^{c_3 u \coth u}\}^2, \quad p_1 = \frac{2\nu D}{c} \coth \frac{\nu}{2}. \quad (\text{A.13b})$$

Since $u \neq 0$, it follows from (A.11b) that $A \neq E$ and from (A.11a) that the solution $u_0(x)$ is no longer symmetric about the midpoint $x = 1/2$. This asymmetric solution bifurcates from the point $(p^*, u^*) \sim (p_1 e^{-c_3}, 0)$, which is obtained from (A.13b) by letting $u \rightarrow 0$ and recalling that $0 < \chi \ll 1$. The graph of equation (A.13b) is shown in Figure A.2 for $D = 1, \nu = \sqrt{2}$, and $\chi = 0.01$.

The corresponding bifurcation diagram for v is shown as the solid curve in Figure A.3 for the same sequence of parameters. When $p = p^*$, $u = 0$, and $v = c_3$ from equation (A.13a). This is why the graph starts at the point (p^*, c_3) . Also shown in Figure A.3, as a dashed curve, is the graph of the symmetric solution given by equation (A.12). Note that the asymmetric solution bifurcates from this curve at (p^*, c_3) . This same bifurcation phenomenon was observed in the physical model, where the source term is proportional to $\sin^2(2\pi x)$, by purely numerical means.

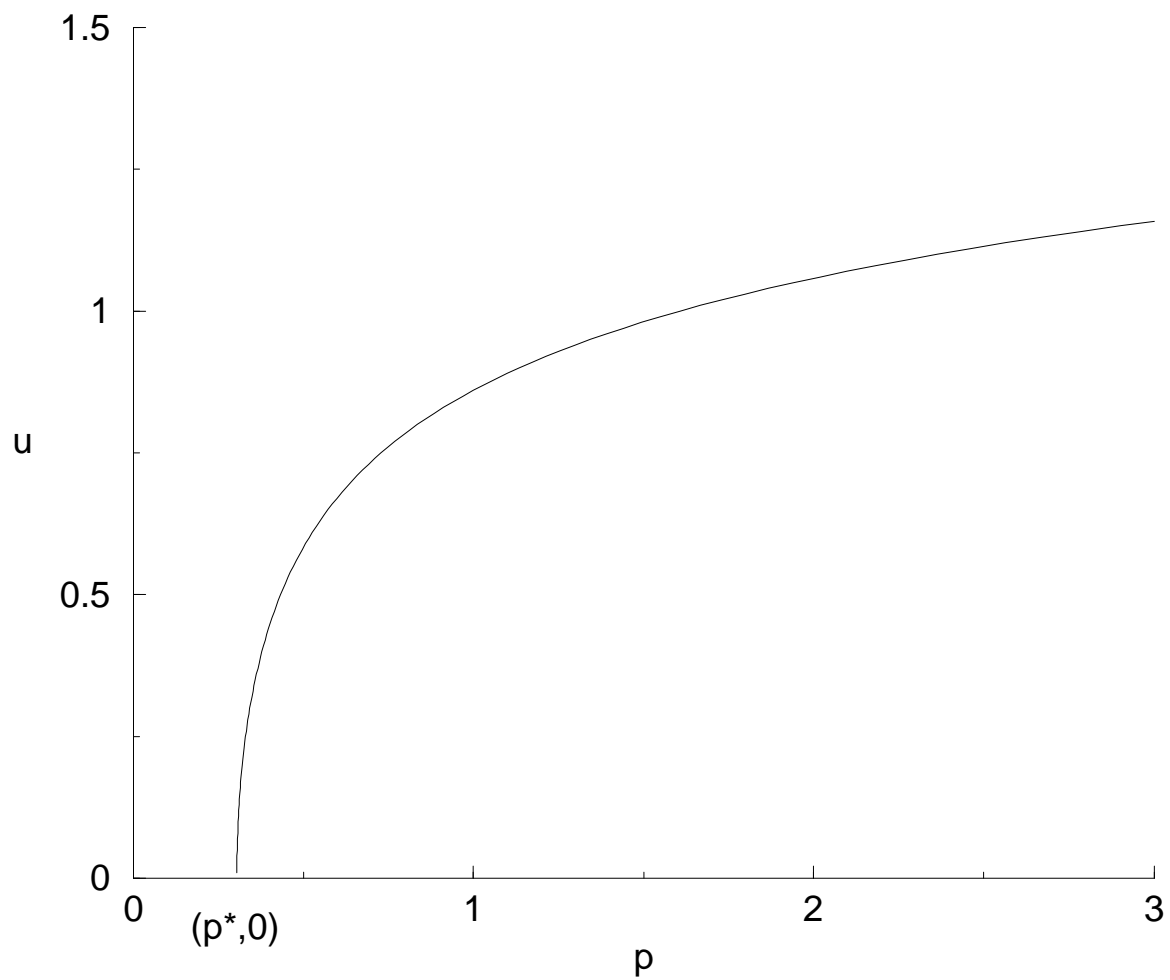


Figure A.2 Bifurcation branch for $D = 1$.

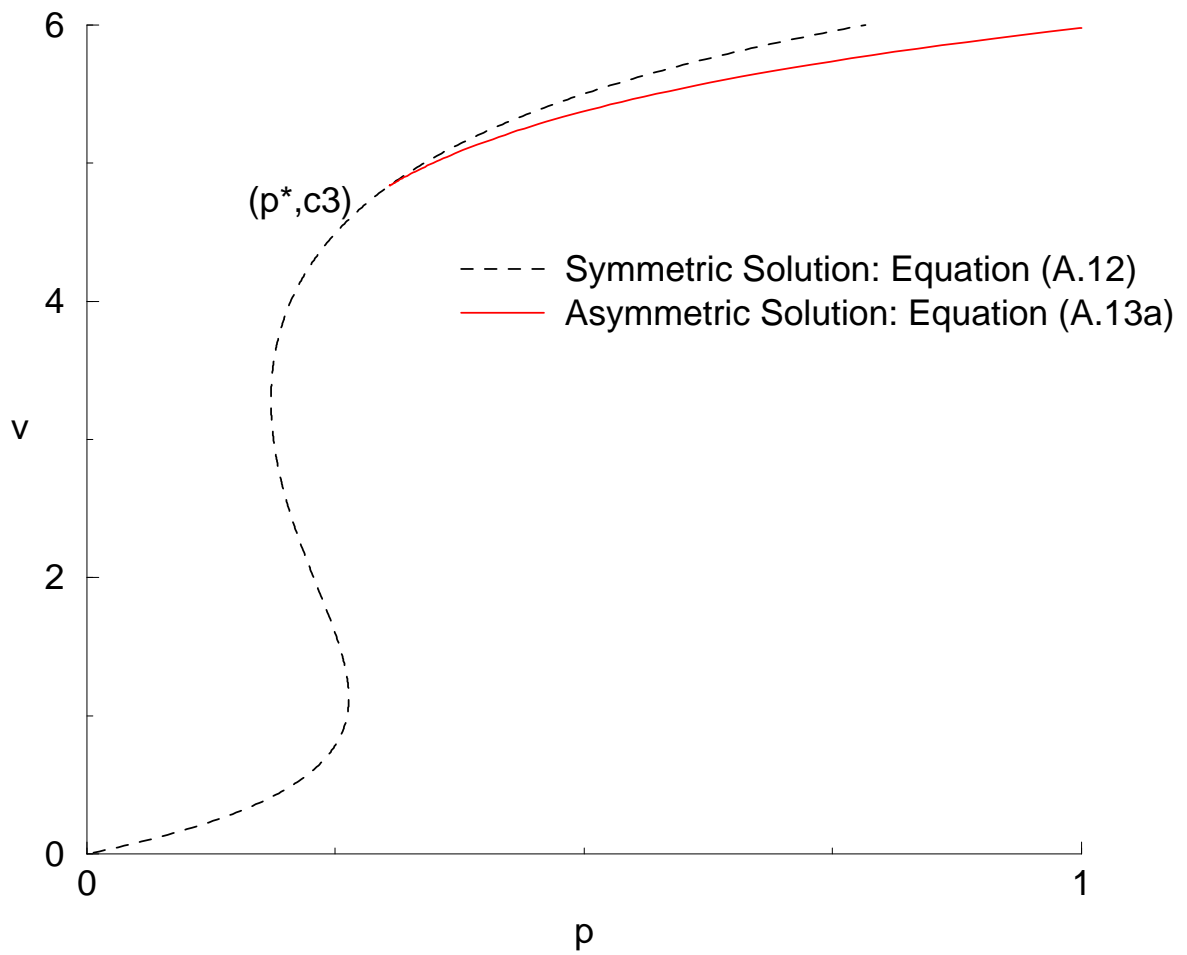


Figure A.3 Symmetric and asymmetric solutions for $D = 1$.

REFERENCES

- [1] Michael R. Booty and Gregory A. Kriegsmann. Microwave heating and joining of ceramic cylinders: A mathematical model. *Methods and Applications of Analysis*, 1(4):403–414, 1994.
- [2] Morris E. Brodwin and J.T. Chang. A new microwave oven for efficient uniform heating based upon a circular cylindrical geometry. In *Microwave Conference Brazil*, 1993.
- [3] Morris E. Brodwin and D. Lynn Johnson. Microwave sintering of ceramics. *IEEE MTT-S Digest*, 1:287–288, 1988.
- [4] Yu. V. Bykov, K. I. Rybakov, and V. E. Semenov. High-temperature microwave processing of materials. *J. Phys. D: Appl. Phys.*, 2001.
- [5] D. E. Clark. Microwaves: Theory and application in materials processing iv, ed clark,d., et al. (westerville, oh: The american ceramic society). *Ceramic Transactions*, 1997.
- [6] E. Jerby and V. Dikhtyar. Method and device for drilling, cutting, nailing and joining solid non-conductive materials using microwave radiation. *US Patent 6,114,676*, 2000.
- [7] E. Jerby, V. Dikhtyar, and O. Aktushev. Microwave drill for ceramics. *Ceramic Bulletin*, (82), 2003.
- [8] J. D. Katz. Microwave sintering of ceramics. *Annual Review of Materials Science*, 22:153–170, 1992.
- [9] W. D. Kingery et al. *Introduction to Ceramics*. Wiley, New York, New York, second edition, 1976.
- [10] G. A. Kriegsmann. Microwave heating of ceramics: a mathematical theory, in microwaves: Theory and applications in materials processing, edited by clark,d.e., gak,f.d., and sutton,w.h. *Ceramic Transactions, American Ceramic Society, Cincinnati, OH*, 1991.
- [11] G. A. Kriegsmann. Thermal runaway in microwave heated ceramics. *J. Appl. Phys.*, (71):1960–1966, 1992.
- [12] G. A. Kriegsmann. Cavity effects in microwave heating of ceramics. *SIAM Journal of Applied Mathematics*, 57(2):382–400, 1997.
- [13] G. A. Kriegsmann. Pattern formation in microwave heated ceramics: Cylinders and slabs. *IMA Journal of Applied Mathematics*, 66(1):1–32, 2001.

- [14] G.A. Kriegsmann. Microwave heating of silicon wafers in cylindrical tm cavities: a mathematical model. In D.C. Folz, J.H. Booske, D. E. Clark, and J. F. Gerling, editors, *Microwave and Radio Frequency Applications*, pages 127–142, Sydney, Australia, 2003. The Microwave Working Group, Wiley.
- [15] E. B. Kulumbaev, V. E. Semenov, and K. I. Rybakov. Stability of microwave heating of ceramic materials in a cylindrical cavity. *J. Phys. D: Appl. Phys.*, 40(21):6809–6817, 2007.
- [16] A.R. Mitchell and D.F. Griffiths. *The Finite Difference Method in Partial Differential Equations*. John Wiley and Sons, New York, New York, first edition, 1980.
- [17] L. Perko. *Differential Equations and Dynamical Systems*. Springer-Verlag, New York, New York, third edition, 2001.
- [18] W. H. Press et al. *Numerical Recipes in C*. Cambridge University Press, New York, New York, second edition, 1992.
- [19] W.H. Sutton. Microwave processing of ceramics - an overview. In M.A. Janney and et al., editors, *Microwave Processing of Materials III*, volume 269, pages 3–20, Washington, D.C., 1994. Materials Research Society, The National Academies Press.
- [20] K. Thompson, J.H. Booske, Y.B. Gianchandani, and R.F. Cooper. Direct si-si bonding by electromagnetic induction heating. *Journal of MicroElectroMechanical Systems*, 11(4):285–292, 2002.
- [21] K. Thompson, J.H. Booske, Y.B. Gianchandani, and R.F. Cooper. Electromagnetic annealing for the 100nm technology node. *IEEE Electron Device Letters*, 23(3):127–129, 2002.
- [22] W. R. Tinga and E. M. Edwards. Dielectric measurement using swept frequency techniques. *J. Microwave Power*, 3:144–175, 1968.
- [23] W. R. Tinga and A. G. Voss. *Microwave Power Engineering*. Academic Press, New York, New York, first edition, 1968.
- [24] A. R. Von Hippel. *Dielectric Materials and Applications*. Wiley, New York, New York, first edition, 1954.
- [25] Stuart J. Walker. *Multi-Mode Cavity Effects on the Microwave Heating of a Ceramic Slab*. PhD thesis, NJIT, Newark, New Jersey, 2001.
- [26] Michael J. Ward. Thermal runaway and microwave heating in thin cylindrical domains. *IMA Journal of Applied Mathematics*, 67(2):177–200, 2002.